LBNL-47208

ERNEST ORLANDO LAWRENCE BERKELEY NATIONAL LABORATORY

Deformation Behavior of Aluminum Alloy 6111-T4

Carol Tseng

Materials Sciences Division

December 2000

Ph.D. Thesis

REFERENCE COPY
Does Not
Circulate

Lawrence Berkeley National Laboratory

Copy 1

Annex

LBNL-47208

DISCLAIMER

This document was prepared as an account of work sponsored by the United States Government. While this document is believed to contain correct information, neither the United States Government nor any agency thereof, nor the Regents of the University of California, nor any of their employees, makes any warranty, express or implied, or assumes any legal responsibility for the accuracy, completeness, or usefulness of any information, apparatus, product, or process disclosed, or represents that its use would not infringe privately owned rights. Reference herein to any specific commercial product, process, or service by its trade name, trademark, manufacturer, or otherwise, does not necessarily constitute or imply its endorsement, recommendation, or favoring by the United States Government or any agency thereof, or the Regents of the University of California. The views and opinions of authors expressed herein do not necessarily state or reflect those of the United States Government or any agency thereof or the Regents of the University of California.

LBNL-47208

Deformation Behavior of Aluminum Alloy 6111-T4

Carol Tseng
Ph.D. Thesis

Materials Science and Engineering Department
University of California, Berkeley

and

Materials Sciences Division
Ernest Orlando Lawrence Berkeley National Laboratory
University of California
Berkeley, CA 94720

December 2000

This work was supported by the Director, Office of Science, Office of Basic Energy Sciences, Materials Sciences Division, of the U.S. Department of Energy under Contract No. DE-AC03-76SF00098.

Deformation Behavior of Aluminum Alloy 6111-T4

by

Carol Tseng

B.S. (University of California, Berkeley) 1989
M.S. (University of California, Berkeley) 1993

A dissertation submitted in partial satisfaction of the

requirements for the degree of

Doctor of Philosophy

in

Engineering- Materials Science and Engineering

in the

GRADUATE DIVISION

of the

UNIVERSITY OF CALIFORNIA, BERKELEY

Committee in charge:

Professor John W. Morris, Jr., Chair
Professor Robert O. Ritchie
Professor Lisa Pruitt

Fall 2000

Abstract

Deformation Behavior of Aluminum Alloy 6111-T4

by

Carol Tseng

Doctor of Philosophy in Materials Science and Engineering

University of California, Berkeley

Professor J. W. Morris, Jr., Chair

Although aluminum alloys have found increasing usage in the automotive industry, their lower tensile elongations as compared with the low carbon steels they replace has raised concern about their lower formability. Lower formability imposes design and economic constraints on the automakers. The cause behind this lower elongation is the primary focus of this research. The specific alloy studied is 6111-T4 (Al-0.76Si-0.61Mg-0.82Cu in w/o), which is used in automobile outer body panels. In order to determine the factors that are limiting the elongation, it is critical to understand the deformation behavior of this alloy. To investigate the deformation behavior of this alloy, uniaxial tensile tests were performed at various temperatures (300K, 77K and 4.2K), strain rates (10^{-4}, 5×10^{-4}, 10^{-3}, 10^{-2}, 10^{-1} /s) and specimen geometries. The work hardening and deformation behavior were examined both qualitatively and quantitatively. Ex-situ and in-situ observations were made on the tensile samples by using videography

and optical microscopy. Several important findings resulted from this study. First, oscillations in the work hardening are due to the formation and propagation of deformation islands and deformation bands. Deformation islands are areas of localized deformation that occur in a cluster of grains. Second, the microstructural feature dominating the formation and propagation of the islands are the clustering of similarly oriented grains and the clustering of large sized grains. Third, the sharp drop in work hardening near the diffuse necking criterion for the 300K, 10^{-4} /s test samples is due to the inhomogeneous deformation arising from these clusters. Finally, diffuse and local necks form before the theoretical predictions. The inhomogeneous microstructures causing the deformation islands and bands to form and propagate, thus leading to strain localization and eventual premature failure.

ACKNOWLEDGMENTS

The completion of this thesis would not have been possible without the help and support of many people. I would like to thank my advisor, Professor Bill Morris, for his support and guidance through the years, and my committee, Professors Robert Ritchie and Lisa Pruitt, for taking the time to read this thesis and offer their expertise. The EBSP microscopy would not have been possible without the time and help from Professor Rudy Wenk and his group. I especially appreciate the technical expertise that Dr. Jin Chan offered in conducting many of the experiments as well as in interpreting the data. Dr. Chan and Dr. Pamela Kramer have offered invaluable comments on the thesis draft. The Morris Group members, both past and present, have been a wonderfully supportive group, and it has been a pleasure to work with them.

My family and friends have also been instrumental in this effort. I'd like to thank my husband and children for their support through the years. Without them, I would not have had such a rich experience in graduate school and in my life. A big thank you to my parents, who have been so supportive in everything I have undertaken in my life and have set a good example for me. I want to extend a special thank you to the Youngs: Mr. and Mrs. Young, Jerry, Andrea, and Calvin; they have selflessly contributed countless hours of their lives to help me through.

TABLE OF CONTENTS

1 Introduction 1

1.1 Background 1

1.2 Physical Metallurgy of 6111-T4 4

1.3 Objective 5

2 Experimental Procedure 6

3 Material Characterization Results 10

3.1 Optical Microscopy and SEM 10

3.2 EBSP 10

3.3 Fractography 14

3.4 Summary 15

4 Mechanical Properties Results 16

4.1 300K Tensile Tests 16

4.1.1 6111-T4 Longitudinal 16

4.1.2 6111-T4 Transverse 16

4.1.3 6111-T4 Wide and Narrow Samples 17

4.1.4 6111 Transverse Solution Heat Treated 18

4.1.5 AKDQ Steel 18

4.1.6 6061-T6 Sheet 19

4.1.7 6061-T6 Round Cross-Section 19

4.2 77K Tensile Tests 20

4.2.1 6111-T4 Longitudinal 20

4.2.2 6111-T4 Transverse 20

4.3 4.2K Tensile Test 21

4.3.1 6111-T4 Longitudinal 21

4.4 Summary 21

5 Work Hardening and Deformation Behavior Results 23

5.1 6111-T4 Longitudinal 23

5.2 6111-T4 Transverse 24

5.3 6111-T4 Wide 24

5.4 6111-T4 Narrow 25

5.5 6111 SHT 25

5.6 6061-T6 25

5.6.1 Sheet 25

5.6.2 Round Cross-Section 26

5.7 AKDQ Steel 26

5.8 Summary 26

5.9 Surface Observations 26

5.10 Necking Measurements 28

5.11 Fractography 29

5.12 Summary 30

6 Discussion 31

6.1 Strength Effect on the Elongation 32

6.2 Stable vs. Stable Deformation at 300K, 10^{-4} /s 33

6.2.1 The Role of Voids in Early Failure 33

6.3 Deformation Behavior: 6111-T4, Longitudinal 38

6.3.1 Work Hardening Oscillations 38

6.3.1.1 Mechanism for Oscillations 39

6.3.1.1.1 The PLC Effect and Inhomogeneous Deformation 40

6.3.1.1.2 Effect of Microstructure and Islands on Oscillation Behavior 41

6.3.1.2 Effect of Oscillations on Elongation 43

6.3.2 Necking Behavior 44

6.3.3 Assessment of the Deformation Behavior 45

6.3.3.1 Effect of Test Variables 46

6.3.3.2 Effect of Solute/Precipitate Structure 48

6.3.3.3 Effect of Specimen Geometry 49

6.3.4 Necking Measurements 51

6.4 Island Formation and Propagation: Dominant Microstructural Feature 52

6.5 Model for Island Formation and Propagation 56

7 Summary and Conclusions 58

8 Outstanding Issues and Suggested Future Work 61

References 62

Appendix A 65

LIST OF FIGURES

Figure 1 Uniaxial tensile elongations for 6111-T4 and AKDQ steel.

Figure 2 a) Schematic plot of the work hardening rate, θ, and one-half true stress, $\frac{\sigma}{2}$, versus true strain, ε. The upper curve is the work hardening rate, and the lower curve (shaded) is the $\frac{\sigma}{2}$ vs. ε. Where the two curves meet is where the local necking criterion theoretically occurs.

b) A higher work hardening rate at higher strains (shaded curve) will delay the onset of necking and increase the elongation of the material.

Figure 3 Local deformation occurs on the macroscopic scale. The size can range from deformation occurring in a few grains (left), or deformation islands, to spanning the width of the sample (right), or deformation bands.

Figure 4 a) Deformation islands and bands can form and propagate through a cluster of similarly oriented grains. The shaded grains have an orientation that is different from the surrounding grains.

b) The shaded grains form a cluster of large sized grains. These large sized grains act as a "soft" area through which islands can form and propagate. The arrow indicates the direction in which the deformation will propagate.

Figure 5 Stress-strain curve of 6061 [Robinson , 1994]. Serrations due to the PLC effect can be seen in the curve and are magnified in the inset. Longer wavelength oscillations, of varying amplitude, are also seen in the figure.

Figure 6 Drawings of the specimen dimensions for various tensile samples: a) standard, b) 6111-T4 wide, c) narrow [Chan] and d) round cross-section [Chan]. Note: drawings are not as scale.

Figure 7 a) Optical micrograph of the grain structure in 6111-T4. There is clustering of grains with similar shades of gray. b) Same micrograph as that in a), clusters of large sized grains (> 50 μm) are colored in black.

Figure 8 Histogram of the grain size distribution in 6111-T4.

Figure 9 Plot of an orientation in Euler space.

Figure 10 Schematic of grains with a particular orientation (dots) at a particular x-y location in a gage section of a tensile sample. This kind of plot is useful for determining which clusters of a particular orientation are located.

Figure 11 Euler angle plot of orientations found in a 6111-T4 sample. There is evidence of clustering of orientations.

Figure 12 Plots of grains with a particular orientation at their respective x-y coordinates in the gage section: a) Cube {100}<001>, b) Goss {110}<001>, c) R {124}<211>, d) P {011}<122>, e) Q{013}<231>, f) Copper {112}<111>, g) Brass {011}<211> and h) S{123}<634>. Rolling direction (RD), also the tensile direction, is in the x-direction, and the transverse direction (TD) is in the y-direction. The S texture has clusters of grains, and many of these clusters are at an angle to the rolling and tensile directions.

Figure 13 SEM micrographs of the fracture surfaces of 6111-T4, in the longitudinal direction, at various test conditions. a) 10^{-4} /s, 300K, b) 10^{-1} /s, 300K, c) 10^{-4} /s, 77K, d) 10^{-1} /s, 77K and e) 4K, 10^{-1} /s. The fracture micromode remains ductile.

Figure 14 SEM micrographs of the fracture surfaces of 6111-T4, in the transverse direction, at various test conditions. a) 10^{-4} /s, 300K, b) 10^{-1} /s, 300K, c) 10^{-4} /s, 77K and d) 10^{-1} /s, 77K. The fracture micromode is ductile for the test conditions.

Figure 15 Engineering stress-strain curve of 6111-T4 at 300K and at strain rates of 10^{-4}, 5×10^{-4}, 10^{-3}, 10^{-2}, and 10^{-1} /s. Despite the three orders of magnitude increase in strain rate, the stress-strain behavior does not significantly change.

Figure 16 Engineering stress-strain curve of 6111-T4 transverse samples at 300K and at strain rates of 10^{-4}, 5×10^{-4}, 10^{-3}, 10^{-2}, and 10^{-1} /s. Despite the three orders of magnitude increase in strain rate, the stress-strain behavior does not significantly change.

Figure 17 Engineering stress-strain curve of 6111-T4 at 300K and at strain rates of 10^{-4} and 10^{-1} /s with a change in geometry. Only minor changes in stress-strain behavior occur when the gage width increases.

Figure 18 Engineering stress-strain curve of 6111 SHT at 300K and at strain rates of 10^{-4} and 10^{-1} /s. The stress-strain behavior changes with increasing strain rate.

Figure 19 Engineering stress-strain curve of AKDQ steel at 300K and at strain rates of 10^{-4}/s (solid circles) and 10^{-1} /s (x). A change in strain rate does change the stress-strain behavior.

Figure 20 Engineering stress-strain curve of 6061-T6 at 300K and at strain rates of 10^{-4} and 10^{-1} /s for sheet and round cross-section samples. Minor changes occur in the stress-strain behavior with increasing strain rate. The stress-strain behavior changes dramatically with change in specimen geometry.

Figure 21 Engineering stress-strain curve of 6111-T4 at 77K and at strain rates of 10^{-4} and 10^{-1} /s for longitudinal and transverse samples. As compared with the 300K curves (figures 15 (longitudinal) and 16 (transverse)), the 77K behavior changes more dramatically with an increase in strain rate.

Figure 22 a) Schematic of a work hardening plot with oscillations. b) Schematic work hardening plot displaying a gradual work hardening drop off (shaded curve) versus a sharp drop off (solid) near the diffuse necking criterion.

Figure 23 Plots of θ and $\frac{\sigma}{2}$ vs. ε for 6111-T4 longitudinal specimens tested at 300K: a) 10^{-4} /s, b) 5×10^{-4} /s, c) 10^{-3} /s, d) 10^{-2} /s, e) 10^{-1} /s and f) stable versus unstable at 10^{-4} /s.

Figure 24 Plots of θ and $\frac{\sigma}{2}$ vs. ε for 6111-T4 longitudinal specimens tested at 77K: a) 10^{-4} /s and b) 10^{-1} /s.

Figure 25 Plots of θ and $\frac{\sigma}{2}$ vs. ε for 6111-T4 longitudinal specimens tested at 300K and 77K: a) 10^{-4} /s and b) 10^{-1} /s.

Figure 26 Plots of θ and $\frac{\sigma}{2}$ vs. ε for 6111-T4 transverse specimens tested at 300K: a) 10^{-4} /s and b) 5 x 10^{-4} /s, c) 10^{-3} /s, d) 10^{-2} /s and e) 10^{-1} /s.

Figure 27 Plots of θ and $\frac{\sigma}{2}$ vs. ε for 6111-T4 transverse specimens tested at 77K: a) 10^{-4} /s and b) 10^{-1} /s.

Figure 28 Plots of θ and $\frac{\sigma}{2}$ vs. ε for 6111-T4 transverse specimens tested at 300K and 77K: a) 10^{-4} /s and b) 5 x 10^{-4} /s, c) 10^{-3} /s, d) 10^{-2} /s and e) 10^{-1} /s.

Figure 29 Plots of θ and $\frac{\sigma}{2}$ vs. ε for 6111-T4 wide specimens tested at 300K: a) 10^{-4} /s and b) 10^{-1} /s.

Figure 30 Plots of θ and $\frac{\sigma}{2}$ vs. ε for 6111-T4 narrow specimen tested at 300K and at 10^{-4} /s.

Figure 31 Plots of θ and $\frac{\sigma}{2}$ vs. ε for 6111 SHT and -T4 transverse specimens tested at 300K: a) 10^{-4} /s and b) 10^{-1} /s.

Figure 32 Plots of θ and $\frac{\sigma}{2}$ vs. ε for 6061-T6 specimens tested at 300K and strain rates of 10^{-4} and 10^{-1} /s: a) sheet and b) round cross-section specimens.

Figure 33 Plots of θ and $\frac{\sigma}{2}$ vs. ε for AKDQ steel tested at 300K and at strain rates of a) 10^{-4} /s and b) 10^{-1} /s.

Figure 34 Optical micrograph of areas of local deformation (arrows) that have formed on a sample that was polished and strained to 1% plastic strain. a) Higher magnification and b) lower magnification (photo is inverted from a)). The

local deformation areas are approximately 40 μm wide and range from 400-800 μm long.

Figure 35 Optical micrograph of 6111-T4 (4.2K, 10^{-4} /s) specimen surface. Fracture surface is at the top of the micrograph. Intense slip occurs in some grains but not in other.

Figure 36 Optical micrograph of 6111-T4 (4.2K, 10^{-4} /s) specimen surface. Several deformation bands are visible. Each division on the scale is 1 mm.

Figure 37 Plots of θ and $\frac{\sigma}{2}$ vs. ε for 6111-T4 (300K, 10^{-4}/s) specimens used for measuring width and thickness changes: a) BDN1, b) BDN2, c) BDN3, d) DN1, e) DN2 and f) LN.

Figure 38 Engineering strain vs. position in the gage section for BDN1, BDN2 and BDN3 in the a) width and b) thickness directions.

Figure 39 Engineering strain vs. position in the gage section for DN1, DN2 and LN in the a) width and b) thickness directions.

Figure 40 Percent change in mechanical properties for 6111-T4 longitudinal samples when increasing the strain rate from 10^{-4} /s to 10^{-1} /s at a) 300K and b) 77K.

Figure 41 Percent change in mechanical properties for 6111-t4 longitudinal samples when decreasing the test temperature from 300K to 77K at a constant strain rate of a) 10^{-4} /s and b) 10^{-1} /s.

Figure 42 Percent change in mechanical properties for 6111-T4 transverse samples when increasing the strain rate from 10^{-4} /s to 10^{-1} /s at a) 300K and b) 77K.

Figure 43 Percent change in mechanical properties for 6111-T4 transverse samples when the test temperature decreases from 300k to 77K at a) 10^{-4} /s and b) 10^{-1} /s.

Figure 44 Schematic of how low strain rate sensitivity can cause deformation to localize in the next weakest area. The next weakest area is due to void growth.

Figure 45 SEM micrographs of the fracture surfaces for 6111-T4 samples (300K and 10^{-4} /s0 which displayed a) unstable and b) stable deformation behavior.

Figure 46 Schematic of the strain gradient in the LT plane of the fractured tensile specimen. The gradient increases from left to right, as the fracture surface is approached. The void population increases from left to right, as the strain gradient increases.

Figure 47 Optical micrographs of the region near the fracture surface (top of micrographs) for the a) stable deformation sample and b) unstable deformation sample at 300K and 10^{-4} /s. No obvious differences are seen in their void distributions.

Figure 48 Optical micrographs of typical fracture surfaces for both stable and unstable samples (300K and 10^{-4} /s). The fracture surface has regions that have a) a jagged appearance and b) a flat fracture surface.

Figure 49 Micrographs of the etched fracture surface (300K, 10^{-4} /s). Fracture occurs along grain boundaries as well as through grains. Fracture through grains of similar contrast can be seen at the arrow.

Figure 50 Optical micrographs of the grip section of a prepolished tensile sample. No fractured particles are visible; therefore, the polishing procedure does not introduce fractured particles.

Figure 51 Schematic of a work hardening curve (θ, $\frac{\sigma}{2}$ vs. ε). A line can be fitted to the latter region (Region A).

Figure 52 a) True stress-strain curve and b) work hardening curve of data generated by using the parabolic relationship $\sigma = K\varepsilon^{0.2}$. No oscillations are introduced during the data processing.

Figure 53 Schematic of how long wavelength oscillations (heavy line) often seen in stress-strain curves from the literature. These oscillations are observed in the stress-strain curve such as in figure 5 but have not been addressed. In materials that exhibit serrated flow, these oscillations occur simultaneously with the serrations (light line).

Figure 54 Schematic of obtaining an ideal elongation from the work hardening plot.

Figure 55 Actual and ideal elongations at 300K and at 10^{-4} /s and 10^{-1} /s for a) 6111-T4 and b) AKDQ steel.

Figure 56 Schematic of how the number of oscillations, N, the average amplitude, A, the work hardening drop offs and the necking parameters behave for samples A and B. a) $N_A > N_B$; therefore, it would be expected that $A_A < A_B$, and b) their respective work hardening curves. Sample A has a more gradual drop off, and the necking parameters for A are greater as well.

Figure 57 a) Number of oscillations, b) average amplitude, c) work hardening drop off characteristics and d) necking parameters for 6111-T4 longitudinal tested at 300K with an increase in strain rate from 10^{-4} /s to 10^{-1} /s.

Figure 58 a) Number of oscillations, b) average amplitude, c) work hardening drop off characteristics and d) necking parameters for 6111-T4 longitudinal tested at 10^{-4} /s with an increase in temperature from 300K to 77K.

Figure 59 a) Number of oscillations, b) average amplitude, c) work hardening drop off characteristics and d) necking parameters for 6111-T4 longitudinal tested at 10^{-1} /s with an increase in temperature from 300K to 77K.

Figure 60 a) Number of oscillations, b) average amplitude, c) work hardening drop off characteristics and d) necking parameters for 6111 tested at 10^{-4} /s when the -T4 samples are solution heat treated (SHT).

Figure 61 a) Number of oscillations, b) average amplitude, c) work hardening drop off characteristics and d) necking parameters for 6111 tested at 10^{-1} /s when the -T4 samples are solution heat treated (SHT).

Figure 62 Percent change in mechanical properties for 6111 when the -T4 samples are solution heat treated (SHT) at 300K and a strain rate of a) 10^{-4} /s and b) 10^{-1} /s.

Figure 63 Schematic of how varying the gage width will affect the work hardening behavior. Clusters in a a) wide sample will account for a smaller volume fraction of the gage area while these clusters will constitute a larger volume fraction in the gage area of a narrow sample in b). The work hardening curve for the wide sample will have smaller amplitude oscillations than those for a narrow sample.

Figure 64 Percent change in mechanical properties for 6111-T4 longitudinal samples at 300K and 10^{-4} /s with a change in specimen geometry.

Figure 65 a) Number of oscillations, b) average amplitude, c) work hardening drop off characteristics and d) necking parameters for 6111-T4 tested at 10^{-4} /s and 300K when the gage width is changed.

Figure 66 Hypothesized formation and propagation of deformation islands. a) Deformation will localize in a weak area of the sample; this softening is reflected as a decrease in the slope of the stress-strain curve. b) The island continues to propagate when the local stress can overcome obstacles in the neighboring grains; the slope in the stress-strain curve continues to decrease. c) Island continues to propagate until it cannot overcome hard obstacles in its path; the slope in the stress-strain curve no longer decreases. d) The island hardens without increasing in size; the slope of the stress-strain curve is increasing. The cycle begins again when the island hardens

to the point where it is more favorable to begin deformation in the next weakest area.

LIST OF TABLES

Table 1 Tensile test matrix, 6111-T4.

Table 2 Tensile test matrix, 300K.

Table 3 Textures and Euler angles.

Table 4 Mechanical properties for longitudinal and transverse 6111-T4 at 300K.

Table 5 Mechanical properties of wide and narrow 6111-T4 at 300K.

Table 6 Mechanical properties of transverse 6111 SHT at 300K.

Table 7 Mechanical properties of AKDQ steel at 300K.

Table 8 Mechanical properties of 6061-T6 at 300K.

Table 9 Mechanical properties of 6111-T4 at 77 and 4.2K.

Table 10 Diffusion coefficients of major solutes in 6111-T4.

Table 11 Schmid factors for 6111-T4 textures.

1 INTRODUCTION

1.1 Background

Due to a mandate for designing more fuel efficient cars, the automotive industry has, in recent years, turned from the traditional low carbon steels to lighter weight alternatives such as aluminum alloys. With its higher specific strength, aluminum can be a competitive alternative. Automobiles made entirely of aluminum, e.g. the Honda NSX and the Audi A8, have been introduced, while other models are becoming more aluminum intensive by weight. For outer body panel applications, alloy 6111-T4 (Al-0.76Si-0.61Mg-0.82Cu in w/o) has become a particularly attractive alternative to steel.

Despite the weight savings advantage in substituting aluminum alloys for steel, there are drawbacks to using aluminum. One of the most serious disadvantages is the lower uniaxial tensile elongation of 6111-T4 compared with Aluminum Killed Drawing Quality (AKDQ) steel, a typical outer body panel steel, as shown in figure 1. Since uniaxial tension can be mathematically related to more complex stress-strain states such as those seen in forming operations, this lower elongation indicates lower formability and thus, greater difficulty in forming complex parts. It is therefore desirable to improve the elongation of 6111. To improve the elongation, it is necessary first to understand what factors are affecting the elongation and then to understand how to manipulate these factors such that an increase in elongation can be attained.

There are three factors that can affect the elongation: work hardening rate, inhomogeneous deformation and strain rate sensitivity. The work hardening rate, $\theta = \frac{d\sigma}{d\varepsilon}$, is especially important prior to the onset of necking. For a sheet material deformed in uniaxial tension, the necking criterion is given by

$$\theta = \frac{\sigma}{2} \tag{1.1}$$

where

σ = true stress.

This criterion can be seen graphically in figure 2a. The work hardening rate and $\frac{\sigma}{2}$ can be plotted versus the true strain ε. Where the two curves meet is where the onset of local necking occurs. The onset of necking can be delayed when the work hardening rate is high at higher strains, as shown in figure 2b, therefore increasing the elongation.

The extent of inhomogeneous deformation can also affect the elongation. Deformation inhomogeneities range from the microscopic level of slip bands to macroscopic scale localized deformation that occurs in groups of grains. Localized deformation can manifest itself as deformation concentrating in a few grains, or islands, to deformation occurring in a band which can span the width of a sample (figure 3). Islands which cause macroscopic strain localizations can hasten the onset of a neck, thus affecting the elongation [Gillis and Jones, 1979; Jalinier, Christodoulou, Baudelet and Jonas, 1977].

The critical defect size and shape, due to strain localization, that will cause necking will depend on the material and can be affected by the strain rate sensitivity. For instance, when a deformation band forms in a weak area, it causes a local instability. The strain rate in this band is higher than the strain rate in the rest of the sample. In a strain rate sensitive material, the softening due to the band is quickly damped out due to local hardening. This ability to offset local instabilities is especially important near necking [Ghosh, 1974]. Since aluminum is less strain rate sensitive than steel, it may be more susceptible to premature failure when these bands form, and the critical defect size to cause necking may be smaller than that of steel.

Since it is believed that localized deformation is detrimental to the elongation, improving the elongation would entail manipulating the microstructure in order to reduce the incidence of localized deformation. Various microstructural features can affect the formation and propagation of localized deformation in this alloy: solute distribution, precipitate structure, grain size distribution and local crystallographic texture variations. These features can cause localized deformation to form and propagate by influencing the

stress concentrations at the deformation front. Deformation will propagate when it can overcome local obstacles in the microstructure. The solute distribution and precipitate structure can affect the accommodation of such stresses from grain to grain. The grain size distribution can influence the propagation of deformation through the local grain distribution. If there is a cluster of large sized grains surrounded by a cluster of small sized grains (figure 4a), it can be easier for deformation to proceed through the cluster of large grains because it is softer relative to the cluster of small sized grains.

Texture has been observed to affect the orientation of deformation bands [Robinson and Shaw, 1994]. The orientation of these bands can range from 52° to 66°. In a material that has more than one crystallographic texture present, an inhomogeneous texture distribution may also affect the formation and propagation of the deforming regions. For example, in figure 4b, when a cluster of similarly oriented grains has an orientation different from the surrounding grains and if this cluster of grains is located in a weak area, a few deform first. With increased deformation, it may be easier to continue deforming grains in this cluster, thus localizing the deformation. The size and propagation direction of the localized deformation, of course, still depend on the local stresses. These local stresses arise from the superposition of the global stress distribution and the local stress concentration. Since the localized deformation is macroscopic in size, more macroscopic microstructural features such as local texture variation or grain size distribution will more likely influence the formation and propagation of the localized deformation.

In aluminum alloys, deformation bands have been linked with serrated flow [Kim, et al., 1979; Robinson and Shaw, 1994; Robinson, 1994; Chihab, et. al., 1987; Cetlin, et al., 1973; Reed-Hill and Gulec, 1975; Rodriguez, 1984; Fujita and Tabata, 1977; Phillips and Swain, 1952-3]. An example of this serrated flow in alloy 6061 (Al-1.0Mg-0.6Si w/o) is shown in figure 5 [Robinson, 1994]; the serrations are the short wavelength serrations seen in the inset, and the longer wavelength oscillations will be discussed further in section 6.3.1.1.1. This serrated flow has been attributed to the Portevin-Le Chatelier

(PLC) effect [Portevin and Le Chatelier, 1923; Portevin and La Chatelier, 1924], where the serrations are due to the solute-pinned dislocations breaking free. Deformation bands have been observed to occur in materials exhibiting such serrated flow. Although various researchers have attempted to correlate the serrations and bands [Kim and Chaturvedi, 1979; Chihab, et al., 1987; Cetlin, et al., 1973; Fujita and Tabata, 1977; Phillips and Swain, 1952-3], no direct correlation has been convincingly established. The exact nature of how the PLC effect can affect something on the order of the size of a deformation band is undetermined.

How localized deformation initiates and propagates is still not well understood. Fujita and Tabata have suggested the need for "trigger grains" to nucleate small scale strain localizations [Fujita and Tabata, 1977]. With the yielding of these "trigger grains", neighboring grains deform. They believe that these localizations will grow to the size of a few grains and that bands of deformation correspond to the serrations in the stress-strain curve.

1.2 Physical Metallurgy of 6111-T4

6111 is supplied in the -T4 condition, the condition in which it is used for forming operations. This temper designation refers to a final thermomechanical process that consists of a solution heat treatment, a quench, a 0.5% stretch to increase the flatness of the sheet, and a natural age. In this condition the material will have a microstructure that consists of GP zones and some free solutes. The texture is expected to consist predominantly of the recrystallization texture, where recrystallization textural components such as Cube {100} <001> and Goss {110}<001> are present, with small contributions from the rolling textures such as Brass {110}<112>, Copper {211}<111> and S {123}<634>.

1.3 Objective

The overall purpose of this research is to understand what limits the elongation in 6111. To achieve this objective, there are two specific issues that need to be addressed. First, how deformation proceeds and how it affects the elongation needs to be understood. Second, the mechanism involved in the deformation behavior must be determined. Once this mechanism is identified, then recommendations on the optimal microstructure can be made to obtain the desired improvement in elongation.

2 EXPERIMENTAL PROCEDURE

The material, 6111-T4, used in this investigation was supplied by ALCOA as 0.030 inch thick sheet. This material underwent a final thermomechanical process of a solution heat treatment, a quench, a 0.5% stretch to increase the flatness of the sheet and finally a natural age until stabilized. It was important to characterize the deformation behavior first, to compare the properties with those of AKDQ steel. Then, observations of the surface were necessary to determine the extent of islands occurring in the sample and how it affected the development of the local neck. To determine the microstructural cause of the islands, the material needed to be characterized before testing. In-situ observations during testing were necessary to observe how the islands formed and propagated through the sample.

To characterize the deformation behavior of this alloy, uniaxial tensile tests were performed at three test temperatures (4.2K, 77K and 300K) and five strain rates (10^{-4}, 5 x 10^{-4}, 10^{-3}, 10^{-2}, 10^{-1} /s) in both the longitudinal and transverse directions; the test matrix is shown in Table 1. The temperatures were chosen to determine how deformation behavior changed with decreasing temperature; 77K is the temperature of liquid nitrogen, and 4.2K is the temperature of liquid helium. The changes in temperature are also useful in eliminating different microstructural features and mechanisms when trying to evaluate their effect on the deformation behavior. The strain rates covered the range of strain rates encountered during a typical forming operation. Specimen dimensions are shown in figure 6a and were designed and machined according to a modified ASTM E-8 Standard. For mechanical properties and work hardening comparison purposes, tensile specimens of AKDQ steel (Fe-0.05C w/o), with dimensions shown in figure 6a, were also tested at 300K and at two strain rates (10^{-4}, 10^{-1} /s). For 6111-T4, fractography was performed on tensile samples with an SEM to detect any fracture mode changes at the different test conditions.

As mentioned above, the material was received in the –T4 condition. The microstructure, as reported by others [Bull, Burger, Gupta, Jeffrew and Lloyd, 1994], generally consists of some GP zones and solutes. By solution heat treating, these GP zones will dissolve and the solute population will increase. The effect of solute/precipitate distribution on the deformation behavior was investigated by solution heat treating transverse tensile samples (550 °C for 10 minutes, then ice water quench) and then testing them within 30 minutes of quenching at 300K and at 10^{-4} and 10^{-1} /s.

The effect of specimen geometry on deformation behavior was studied by testing 6111-T4 in three sheet specimen configurations and by testing 6061-T6 sheet and round cross-section tensile samples; 6111-T4 was not available in plate or bar form. The test matrix is shown in Table 2. Because deformation islands and bands are on a macroscopic scale, it is very possible that a larger scale microstructural feature, such as a cluster of grains, is the dominating feature. If the gage width is narrower, the clusters will occupy a greater area fraction of the gage area. Changes in specimen geometry would be reflected in the work hardening oscillations. The effect of varying specimen geometry is further discussed in section 6.3.3.3. Two additional 6111-T4 sheet specimen geometries were tested where the width of the reduced area was made wider and narrower than the standard samples above; they are depicted in figure 7. The gage length, however, remained 25.4 mm (1 in.) for all sample geometries. The wide specimens have a gage width of approximately 13.8 mm (0.545 in) (figure 6b), the standard samples (which are used in the standard tensile tests) are approximately 9.5 mm (0.375 in.), and the narrow samples are 5.1 mm (0.2 in.) wide (figure 6c) [Chan, 1999]. Tensile tests were conducted at 10^{-4} /s and 300K for all three, with one sample for the wide specimen and two for the narrow, and at 10^{-1} /s for the wide (two samples) and standard samples. For 6061-T6, sheet specimens were 0.79 mm (0.031 in.) thick, and the same specimen configuration (figure 6a) as the 6111-T4 standard samples was used. Round cross-section samples [Chan, 1999] were

machined with the dimensions shown in figure 6d. These samples were tested at 300K and at strain rates of 10^{-4} and 10^{-1} /s.

Table 1- Tensile test matrix.

T [K]	Alloy, Orientation	10^{-4} /s	$5x10^{-4}$ /s	10^{-3} /s	10^{-2} /s	10^{-1} /s
300	6111-T4, L	x	x	x	x	x
	6111-T4, T	x	x	x	x	x
	6111 SHT	x				x
	AKDQ Steel	x				x
77	6111-T4, L	x				x
	6111-T4, T	x				x
4.2	6111-T4, L	x				x

Table 2- Tensile test matrix, 300K

Alloy, Geometry	10^{-4} /s	10^{-1} /s
6111-T4, Wide	x	x
6111-T4, Standard	x	x
6111-T4, Narrow	x	
6061-T6, Sheet	x	x
6061-T6, Round Cross-section	x	x

To determine the extent of deformation island and band formation in this material, longitudinal specimens were polished and pulled in tension to various strains at 300K, 77K and 4.2K. Both ex-situ and in-situ observations were made. At 300K and 10^{-4} /s, specimens were polished to 0.05 μm and strained to plastic strains of 1%, 4% and failure. The 77K sample was polished to 600 grit and then strained at 10^{-4} /s to a strain near necking, approximately 27%. At 4.2K, a sample was polished to 0.05 μm and was tested at 10^{-4} /s and 10^{-1} /s to failure. For all of the above samples, ex-situ observations were made with an optical microscope. The resolution of the optical microscopy depends on many factors, such as the objective lens used, etc. Sub-micron resolution is obtained in the

worst case scenario, and this resolution is more than adequate since the feature of interest is on the order of several grain diameters. In addition, in-situ videography during a tensile test was performed on a longitudinal tensile sample that was polished to 600 grit. The test conditions were 10^{-3} /s and 300K; a faster strain rate was chosen such that changes in the deforming surface could be viewed more quickly.

The onset of diffuse and local necking needed to be determined. Tensile specimens were marked at approximately 1.3 mm (0.05 in.) intervals in the gage section, and both width and thickness measurements were taken before and after straining. Six specimens were tested at 300K at a strain rate of 10^{-4} to various strains: before the onset of diffuse necking (15.99%, 20.11%, 20.59%; BDN1, BDN2, and BDN3, respectively), after the onset of diffuse necking but before the onset of local necking (18.70% and 22.59%; DN1 and DN2, respectively), and after the onset of local necking (21.36%, LN).

The microstructure needed to be characterized by both optical microscopy to determine grain size, grain distribution and degree of clustering of similar sized grains and Electron Backscattered Pattern (EBSP) Microscopy to determine the degree of clustering of similarly oriented grains. For optical microscopy, the samples were mechanically polished to 0.05 μm and then etched with Keller's Reagent (2.5% HNO_3, 1.5% HCl, 0.5% HF, H_2O bal.). Grain size statistics were analyzed using NIH Image 1.62. For grain orientation characterization, sub-sized specimens (figure 6e), prior to tensile testing, were mechanically polished to 0.05 μm. The polishing solution for the 0.05 μm step was an alumina and colloidal silica suspension of pH 9. Grain orientations in a 7 mm x 2.5 mm (233 x 83 grains) region in the middle of the gage section were determined. The sampling mesh had a pitch of 50 μm.

3 MATERIAL CHARACTERIZATION RESULTS

3.1 Optical Microscopy and SEM

From the optical microscopy, it does appear that there is clustering of similar sized grains. In figure 7a, clusters of larger sized grains (those greater than approximately 50 μm) are colored in figure 7b (the same micrograph as in 7a). Smaller sized grains are also observed to cluster in these micrographs. The clusters of large sized grains can act as soft areas in the specimen while the clusters of small sized grains can act as hard areas. The grain size analysis reveals that the average grain size is approximately 30 μm. A histogram of the grain size distribution is shown in figure 8. There is a large population of grains around 4-5 μm, and the distribution is skewed towards the smaller grain sizes. In addition, a rather large population of a secondary phase is visible. From SEM EDS analysis, the secondary phases have several different compositions: Al-Mg-Cu, Al-Fe-Mn-Si-Cu and Al-Fe-Mn-Mg-Si-Cu. Exact compositions were not determined because standards were not available, and the area sampled included the matrix. The presence of such a large population of inclusions could influence the void population when the specimen begins to neck; the implications of this observation will be discussed in section 6.2.1.

3.2 EBSP

Grain orientation can be determined by performing EBSP in the scanning electron microscope (SEM) [Adams, Wright and Kunze, 1993; Michael and Goehner, 1993; Dingley, 1984; Dingley and Baba-Kishi, 1990; Randle, 1992]. When an incident electron beam enters the specimen, electrons are scattered, elastically and inelastically, in all directions. Electrons that are backscattered from the specimen are collected through a detector. Those backscattered electrons that satisfy the Bragg condition diffract to form pairs of bright (excess) and dark (defect) lines, or Kikuchi lines [Michael and Goehner, 1993]; the arrangement of these Kikuchi lines, called a Kikuchi pattern, are related to the

specimen crystallographic structure and orientation [Edington, 1975; Thomas, 1962]. With a polycrystalline specimen, the orientation of a particular grain can be obtained.

Microtexture information can be determined in the following manner. Two axes are needed; there is the reference crystal axes, x_c, y_c, and z_c, and the grain axes, x_g, y_g, and z_g. The crystal axes can be brought into coincidence with the grain axes by performing three successive rotations: 1) rotation of φ_1 about the z_c axis, 2) rotation of Φ about the x_c axis and 3) rotation of φ_2 about the z_c axis [Randle, 1992]. The angles φ_1, Φ and φ_2, using Bunge's convention [Bunge, 1982], are also known as Euler angles and describe the orientation of the grain. These angles can be used to calculate a 3 x 3 orientation matrix which represents a three dimensional orientation with respect to the reference axes. Each element, a_{ij}, can be calculated by the following equations:

$$
\begin{aligned}
a_{11} &= \cos\varphi_1\cos\varphi_2 - \sin\varphi_1\sin\varphi_2\cos\Phi \\
a_{12} &= -\cos\varphi_1\sin\varphi_2 - \sin\varphi_1\cos\varphi_2\cos\Phi \\
a_{13} &= \sin\varphi_1\sin\Phi \\
a_{21} &= \sin\varphi_1\cos\varphi_2 + \cos\varphi_1\sin\varphi_2\cos\Phi \\
a_{22} &= -\sin\varphi_1\sin\varphi_2 + \cos\varphi_1\cos\varphi_2\cos\Phi \\
a_{23} &= -\cos\varphi_1\sin\Phi \\
a_{31} &= \sin\varphi_2\sin\Phi \\
a_{32} &= \cos\varphi_2\sin\Phi \\
a_{33} &= \cos\Phi
\end{aligned}
\tag{3.1}
$$

Then, by performing a series of matrix operations and transformations (see Appendix A [Krenn, 1996]), a misorientation angle can be calculated between the grain orientation and the ideal orientation. There are several ideal recrystallization and rolling textures expected in 6111-T4: Cube, Goss, R, P, Q, Brass, Copper and S; their Euler angles are listed in Table 3. Those grains that have an angle of misorientation less than 15° are considered as

the ideal orientation. For instance, if a grain has a misorientation angle of 10° from the Goss texture, then it is considered to have the Goss texture.

This experiment was performed to confirm that there is clustering of similarly oriented grains. From the optical microscopy, it is expected that there is clustering of similarly oriented grains. Previous researchers have also confirmed the existence of clustering of similarly oriented grains [Bryant, Beaudoin, and Demeri, 1996]. If there is clustering of similarly oriented grains, then it is strong evidence that this microstructural feature can facilitate island formation and propagation. It is also expected that the predominating texture should consist of the recrystallization textures; some retained rolling texture will be present. If clustering of similarly oriented grains follows that same angle or directionality as the island, then it is very strongly possible that the similarly oriented grains will be one of the dominant mechanisms behind the island formation and propagation. The Euler angles for each measured point in the gage section that were determined. Then, by calculating the orientation matrix with equation 3.1 above for each point measured, the misorientation angle between the point, or grain, and the ideal textures listed in Table 3 was determined. If the misorientation angle fell within 15° of an ideal orientation, it was considered that orientation. Since the x (longitudinal direction) and y (transverse direction) coordinates for each measured point is also known, the spatial location of each orientation can be made.

The data can be plotted in two ways. A 3D plot of Euler angles Φ, φ_2, and φ_1 (x, y and z axes, respectively) can be used to show any preferred orientations (figure 9a). For example, if there is clustering of similarly oriented grains for a particular orientation, then there would be a large population of grains in a certain region in the plot. The location of clusters of similarly oriented grains in the gage section can be seen by plotting grains of a particular orientation at their x, y coordinates. In figure 10, grains of a particular orientation, in the gage section, are the black spots. Any clustering that is present will be easily seen.

Three things are apparent from the EBSP microscopy. First, there is strong texturing in this 6111-T4. In figure 11, a plot of the Euler angles in Euler space, there are areas where the data points cluster. The clustering at 180° is due to the 180 degree symmetry. Second, from the x-y plots in figure 12(a-h), the Cube texture (figure 12a) is the predominant texture in the material; this result has been reported elsewhere [Bryant, Beaudoin, and Demeri, 1996]. Plots were made where the grains within 15° of the ideal orientation were plotted as light areas at their respective x and y coordinates in figure 12. The S texture (figure 12h) is next most common; the order of texture abundance is listed in Table 3 with "1" as the most abundant and "8" the least abundant. Third, there is clustering of similarly oriented grains. For the Cube texture (figure 12a), there are clusters of grains with the Cube orientation; many of these clusters have a directionality to the tensile axis. In the S orientation (figure 12h) there is a directionality to the distribution as well. The grains align at an angle to the rolling direction/tensile axis. If the island forms and propagates in the same direction, then this evidence supports the theory that clustering of similarly oriented grains is one feature that dominates the formation and propagation of islands. Implications of these results will be further discussed below.

Table 3- Textures and Euler Angles

Orientation	{hkl}<uvw>	Texture Type	φ_1	Φ	φ_2	Abundance
Cube	{100}<001>	Recrystallization	0	0	0/90	1
Goss	{110}<001>	Recrystallization	0	45	0/90	5
R	{124}<211>	Recrystallization	53	36	60	4
P	{011}<122>	Recrystallization	65	45	0/90	8
Q	{013}<231>	Recrystallization	45	15	10	3
Copper	{112}<111>	Rolling	90	30	45	7
Brass	{011}<211>	Rolling	35	45	0/90	6
S	{123}<634>	Rolling	59	34	65	2

3.3 Fractography

The fracture surface of 6111-T4 longitudinal and transverse specimens (10^{-4} /s, 10^{-1} /s, 300K, 77K and 4.2K) were examined using an SEM to detect any changes in fracture mode when the strain rate or temperature changes. Typical fracture surfaces are shown in figure 13 (longitudinal) and figure 14 (transverse). For the longitudinal samples at 300K and 10^{-4} /s (figure 13a), the fracture mode is ductile, and the surface has a fine dimple structure. When the strain rate is increased to 10^{-1} /s (figure 13b), the dimple size increases, and the dimple walls appear less planar. At 77K, the fracture micromode at 10^{-4} /s (figure 13c) is ductile. Small dimples and slip steps decorate the larger dimple walls. With an increase in strain rate to 10^{-1} /s (figure 13d), the fracture surface does not significantly change in appearance; the micromode is still ductile. A larger population of microcracks is seen at this test condition. With a decrease in test temperature from 300K to 77K at constant strain rate, the fracture micromode remains ductile for both strain rates (figures 13 c and 13d). At both strain rates at 77K, the void walls are more planar, and there are more microcracks. In addition, there are very small voids between the planar walls. Slip steps are also seen on the void walls. When the test temperature is further decreased to 4.2K (strain rate at 10^{-1} /s), shown in figure 13e, there is an increase in microcracks, and the fracture surface is more facetted in appearance, as though the fracture occurred on crystallographic planes.

Similar observations can be made for the transverse samples. At 300K and 10^{-4} /s (figure 14a), the fracture mode is ductile; there are small dimples in the surface. With an increase in strain rate to 10^{-1} /s (figure 14b), the fracture micromode remains ductile, the dimple size increases, and the void walls are less planar. At 77K and 10^{-4} (figure 14c), the fracture micromode is ductile and slip steps can be seen on some of the void walls. The dimples are larger as well, and there are more microcracks. When the strain rate is increased to 10^{-1} /s (figure 14d), the dimple size increases. Decreasing the test temperature

from 300K to 77K while holding the strain rate constant produces a larger dimple size, more planar void walls, and more microcracking. Despite the decrease in test temperature and strain rate for both orientations, the fracture micromode remains ductile.

3.4 Summary

The microstructure was characterized using optical microscopy, SEM and EBSP microscopy. The fracture surfaces were characterized by SEM. There is clustering of large sized grains as well as clustering of similarly oriented grains. There is also a sizable inclusion population. The fracture micromode remains ductile for all orientations, test temperatures, and strain rates (10^{-4} and 10^{-1} /s).

4 MECHANICAL PROPERTIES RESULTS

4.1 300K Tensile Tests

4.1.1 6111-T4 Longitudinal

The mechanical properties of longitudinal specimens are given in Table 4, and the engineering stress-strain curves are shown in figure 15. When the strain rate is increased, there is no significant variation in yield or ultimate strength. The elongation (at $\theta = \frac{\sigma}{2}$) and total elongation decrease slightly with a change in strain rate from 10^{-4} to 10^{-2} /s but then decrease more sharply at 10^{-1} /s. The slight changes in the mechanical properties are reflected in their stress-strain curves; their tensile behaviors do not significantly change with changes in strain rate.

4.1.2 6111-T4 Transverse

The mechanical properties of transverse samples are listed in Table 4, and their engineering stress-strain curves are shown in figure 16. The yield strengths are approximately 10% lower than those in the longitudinal direction while the elongations are nearly the same. Again, the yield and ultimate strengths do not vary significantly with increasing strain rate. The elongations peak at 10^{-3} /s, but as the strain rate increases, the elongations at $\frac{\sigma}{2}$ remain slightly higher than those at 10^{-4} /s. The engineering stress-strain behavior does not vary significantly with changes in strain rate.

Table 4- Mechanical Properties for longitudinal and transverse 6111-T4 at 300K.

Orientation	Strain Rate /s	YS [MPa]	UTS [MPa]	Elong. [%]	TE [%]
L	10^{-4}	197	324	26.37	28.03
	5×10^{-4}	198	330	26.45	28.38

	10^{-3}	195	326	25.18	27.44
	10^{-2}	194	328	25.21	27.08
	10^{-1}	198	323	23.68	24.71
T	10^{-4}	175	318	26.57	28.66
	5×10^{-4}	173	316	25.66	27.29
	10^{-3}	174	318	29.21	30.90
	10^{-2}	174	318	26.04	27.96
	10^{-1}	173	316	24.77	27.52

4.1.3 6111-T4 Wide and Narrow Samples

The mechanical properties for wide and narrow samples are listed in Table 5, and their engineering stress-strain curves are shown in figure 17. The yield and ultimate strengths remain virtually the same when the gage width decreases from wide to standard to narrow width. At a strain rate of 10^{-4} /s, the elongation at $\frac{\sigma}{2}$ and the total elongation peak at the standard sample width and are lowest in value for the narrow samples. At a strain rate of 10^{-1} /s, both elongations decrease slightly with decreasing gage width. The variation in geometry has only a minor effect on the stress-strain behavior.

Table 5- Mechanical properties of wide and narrow 6111-T4 at 300K.

Geometry	Strain Rate /s	YS [MPa]	UTS [MPa]	Elong. [%]	TE [%]
Wide	10^{-4}	196	324	25.32	26.73
	10^{-1}	198	323	23.81	25.61
Narrow	10^{-4}	194	326	22.46	23.98

4.1.4 6111 Transverse Solution Heat Treated

Tensile samples were solution heat treated prior to testing at 10^{-4} and 10^{-1} /s to alter the solute/precipitate structure. The mechanical properties in Table 6 show that the solution heat treatment lowers the yield and ultimate strengths and increases the elongations; the total elongation actually decreases slightly at 10^{-1} /s. For the solution heat treated specimens, an increase in strain rate causes a decrease in the strengths and a decrease in the elongations. The engineering stress-strain behavior, figure 18, do change with increasing strain rate. The stress level decreases with increasing strain rate.

4.1.5 AKDQ Steel

Tensile tests were also performed on AKDQ steel to provide a mechanical properties reference for comparison with 6111-T4. The mechanical properties are listed in Table 7. The elongation of AKDQ steel is greater than that of 6111-T4. Their engineering stress-strain behavior (figure 19) show a greater change, as compared with 6111-T4, when the strain rate increases. Since the aluminum alloys are less strain rate sensitive, this observation is expected.

Table 6- Mechanical properties of transverse 6111 SHT at 300K.

Strain Rate /s	YS [MPa]	UTS [MPa]	Elong. [%]	TE [%]
10^{-4}	78	234	28.22	29.16
10^{-1}	76	201	25.52	27.48

Table 7- Mechanical properties of AKDQ steel at 300K

Strain Rate /s	YS [MPa]	UTS [MPa]	Elong. [%]	TE [%]
10^{-4}	154	301	38.56	49.05
10^{-1}	192	328	32.32	44.82

4.1.6 6061-T6 Sheet

6061-T6 sheet mechanical properties do not vary significantly with a change in strain rate (Table 8). With an increase in strain rate, the yield and ultimate strengths remain virtually the same. The total elongation decreases slightly while the elongation shows a somewhat larger decrease. Changes in strain rate do not affect the stress-strain behavior significantly (figure 20).

4.1.7 6061-T6 Round Cross-Section

Yield and ultimate strengths increase slightly with increasing strain rate (Table 8). The uniform elongation slightly increases and total elongation slightly decreases. The strengths are lower than the sheet samples. The total elongations, however, are significantly greater than those of the sheet specimens. When the strain rate increases, the stress-strain behavior (figure 20) changes slightly.

Table 8- Mechanical properties of 6061-T6 at 300K

Geometry	Strain Rate /s	YS [MPa]	UTS [MPa]	UE [%]	Elong. [%]	TE [%]
Sheet	10^{-4}	311	352		12.17	14.82
	10^{-1}	316	357		11.43	14.49
Bar	10^{-4}	283	320	10.20		20.93
	10^{-1}	290	321	10.26		20.38

4.2 77K Tensile Tests

4.2.1 6111-T4 Longitudinal

The mechanical properties of 6111-T4 longitudinal samples at 77K are listed in Table 9, and the stress-strain curves are shown in figure 21. Lowering the test temperature increases the yield and ultimate strengths and the elongation and total elongations. At 77K, the yield and ultimate strengths increase slightly with increasing strain rate. The elongation and total elongation both increase with increasing strain rate. At this temperature, as compared to the 300K data, there is a greater change in stress-strain behavior when the strain rate increases.

4.2.2 6111-T4 Transverse

Transverse mechanical properties at 77K are given in Table 9, and the stress-strain curves are plotted in figure 21. With a decrease in test temperature, the strengths and elongations increase significantly. When the strain rate is increased at 77K, the strengths and elongations increase. A greater change with increasing strain rate is seen at this temperature, as compared with the results at 300K, but the difference is not as great as that seen for the longitudinal samples.

4.3 4.2K Tensile Test

4.3.1 6111-T4 Longitudinal

One tensile test was performed at 10^{-4} /s and 10^{-1} /s each. The strengths and elongations are listed in Table 10. With the decrease in temperature from 77K, the yield and ultimate strengths increase, and the elongations decrease. At 4.2K an increase in strain rate increases the yield strength but decreases the UTS; the elongation increases while the total elongation decreases only slightly.

Table 9- Mechanical properties of 6111-T4 at 77 and 4.2K.

Temperature [K]	Orientation	Strain Rate /s	YS [MPa]	UTS [MPa]	Elong. [%]	TE [%]
77	L	10^{-4}	247	430	31.33	32.13
		10^{-1}	266	469	34.92	36.08
	T	10^{-4}	237	428	31.92	32.85
		10^{-1}	248	447	37.78	40.00
4.2	L	10^{-4}	317	564	25.61	27.52
		10^{-1}	400	510	26.02	27.25

4.4 Summary

Tensile tests were conducted on 6111-T4 at several temperatures (300K, 77K, 4.2K), strain rates (10^{-4}, 5 x 10^{-4}, 10^{-3}, 10^{-2}, 10^{-1} /s), orientations (longitudinal and transverse), microstructures (-T4, SHT) and geometries (wide, standard, narrow). In addition, tensile tests were performed on AKDQ steel to provide a basis of comparison and on 6061-T6 (sheet, round cross-section) to determine the effect of specimen geometry on the mechanical properties. First, the mechanical properties of 6111-T4 were not strain rate sensitive at constant temperature (300K, 77K), geometry (wide, standard) or microstructure (-T4, SHT). Second, a change in test orientation decreased the yield and

ultimate strengths. Third, a change in geometry for 6111-T4 did not significantly affect the yield and tensile strengths. Fourth, the yield and ultimate strengths decreased and the elongation at $\frac{\sigma}{2}$ and total elongation increased when the –T4 samples were solution heat treated. Fifth, decreasing the test temperature from 300K to 77K produced an increase in all the mechanical properties, while a further decrease in temperature to 4.2K decreased the elongation and total elongation from their 77K values. Sixth, for 6061-T6 changing the specimen geometry from sheet to round cross-section decreased the yield and ultimate strengths, and increased the total elongations. Finally, AKDQ steel has much higher elongations than 6111-T4.

5 WORK HARDENING AND DEFORMATION BEHAVIOR RESULTS

A plot of work hardening rate, $\theta = \frac{d\sigma}{d\varepsilon}$, versus true strain, ε, is useful in assessing how stable the deformation behavior is. A schematic work hardening rate versus true strain curve is shown in figure 22a. Relative increases and decreases in the work hardening can indicate local stabilizations and instabilities during deformation. If the assumption is made that various weak areas in the gage are experiencing instabilities and stabilizations, then the oscillations in the work hardening curve can be attributed to this local behavior. If these oscillations are present, it is also necessary to determine what causes them by examining how test parameters, microstructure and specimen geometry affect the oscillation behavior. Another regime where deformation stability can be important is the region between diffuse necking and failure. As illustrated in the figure, a sharp drop off before final failure in a specimen can imply very unstable deformation behavior in response to the presence of islands or deformation bands. If the drop-off before final failure is more gradual (figure 22b), then the macroscopic deformation behavior is not as unstable, and the specimen should not approach failure as quickly.

5.1 6111-T4 Longitudinal

Oscillations were present at all test conditions (figures 23 and 24), and the character of the oscillations did change with test conditions. At 300K, with increasing strain rate (figure 23), the number of oscillations generally decreased and the oscillation amplitude generally increased. The drop offs are more gradual at the higher strain rates. In addition, at 300K and 10^{-4} /s, about one-third of the test specimens exhibit more gradual drop-offs (figure 23f); these specimens also have higher elongations. The implications of these results will be discussed in section 6.2. At 77K increasing the strain rate again produces fewer oscillations and a more gradual drop off (figure 24).

The effect of decreasing the test temperature at constant strain rate on the oscillations and drop off varies. At either strain rate, a decrease in test temperature produces more oscillations (figure 25). The sharpness of the work hardening drop off depends on the strain rate. At 10^{-4} /s, the drop off is slightly sharper at 77K, and the opposite is true at 10^{-1} /s. The effect of decreasing test temperature will be further discussed in section 6.3.3.1.

One possible mechanism for these oscillations is the PLC effect that was mentioned earlier. The tests conducted at 77K are well below the temperature regime in which the PLC effect exists, yet the oscillations still occur at 77K. The character does change with the decrease in temperature, but the presence of the oscillations indicates that the PLC effect is not the dominant mechanism. Another mechanism or mechanisms is likely responsible for the change in oscillation character.

5.2 6111-T4 Transverse

For the transverse samples oscillations were present at all strain rates and temperatures (figures 26 and 27). At 300K (figure 26) the number of oscillations again generally decreased with increasing strain rate, although at 10^{-3} /s, the number increased. The drop offs are more gradual at the higher strain rates. At 77K (figure 27) fewer oscillations and a more gradual drop off occur at the higher strain rate. When the strain rate is held constant (figure 28), the number of oscillations increases with a decrease in temperature for both strain rates. At 10^{-4} /s the drop off becomes sharper while at 10^{-1} /s the drop off becomes more gradual with the decrease in temperature.

5.3 6111-T4 Wide

The work hardening curves for longitudinal samples with a wider gage section, tested at 300K and at strain rates of 10^{-4} and 10^{-1} /s, are shown in figure 29. Oscillations are still present in the work hardening curve when the gage width increases. When the

work hardening curves are compared with those from the standard samples, the number of oscillations is about the same as that for the standard samples. Compared to the standard samples, the number of oscillations is about the same and the drop offs are more gradual.

5.4 6111-T4 Narrow

Longitudinal samples with a narrower gage section were tested at 300K and at a strain rate of 10^{-4} /s; the work hardening curves are shown figure 30. Oscillations are present in this sample geometry. Compared to the standard samples, the narrow samples have about the same number of oscillations, but the oscillation amplitudes are clearly larger. The drop off is also much sharper.

5.5 6111 SHT

Transverse samples were solution heat treated to dissolve the GP zones and to increase the solute content. The work hardening curves for specimens tested at 300K and at strain rates of 10^{-4} /s and 10^{-1} /s are in figure 31. At both strain rates, oscillations are present. When the strain rate is increased, the number of oscillations decreases, and the amplitude of the oscillations decreases. These oscillations, when compared with the –T4 oscillations, are greater in number, and have greater amplitude. Also, the drop off is sharper at both strain rates.

5.6 6061-T6

5.6.1 Sheet

The work hardening curves for 6061-T6 sheet specimens are in figure 32a. Oscillations are present at both strain rates (10^{-4} and 10^{-1} /s). At 10^{-4} /s, more oscillations occur at 10^{-4} /s, and the drop off is sharper at this strain rate. At 10^{-1} /s, however, the drop off occurs earlier in the work hardening curve, prior to the onset of local necking. When

the strain rate increases, the number of oscillations decreases, and the drop off is more gradual.

5.6.2 Round Cross-Section

6061-T6 round cross-section samples were tested at 300K and at strain rates of 10^{-4} /s and 10^{-1} /s. Oscillations are present at 10^{-4} /s but not at 10^{-1} /s (figure 32b). The drop off is sharper at the higher strain rate.

5.7 AKDQ Steel

Work hardening curves for AKDQ steel (300K, 10^{-4} /s and 10^{-1} /s) are shown in figure 33. In this non-PLC alloy, oscillations are present at both strain rates. In addition, when the strain rate is increased, the number and amplitude of the oscillations increases.

5.8 Summary

The work hardening curves of specimens at various test conditions and microstructures were examined to characterize the deformation behavior. Oscillations were observed in every condition except for the 6061-T6 round cross-section samples at 300K and 10^{-1} /s. Generally, when the strain rate increased at constant temperature, the number of oscillations decreased, and the work hardening drop off was more gradual. For 6111-T4, when the test temperature decreased at 10^{-4} /s, the number of oscillations decreased, and the work hardening drop off was sharper. At 10^{-1} /s, however, the number of oscillations increased with the lower test temperature.

5.9 Surface Observations

To determine if the oscillations were due to islands, and to observe how these areas formed and propagated, polished and strained samples were observed in-situ visually and with a video camera, and ex-situ with an optical microscope. At the test conditions of

300K and 10^{-4} /s, islands could be seen forming, visually, in several areas in the gage section. As the strain increased, more islands formed. These results were confirmed with the in-situ videography where the tensile test was conducted at 10^{-3} /s and 300K. From the optical micrograph in figure 34a, it is evident that islands (arrows) appear on a sample strained to 1% plastic strain; a lower magnification view is shown in figure 34b. Islands, each approximately 40 μm wide and ranging from 400 to 800 μm long, clustered together in this particular area. There was a corresponding rise in the work hardening rate of this sample. Observations on samples plastically deformed to higher strains revealed that additional areas on the sample underwent a similar deformation pattern. These areas were difficult to capture on the optical microscope due to the intensity of the general background out-of-plane grain rotation and the angle of illumination. One specimen strained to near necking (10^{-4} /s, 77K) had two sample wide deformation bands, and there was a corresponding a peak in the work hardening oscillation. From the sample shown in figure 34, islands were easily observable at strains as low as 1%. In addition, there is an indirect correlation between the occurrence of an oscillation and the formation and propagation of islands. Higher magnification optical micrographs of a 300K, 10^{-4} /s fractured sample showed intense slip in some grains but not in adjacent grains (figure 35). Several neighboring grains also had the same slip direction; this observation indicates that these grains have the same orientation, that there is clustering of similarly oriented grains, and that deformation propagates through such a cluster.

Ex-situ observations of the specimen tested at 4.2K and 10^{-4} /s reveal that several deformation bands formed in the gage section (figure 36). Out-of-plane grain rotation can also be observed on the specimen. The most significant observation is the presence of a deformation band at the fracture surface.

5.10 Necking Measurements

Quantitative analysis of the necking behavior can be performed through the width and thickness measurements. Then, the thickness and width engineering strains, obtained by the equations

$$\varepsilon_t = \frac{t_f - t_i}{t_i} \tag{5.1}$$

$$\varepsilon_w = \frac{w_f - w_i}{w_i} \tag{5.2}$$

where

$\varepsilon_{t,w}$ = thickness, width engineering strain, respectively,

$t_{f,i}$ = final and initial specimen thickness, respectively, and

$w_{f,i}$ = final and initial specimen width, respectively,

can be plotted versus their positions in the gage section. Any diffuse or local necking will become obvious in the plots when there is an increase in strain in a localized area along the gage.

Six specimens were deformed to various strains: before diffuse necking at 15.99% true strain (BDN1), 20.11% (BDN2), and 20.59% (BDN3); after the onset of diffuse necking but before the onset of local necking at 18.70% (DN1) and 22.59% (DN2); and after the onset of local necking at 21.36% (LN). Their work hardening curves are shown in figure 37. The engineering strain at approximately 1.3 mm (0.05 in.) intervals along the width and thickness directions are shown in figures 38 and 39. Since the final gage length differs for each specimen, the x-axis is the position in the gage section normalized to 1. The corresponding work hardening state is shown schematically in the figures. Generally, it would be expected that the thickness strains are higher than the width strains after the onset of local necking since this direction is less constrained and can therefore deform more easily.

It has been found that diffuse and local necking can occur before the theoretical prediction. BDN1 (figure 38a), as expected, does not exhibit diffuse or local necking in the width direction. In the thickness direction (figure 38b), however, there does appear to

be some thinning near the 0 position. This thinning may be the onset of diffuse necking. BDN2, which was strained to before the onset of diffuse necking, does show thinning in both width (figure 38a) and thickness (figure 38b). Again, diffuse necking could be occurring before the theoretical prediction. Further evidence of diffuse necking occurring before the theoretical prediction is exhibited by BDN3. In both thickness (figure 38b) and width (figure 38a) directions, there is a very clear diffuse neck in the gage section. Additionally, this sample exhibits the signs of a local neck, at around 0.35-0.55, within the diffuse neck. This appearance of a local neck occurs before the theoretical prediction. DN1 (figure 39b) has a diffuse neck between 0 and 0.45 in the thickness direction; the rest of the diffuse neck is probably occurring outside the measured area. There appears to be a sharper dip at about 0.75. In the width direction (figure 39a), there is a narrower section from 0 to 0.2. DN2 shows a broad, diffuse neck in both width (figure 39a) and thickness (figure 39b) direction, between 0 and 0.65 to 0.8. There is also a local neck between 0.3 to 0.65.

In the LN sample, it is expected that a local and diffuse neck will be found. From figures 39a and 39b, it is clear that a diffuse neck has formed in both directions. The narrowest and thinnest region occurs near the 0.1 position and indicates that a local neck exists in that area. Because measurements were not taken outside of the gage area, it is difficult to ascertain the exact size of the diffuse and local necks.

5.11 Fractography

The fracture surfaces of 6111-T4 longitudinal samples at 300K (10^{-4}, 10^{-1} /s), 77K (10^{-4}, 10^{-1} /s) and 4.2K (10^{-1} /s) were examined to determine whether any change in fracture mode had occurred (figure 13). As the temperature decreases, the fracture surface becomes more planar. Despite the drastic decrease in test temperature and strain rate, the fracture micromode remains ductile.

5.12 Summary

From examination of the work hardening curves, test specimen surface, necking measurements, and fractography, a number of observations can be made. First, there are oscillations in the work hardening curve. Second, these oscillations change in character with the test conditions and microstructure. Third, islands form on the specimen surface at strains as low as 1% plastic strain. Fourth, there is an indirect correlation between the oscillations and the formation and propagation of the islands and deformation bands. Fifth, at 4.2K there was a deformation band at the fracture surface. Sixth, diffuse and local necks can form before the theoretical predictions. Finally, the fracture micromode remains ductile when the test temperature and strain rates have decreased by nearly two and three orders of magnitude, respectively.

6 DISCUSSION

The overall objective of this project was to understand what factors limit the elongation in 6111-T4. This goal can be achieved by understanding how deformation proceeds and how it affects the elongation, and by determining the mechanism behind the deformation behavior that limits the elongation. There are many factors that can affect elongation: strength effects, material properties, inhomogeneous deformation and microstructure. It is widely accepted that there is an inverse relationship between strength and elongation; the higher the strength the lower the elongation. Material properties such as strain rate sensitivity and work hardening capacity, as mentioned in section 1.1, will also affect elongation; strain rate sensitive materials are better able to damp out areas of local softening before strain localizes too heavily in that area. High work hardening at high strains can delay the onset of necking (fig.2b). Inhomogeneous deformation can limit elongation if strain concentrates in one area of the sample and triggers the premature onset of local necking. Microstructure, such as high inclusion population, solute/precipitate structure, clustering of similarly oriented grains and clustering of large sized grains can influence the localization of deformation. From the 300K, 10^{-4} /s tensile tests, approximately one-third of the tensile samples area able to maintain more stable deformation which results in higher elongation. How these samples are able to achieve greater elongation is a particularly important piece of information because it may provide the answer to improving the overall elongation of 6111-T4. From in-situ and ex-situ observations and optical microscopy of the tensile specimen surfaces, there are two possible mechanisms that can limit the elongation: void growth and coalescence due to a high inclusion population and deformation island and band formation and propagation.

In this section, the effect of these factors on the deformation behavior and elongation will be discussed. First, strength effects on the elongation will be examined. Second, the effect of high inclusion population and void growth will be considered in

relation to the deformation behavior of the more stable tensile samples. Third, the deformation behavior of 6111-T4 will be covered. Fourth, the effect of test variables, microstructure, and specimen geometry will be explored. Finally, evidence that islands are limiting the elongation will be presented, and a model for the deformation behavior will be introduced.

6.1 Strength effect on the elongation

There is usually an inverse relationship between strength and elongation: for a given change in microstructure or test condition, if the strength increases, the elongation decreases. If changes in elongation were purely due to changes in strength, then it would generally be expected, for example, that if the strength increases, the elongation would decrease. For 6111-T4, the changes in elongation with different test conditions and microstructures are not always attributable to the changes in strength. To examine the strength effects on elongation for longitudinal samples, a bar chart of the percent change in mechanical property (yield strength, UTS, elongation at $\frac{\sigma}{2}$, and total elongation) with a change in test condition is presented in figures 40 and 41. The percent change for an increase in strain rate, at constant temperature, is shown in figure 40 and the percent change for a decrease in test temperature, at constant strain rate, is shown in figure 41. When the strain rate is increased, the longitudinal samples at 300K show a slight increase in yield strength and the elongation decreases. At 77K both yield and ultimate strengths increase, and the elongations increase as well. When the strain rate is held constant and the temperature is decreased from 300K to 77K (figure 41), no inverse relationship is seen between the changes in strengths and elongations; instead, with the increase in strengths, the material experiences an increase in both elongations. Therefore, at 300K, the decrease in elongation (at $\frac{\sigma}{2}$) that accompanies an increase in strain rate can be explained, in part, by the increase in strength. For the three other conditions (increase in strain rate at 77K, decrease in temperature at 10^{-4} /s, and decrease in temperature at 10^{-1} /s), strength effects

cannot explain the increases in elongation. Testing at 77K reverses the inverse relationship between strength and elongation. This effect has been seen in other aluminum alloys such as 2090-T81 [Glazer, 1989; Chu, 1990; Tseng, 1993]. At 77K another mechanism is influencing the elongation.

For the transverse samples, the expected inverse relationship between strength and elongation is not seen for a given change in strain rate (figure 42) or temperature (figure 43). The increase in elongation, therefore, is not due to a decrease in strength, since the strengths also increase. Again, another mechanism is responsible for the increase in elongation.

6.2 Stable vs. Unstable Deformation at 300K, 10^{-4} /s

At 300K and 10^{-4} /s, approximately one-third of the test samples are able to attain greater elongation than the rest of the samples: 29.0% (stable) vs. 19.9% (unstable). The work hardening behavior reveals that the stable samples have a more gradual drop off near the necking criterion (figure 23f). This more gradual decrease in work hardening implies more stable deformation behavior at the higher strains. If the work hardening rate is able to maintain a value high enough, it can delay the onset of necking and therefore increase the elongation (section 1.1). Of particular interest is what microstructural feature or mechanism determines the degree of stability of the deformation behavior at high strains. If this feature or mechanism can be identified, then improvements in the elongation can be made by modifying the microstructure. As mentioned earlier in this section, two possibilities exist: high inclusion population and deformation island band formation and propagation.

6.2.1 The Role of Voids in Early Failure

Voids play an important role in the mechanism of necking and failure in a material. They can either cause the early onset of local necking, or hasten failure once local necking

has occurred. In the former case, if a significant void population exists in a tensile sample prior to deformation, the voids can trigger the early onset of necking because of the reduction in net cross sectional area. In this case the voids will create a locally weak area, and as the applied strain increases, deformation concentrates in this area. When the strain localization causes a defect to reach a critical size and shape [Gillis and Jones, 1979], a local neck will begin to form. Thus, with a higher initial void population, a deformation band will form sooner, reach a critical size and shape more quickly, and thereby cause the early onset of local necking. In the latter case, voids nucleate either at the interface between a particle and the matrix by decohesion of the particle/matrix interface or by fracture of the particle. When the applied strain sets up a sufficient hydrostatic stress component in the vicinity of the particles, which occurs at the onset of local necking in sheet specimens in uniaxial tension, voids will then begin to grow. As the voids grow, the local stresses begin to concentrate and necking instabilities develop locally [Anderson, 1995; McClintock, 1971]. Finally, voids begin to coalesce and eventually lead to failure. With a large population of weak or weakly bonded inclusions, once a triaxial state of stress is present, voids will grow and coalesce quickly since the voids will be more closely spaced. Consequently, failure will occur more rapidly than if the mean inclusion spacing is large.

There are other material properties which can also affect a material's response to void growth and coalescence. Strain rate sensitivity and work hardening capacity are both important properties. If a material has high strain sensitivity, as discussed in section 1.1, it will be able to counteract the local deformation of the deformation bands by hardening the material in the band subjected to the higher strain rate. In the same vein, when a volume in the material becomes locally weak due to void growth, the material will respond by hardening the remaining ligament in this locally soft area; the deformation will then localize in the next weakest area instead of concentrating in this particular area, as depicted in figure 44. If a material has high work hardening capacity, at high strains it will maintain the work hardening rate at a high enough value to delay the onset of local necking.

For 6111-T4 the inclusions and initial void population could account for the low elongation. Since this material has low strain rate sensitivity and low work hardening capacity, a high inclusion and initial void population would limit the elongation. As discussed earlier, these defects could set up a locally weak area where the deformation would concentrate. With the low strain rate sensitivity and low work hardening, the strain would continue to localize in a particular region. This strain concentration would cause a faster drop in the work hardening rate such that necking would occur sooner. The elongation, then, would be lower. At 300K and 10^{-4} /s, one-third of the tensile samples are able to attain higher elongation. The work hardening curves (figure 23f) show that the sample with higher elongation has more stable work hardening behavior near the necking point. The drop off near necking occurs more gradually and closer to the local necking criterion ($\theta = \frac{\sigma}{2}$). One possible explanation for this behavior is that the unstable samples have higher inclusion count and higher initial void population.

In thin sheets, the effects of a large inclusion population can have an even more significant impact, especially if there is a large variation in the inclusion distribution. If a tensile specimen samples an area with a much higher inclusion population, upon void growth and coalescence, the effective net cross sectional area will be reduced. With applied strain, deformation will concentrate more quickly in this sample, and the increased strain localization will lead to the earlier onset of local necking. The elongation will then be lower than that of a sample which had a smaller inclusion population.

Examination of the fractured sample at the fracture surface on the short transverse-transverse (S-T) plane and the longitudinal-transverse (L-T) plane (along the gage section) will aid in determining whether the inclusions and voids are limiting the elongation. In the S-T plane, if they are limiting the elongation, it would be expected that the fracture surfaces of the unstable samples would have a different appearance than that of the stable samples. If the mechanism leading to early failure is that of an initially smaller net cross sectional area due to the presence of a higher inclusion concentration, the fracture surfaces of the

unstable samples would contain more inclusions or more large inclusions than that of the stable samples. The same would also be expected if the mechanism leading to early failure is that of a more rapid void coalescence due to smaller mean inclusion separation. From figure 45, the fracture surfaces in the S-T plane, examined by SEM, are not significantly different.

In the L-T plane, tensile samples were polished before and after testing to view the void population along the gage length. The fractured samples were polished to one-half thickness to a finish of 0.05 μm. If voids were causing the early onset of necking in the unstable sample, then the L-T plane would have either a high void populations prior to testing, which would lead to early onset of necking, or a higher void population both at the fracture surface and away from the fracture surface. As schematically drawn in figure 46, a strain gradient exists in the L-T plane with the highest strain at the fracture surface and the lowest strain farthest away. It would be expected that the void population would be highest at the fracture surface and that the population would decrease with increasing distance from the fracture surface. From the optical microscopy, two observations can be made. First, at the fracture surface (figure 47), no obvious differences were seen in the void population between the stable and unstable samples. The fracture profile for the stable and unstable samples were similar; part of the surface was formed by void coalescence (figure 48a) and other parts were more planar (figure 48b). The etched surface reveals that the samples fractured along grain boundaries as well through grains (figure 49). At the arrow in figure 49, the specimen has fractured through three grains with similar grain contrast. Grains with similar orientation will have similar color contrast. Therefore, the specimen has fractured, following the fracture surface from left to right in the micrograph, through a cluster of similarly oriented grains, stopped at a void, and then proceeded along the grain boundaries of a cluster of similarly oriented grains.

Second, voids were seen away from the fracture surface and outside the necked region for both stable and unstable samples. Again, there were no significant differences.

Both samples had voids with an elongated appearance; the major axis of the void aligned with the tensile direction and rolling direction. Since the voids did not appear elongated in the untested sample, this elongation is due to the applied tensile load. Voids were also seen around fractured inclusions (figure 45a) in the tested samples. These fractured inclusions may be due to the applied tensile load or to the polishing. If they were due to polishing, then fractured inclusions would be visible in the grip section of the tensile sample. An optical micrograph taken from the grip section shows that polishing does not fracture the inclusions (figure 50). Since the void population is not significantly different between the stable and unstable samples, a difference in inclusion and void population is not causing the early failure in the unstable samples. Therefore, a high inclusion and void population, which would lead to void growth and coalescence, is not limiting the elongation in 6111-T4.

If the voids are not responsible for the early drop off in work hardening, then other possibilities must be considered. Two possible explanations for the early drop off are material properties, such as strain rate sensitivity, and inhomogeneous deformation. It is known that aluminum is not a very strain rate sensitive material. The strain rate sensitivity can change with temperature and strain rate. At the other, higher strain rates, where the samples consistently have earlier work hardening drop offs, the strain rate sensitivity may be low enough that once the material has reached a certain mechanical state, it cannot recover from a local instability, and it will proceed to final failure. At 10^{-4} /s, it is possible that the strain rate sensitivity is just high enough that in some cases, the material can maintain fairly stable deformation, despite the formation of islands or deformation bands, until the local necking criterion. The role of inhomogeneous deformation will be discussed below.

6.3 Deformation Behavior: 6111-T4, Longitudinal

The deformation behavior can be characterized by examining certain aspects of the work hardening behavior. One region of the work hardening, denoted as region A in figure 51, is of particular interest. Region A describes that part of the work hardening curve from the start of the last linear portion through failure. The work hardening curve can be fitted with a line based on the assumption that one mechanism dominates in the region through failure. This mechanism will heavily influence the deformation behavior and elongation. Several aspects of the work hardening curve can be used to assess how stable the deformation is near necking and how quickly diffuse and local necking occur. These aspects are the work hardening oscillations, the work hardening drop off near necking, the necking parameters and the width and thickness measurements. The oscillations are due to local stabilities and instabilities in the gage section. The work hardening drop off can indicate how stably deformation proceeds near necking. The necking parameters can qualitatively assess how quickly the material progresses from diffuse necking to local necking to failure. The width and thickness measurements will detail when diffuse and local necking occur. How these parameters are related and how each is affected by test condition, microstructure and specimen geometry will also be discussed.

6.3.1 Work Hardening Oscillations

Oscillations in the work hardening are present from yielding to failure. These oscillations are seen over many test conditions, microstructures, alloys and specimen geometries. As mentioned in section 5, these oscillations are due to local hardening, or stabilities, and local softening, or instabilities, in the gage section. Since these oscillations have been seen in all tensile tests, it can be argued that they are due to test machine or equipment noise, or that they are created during data processing. If they are real, it must be determined how they affect the elongation.

Because the oscillations occur despite changes in many test and microstructural variables and alloy systems (6061-T6, 6111-T4, 6111 SHT and AKDQ steel), it is possible to argue that the test machine or equipment noise can cause the oscillations. The oscillations have a wavelength of over 0.5 to 1.0% strain, which takes approximately 50 seconds per oscillation. Mechanical noise will occur at 0.02 seconds per cycle (60 Hz) and random electrical noise occurs in the MHz region. Load cell and strain extensometer noise will effect errors in the stress and strain, respectively, of ± 0.62 MPa and 0.00001 mm/mm. The amplitude of the oscillations is at least 4 MPa, and the wavelength, as mentioned above, is 0.005-.01 mm/mm strain. Clearly, equipment noise is not responsible for these oscillations.

It can also be argued that the oscillations are introduced during the data processing. Ideally, if the data processing is causing oscillations, then even processing a smooth curve will create oscillations. A smooth true stress-true strain curve can be generated by using the parabolic relationship

$$\sigma = K\varepsilon^n \tag{6.1}$$

where

$K = 1$

$n = 0.2$.

The stress-strain curve is shown in figure 52a, and after processing the data, the work hardening curve (figure 52b) is also smooth. No oscillations are present. Therefore, the data reduction process does not create oscillations.

6.3.1.1 Mechanism for Oscillations

It has been shown that the work hardening oscillations are present over many different test conditions. There are two mechanisms that can cause these oscillations: the PLC effect and the formation and propagation of deformation islands and bands. If these

oscillations are present outside of the PLC regime, for instance outside of its temperature range, then this oscillatory behavior is dominated by something other than the PLC effect. The other possible mechanism is the formation and propagation of islands.

6.3.1.1.1 The PLC Effect and Inhomogeneous Deformation

For aluminum alloys it is widely accepted that oscillations in the stress-strain curve and the appearance of deformation bands are due to the PLC effect [Cetlin, Gulec and Reed-Hill, 1973; Chihab, Estrin, Kubin and Vergnol, 1987; Fujita and Tabata, 1977; Kim and Chaturvedi, 1979; Reed-Hill and Gulec, 1975; Phillips and Swain, 1952-3; Robinson and Shaw, 1994; Rodriguez, 1984]. 6111-T4 does have some free solutes, and it is possible that these oscillations are due to the PLC effect. Another look at the stress-strain curve of 6061 [Robinson, 1994] in figure 5 shows that along with the serrations, there are also longer wavelength oscillations which occur over larger strain ranges. These oscillations occur simultaneously with the serrations and are schematically shown in figure 53. These long wavelength oscillations have not been addressed in the literature.

The PLC effect is not the dominant mechanism behind the oscillations in 6111-T4 for several reasons. First, the oscillations are still present at 77K (figure 24), which is well outside the PLC temperature regime. The solute mobility is too low to pin moving dislocations. A simple calculation of the diffusion rates of the major alloying elements at 77K can be performed. The diffusion coefficient, D, can be estimated from the equation

$$D = D_o \exp\left(-\frac{Q}{RT}\right) \tag{6.2}$$

where

D_o = pre-exponential constant, a material constant

Q = activation energy.

D_o is often measured at high temperatures, and its value will change with temperature. Since values were not available for 300K or 77K, the higher temperature values were used

in equation 6.2. Using the higher temperature D_o values would yield a conservative estimate of the diffusion coefficient. Values of D_o from several sources were used [Bishop and Fletcher, 1972], and based on these values, an average D was calculated. The diffusion coefficients for Mg, Cu and Si at 300K and 77K are listed in Table 10. When the temperature decreases from 300K to 77K, the diffusion coefficient decreases by approximately 60 orders of magnitude. Clearly, the solutes are not diffusing quickly enough to pin mobile dislocations at 77K. Second, oscillations are present in a non-PLC alloy AKDQ steel (figure 33). It is possible that the PLC effect does play a small role in the oscillation behavior, since 6111-T4 does have some free solute content. The character of the oscillations changes with the temperature and alloy change, but the basic behavior is still present when these variables are altered. If the PLC effect is not the dominant mechanism behind the oscillations, then the formation and propagation of islands and bands must be considered.

Table 10- Diffusion coefficients of major solutes in 6111-T4.

Element	T [K]	D [mm^2/s]
Cu	298	1.80e-23
	77	5.36e-84
Mg	298	7.63e-22
	77	9.16e-82
Si	298	3.21e-23
	77	1.20e-87

6.3.1.1.2 Effect of Microstructure and Islands on Oscillation Behavior

If the PLC effect is not responsible for these oscillations, then other mechanisms or microstructural features must be considered. This alloy does have some free solutes, GP

zones and islands. The first two features can be ruled out from the experimental results. The solution heat treatment and low temperature tests effectively alter the precipitate and solute structure. With the solution heat treatment, the GP zone population is significantly reduced while the solute content is greatly increased. Comparing the SHT and the -T4 work hardening curves in figure 31, the oscillations are still present. The amplitude and number of oscillations, however, have increased with the solution heat treatment. Conversely, the curves can also be viewed by assuming the SHT condition as the starting condition. Then, by naturally aging to -T4, the solute population is greatly decreased, and the GP zone population has increased. The number and amplitude of the oscillations has decreased, but the basic oscillation behavior is still present. The solutes and GP zones may still make minor contributions to the oscillation behavior, but they are not the dominating features. It is reasonable to expect that several microstructural features or mechanisms contribute to the deformation behavior with one dominates in a particular strain range.

From the experimental results a correlation had been established between the oscillations and the islands and deformation bands. Islands and deformation bands were seen on the specimen surfaces by in-situ and ex-situ observations (section 5.9). At 1% plastic strain (300K, 10^{-4} /s), islands were observed by optical microscopy (figure 34) and by in-situ visual observations; there was a corresponding rise in the work hardening rate. At 77K (10^{-4} /s) two sample wide deformation bands were observed, and there was a peak in the work hardening rate. From the elimination of the other mechanisms and microstructural features and the correlation observed between the islands/deformation bands and the oscillations, it is believed that the oscillation behavior is dominated by macroscopic inhomogeneous deformation: island and deformation band formation and propagation. Minor contributions to the oscillation behavior are made by solutes and GP zones.

6.3.1.2 Effect of Oscillations on Elongation

The presence of oscillations in the work hardening curve raises an important question: Do they affect the subsequent deformation behavior and elongation? The effect of these oscillations on the elongation can be measured from a work hardening plot. The elongation of a thin sheet in uniaxial tension is limited by the necking criterion: $\theta = \frac{d\sigma}{d\varepsilon} = \frac{\sigma}{2}$. On figure 54, it can be seen that the elongation is indicated by where the work hardening rate θ equals $\frac{\sigma}{2}$. The hypothetical loss of elongation can be obtained by determining the ideal and actual elongations for the sample. The ideal elongation is defined by assuming that the mechanism dominating in the latter part of the work hardening curve will continue to dominate. The peaks in the work hardening occur due to the initiation of deformation in the next weakest area in the specimen; therefore, the peaks represent what the ideal work hardening rate would have been if deformation were occurring homogeneously. A line can then be fitted to the oscillation peaks in the latter region of the work hardening curve, and the intersection of this line and the $\frac{\sigma}{2}$ curve will yield the ideal elongation. If the actual work hardening curve intersects the $\frac{\sigma}{2}$ curve before the ideal value, the local instabilities are causing a loss of elongation.

When this analysis is applied to 6111-T4 at 300K and 10^{-4} and 10^{-1} /s, a loss of elongation from the ideal case is seen. The ideal and actual elongations at each condition are plotted in figure 55a. At 10^{-4} /s the actual and ideal elongations are 23.4% and 31.4%, respectively, and at 10^{-1} /s, the actual and ideal elongations are 21.25% and 28.09%, respectively. The percentage loss of elongation, then, for each of these strain rate conditions is 17.22% (10^{-4} /s) and 24.35% (10^{-1} /s). Not only are these oscillations causing a loss of elongation, but the loss becomes more severe at the higher strain rate.

As a comparison, this analysis can be done on AKDQ steel. The actual and ideal elongations are shown in figure 55b, where in AKDQ steel, there is also a loss of elongation resulting from these oscillations. The percentage loss of elongation is about

13.15% at 10^{-4} /s, and 22.08% at 10^{-1} /s. These losses are not as large as those of 6111-T4.

The oscillations, or islands, do cause a loss of elongation, but the severity of the loss will depend on the alloy. Other factors such as work hardening rate and strain rate sensitivity can affect the influence of the islands. For aluminum alloys the loss of elongation is greater because it has low work hardening and little to no strain rate sensitivity. Steel alloys are better able to cope with the presence of islands because their strain rate sensitivities are higher, and they have higher work hardening.

6.3.2 Necking Behavior

Necking behavior can be assessed qualitatively, through the θ, $\frac{\sigma}{2}$ vs. ε plot, and quantitatively, through width and thickness measurements in the gage section both before and after straining. Qualitatively, if the work hardening drops off sharply prior to failure, an instability has occurred from which the sample cannot recover. If the drop off occurs earlier in the work hardening curve, then at this particular test condition and microstructure, the sample loses stability earlier as compared to other conditions or microstructures. There are some parameters that can be useful in indicating how well a material responds to instabilities induced by islands, deformation bands, or a diffuse or local neck. As mentioned above, for sheet specimens, the formation of a diffuse neck begins at maximum load. The amount of strain between the onset of diffuse necking and the onset of local necking, ε_{DL}, can indicate how stable the deformation is once a diffuse neck has formed. A small ε_{DL} value would imply that the once diffuse necking has occurred, the sample will deform in a very unstable manner and proceed to local necking very quickly. The parameter ε_{LF} can qualitatively assess the stability of deformation between local necking and failure. If this parameter is small, as would be expected in a non-strain rate sensitive material such as aluminum, then the material becomes very unstable with respect to the formation of a local neck and fails quickly. Quantitatively, the width and thickness

measurements characterize whether the diffuse and local necks occur at the theoretical predictions. From these measurements (section 5.10), diffuse and local necking can occur before the theoretical predictions at 300K and 10^{-4} /s; this topic will be discussed further in section 6.4.

6.3.3 Assessment of the Deformation Behavior

All of the work hardening and necking parameters mentioned above can be reduced to a few simple parameters that can be qualitatively compared. For the oscillations, the number of oscillations and their average amplitude in the final linear portion of the work hardening curve can be determined. As was assumed in determining the loss of elongation resulting from the oscillations, the mechanism that dominates in this latter portion is the one that will continue to dominate until failure. Therefore, this mechanism will dominate the deformation behavior and the elongation. Compare two conditions: one (A) produces a larger number of oscillations (N_A) and the other (B) produces a smaller number of oscillations (N_B) (figure 56a). A large number of oscillations would indicate that several islands or deformation bands have formed and propagated. Since the elongation does not vary significantly with a change in strain rate, it can be assumed that A and B are generally experiencing the same amount of global strain. The global strain is then distributed over more islands in sample A; thus, it would be expected that the average amplitude for A is smaller than that for sample B. The deformation, then, is more homogeneous in A, and the material will deform more stably. It would be expected that the sample will approach necking more gradually, that the work hardening drop off would occur at a later strain (figure 56b) and that the drop off would occur more gradually. The necking parameters (ε_{DL} and ε_{LF}) should be larger in A than in B, since the global strain is more homogeneously distributed in A.

6.3.3.1 Effect of test variables

As mentioned earlier, increasing the strain rate reduces the amount of time a specimen has to accommodate the deformation. Deformation processes with a time dependent component do not have enough time to activate. Therefore, the deformation must be accommodated on fewer slip planes, and with increasing applied strain, the deformation continues to concentrate on these planes. At the macroscopic deformation level, the applied strain would be distributed on fewer islands. With fewer islands, there are fewer oscillations in the work hardening curve. The consequence of fewer islands is that the work hardening would drop off earlier and more sharply due to larger strain concentrations in the fewer islands. The sharper drop off would result in the early onset of diffuse and local necking and failure, thus the necking parameters would be smaller than those at a lower strain rate.

In figure 57 the effect of increasing the strain rate from 10^{-4} /s to 10^{-1} /s at 300K, in the longitudinal direction, are examined. With the increase in strain rate, the number of oscillations does decrease as expected, and the amplitude increases. No mathematical correlation was found. It would be expected that the drop off will occur later at 10^{-4} /s, and that the drop off would be more gradual. From figure 23, the drop off at 10^{-4} /s does occur later, at diffuse necking, while the drop off at 10^{-1} /s occurs before the onset of diffuse necking. The drop off occurs rapidly at both conditions, but it is more severe at 10^{-1} /s. The necking parameters, ε_{DL} and ε_{LF}, then, would be expected to be larger than those at 10^{-1} /s. ε_{DL} is greater, but ε_{LF} is smaller. At 10^{-4} /s the material is able to deform more stably between diffuse and local necking, but once local necking begins, the deformation becomes less stable, and the sample fails more quickly.

Temperature will also affect the deformation behavior. When the temperature is lowered, the amount of thermal energy is reduced, and thermally activated deformation mechanisms will not occur or will not occur as readily. The global strain must be accommodated on a fewer number of islands. The effect on the deformation behavior will

be much like that when the strain rate is increased. Fewer islands would form, and therefore, fewer oscillations would be expected. These oscillations will have larger amplitudes, and the work hardening drop off should happen sooner and more sharply. The necking parameters would have a smaller value. The elongation will then be lower.

In 6111-T4, however, the elongation increases when the test temperature decreases from 300K to 77K. This effect has been seen in other aluminum alloys such as 2090-T81 [Chu, 1990; Glazer, 1989; Tseng, 1993]. As mentioned above, the deformation generally becomes less homogeneous with a decrease in test temperature, due to the lower thermal component, and this decrease in deformation homogeneity should result in lower elongation. The greater elongation seen here could be due to either more homogeneous deformation or another mechanism. At 77K, then, if the deformation is more homogeneously distributed, it is possible that the number of oscillations increases, the average amplitude decreases, the work hardening drop off becomes more gradual and occurs later, and ε_{DL} would be greater.

At a strain rate of 10^{-4} /s, the number of oscillations decreases, and the average amplitude is larger at 77K (figure 58). These results alone imply that the deformation is less homogeneous and that the work hardening drop off should be sharper and occur earlier. The necking parameters should have smaller values as well. From figure 25a, the drop off occurs just before diffuse necking and is equally sharp for both conditions. From the necking parameters, however, ε_{DL} is larger and ε_{LF} is smaller at 77K. The greater ε_{DL} value indicates that near diffuse necking, this material is able to deform more stably until local necking occurs. The greater elongation at 77K and 10^{-4} /s is not due to more homogeneous deformation.

At 10^{-1} /s (figure 59) the number of oscillations actually increases with a decrease in temperature, and the average amplitude is smaller. The drop off occurs at diffuse necking, and it is more gradual. These characteristics indicate that more islands form at 77K, and therefore, the drop off should occur later in the work hardening curve and should be more

gradual. The necking parameters and elongation should also be larger at 77K. In figure 59d, ε_{DL} is larger, but ε_{LF} is smaller. 6111-T4 can deform to larger strains between the onset of diffuse necking and local necking, but once local necking has occurred, failure occurs more quickly at 77K. At these test conditions more homogeneous deformation could account for the greater elongation.

6.3.3.2 Effect of Solute/Precipitate Structure

Microstructural features that could affect the deformation behavior in 6111-T4 are the solute/precipitate structure, clusters of large sized grains and clusters of similarly oriented grains. These features can affect the formation and propagation of the islands and bands, which then should be reflected in the work hardening curve oscillations. If they cause the deformation to concentrate to a high enough strain, they can cause the onset of necking. In this section the effect of solute/precipitate structure on the deformation behavior will be examined.

The increase in solute content, at the expense of GP zones, generally increases the elongation and decreases the yield and ultimate strengths. An increase in solute content, from a solution heat treatment, usually creates more homogeneous deformation. With more homogeneous deformation, the number of oscillations would increase and the average amplitude would decrease. Consequently, near necking, the work hardening drop off would be delayed to higher strains, and the drop off would be more gradual. After necking ε_{DL} and ε_{LF} would be larger.

At 10^{-4} /s (figure 60), increasing the solute content increases the number of oscillations and increases the average amplitude. The drop off occurs before diffuse necking, and it is much sharper. From these results, it would be expected that the necking parameters would be lower, as well. From figure 60d, they are smaller than those at -T4. Despite the unstable behavior from the drop off to failure, the higher solute content condition has better elongation.

At 10^{-1} /s, the SHT samples have greater elongations and still have about the same number of oscillations as the -T4 samples, but their average amplitude is higher (figure 61). When approaching necking, the drop off occurs earlier (before diffuse necking), but the drop off is more gradual. The necking parameters have smaller values. In this test condition, despite the indications of unstable deformation behavior, the solution heat treated samples have greater elongation.

The increase in elongation, then, could be due to the decrease in strength. From figure 62, which is a bar chart of the percent change in mechanical property at a given test condition, the strengths decrease and the elongations increase at both strain rates. The decrease in strength is greater at 10^{-1} /s. Correspondingly, there is an increase in elongation at the higher strain rate. This strength effect alone may be enough to offset the other indications that less stable deformation is occurring: the increase in oscillation amplitude, the sharper drop offs, and the smaller necking parameter values.

6.3.3.3 Effect of Specimen Geometry

Changing the specimen geometry could affect the deformation behavior if the microstructural feature dominating the deformation behavior is on a macroscopic scale, e.g. the clustering of similarly oriented grains or large sized grains. Consider two samples with the same gage length and thickness but with different widths, and assume that the microstructure is held constant (figure 63). The microstructure constitutes a larger area fraction of the gage section in the narrow sample versus the wide sample. The wide specimen samples more grains and clusters and thus contains a more random sampling of the microstructure. The deformation behavior is less dependent on any particular cluster of grains. The islands that form from the clusters in the gage section will produce a work hardening curve that is schematically depicted in figure 63a. When the gage area decreases, as when testing the narrow sample, fewer grains and clusters are sampled; the clusters are a larger area fraction of the gage section. When a strain is applied, the resulting macroscopic

deformation behavior will be more sensitive to any islands that are dominated by the clusters. The number of oscillations will not change as significantly as the amplitude of the oscillations (figure 63b). Since the islands that form and propagate are a larger area fraction of the gage, the oscillation amplitude will increase. In this case, the work hardening drop off behavior, the necking parameters and elongation will not necessarily depend on the oscillation number and amplitude. But, if the elongation of the sample is low, it would be expected that the work hardening drop off will occur earlier and more sharply and that the necking parameters will be smaller in value. When the gage width decreases, the work hardening behavior near necking will become more dependent on the area sampled.

The standard samples were compared with wider (~45% larger) and narrower (~45% narrower) samples at 10^{-4} /s and 300K. In figure 64, increasing or decreasing the width from the standard dimension produces a slight decrease in yield strength and a decrease in the elongations. It would generally be expected that a decrease in yield strength would cause an increase in elongation. Clearly the decrease in elongation in each case cannot be explained by changes in the yield strength.

The lower elongations in the narrow and wide samples should be reflected in their deformation behaviors. Since the narrow samples have the lowest elongation, their work hardening drop offs should be sharpest and occur earliest, and their necking parameters should be smallest in value. From figure 65, when decreasing the gage width, the number of oscillations does not change, the amplitude increases, the work hardening drop off occurs earlier and more sharply, and the strain parameter ε_{DL} increases. After the onset of diffuse necking, the deformation is more stable as ε_{DL} increases with decreasing gage width. When local necking commences, the necking parameter ε_{LF} should behave similarly; from figure 65d, however, ε_{LF} actually peaks at the standard condition with the wide samples having the smallest value. After the formation of a local neck, deformation proceeds most stably in the standard sample. According to these trends, the elongation

should increase with gage width. As previously mentioned, the elongation is highest for the standard sample. It is possible that, when considering the scatter in the data, the elongation for the wide samples is on the low end. Thus, the average elongation for the wide samples may actually be higher.

Specimen geometry does noticeably affect the oscillation behavior. When the gage width decreases, it would be expected that the number of oscillations changes slightly and that the oscillation amplitude increases. From figure 65, the number of oscillations does not change, but the amplitude increases.

These results indicate that a more macroscopic feature is affecting the deformation behavior, since the properties and deformation behavior change with specimen geometry. The results from the SHT samples, EBSP microscopy and the optical microscopy point to clusters of similarly oriented grains and/or clusters of large sized grains affecting the deformation behavior in the latter part of the work hardening curve. The dissolving of precipitates and corresponding increase in solute content does increase the elongation of 6111. The explanation for this increase is due to the decrease in strength. The EBSP microscopy results have shown that there are clusters of similarly oriented grains (figures 12 and section 3.2) that are roughly one-tenth of the gage width. The optical microscopy results reveal clustering of large sized grains that usually consist of 4 or 5 grains. These two microstructural features are on a macroscopic scale, and therefore could affect the deformation behavior if the specimen geometry were altered.

6.3.4 Necking Measurements

Measurements of the gage width and thickness before and after tensile testing (300K, 10^{-4} /s) show that diffuse and local necking will begin prior to the theoretical criteria ($\theta = \sigma$ and $\theta = \frac{\sigma}{2}$, respectively) are satisfied. The formation of these necks prior to the theoretical criteria may cause the rather precipitous drop in work hardening rate near the theoretical diffuse necking criterion and the low elongations in 6111-T4. What is clear

from the data is that diffuse and local necking can occur before the theoretical predictions. The theoretical predictions are based on a continuum model. Formation of several necks prior to ultimate load have been theorized by Ghosh [Ghosh, 1974] and have been observed experimentally in a round cross-section stainless steel alloy 304L [Chan, 1999]. The low work hardening and the low strain rate sensitivity can accelerate the necking to failure process. One question that still remains is what microstructural feature could lead to the formation of the diffuse and local necks and thus the early, sharp drop in work hardening. There are a two possibilities: clustering of similarly oriented grains and clustering of similar sized grains.

Theory predicts that in sheet specimens tested in uniaxial tension, the onset of diffuse necking serves merely to reduce the gage section from an infinite radius to a finite radius. After further deformation, the onset of local necking will occur. This local necking is what will cause unstable deformation which will then lead, ultimately to failure. A sharp drop off, seen in 6111-T4, is indicative that the deformation is very unstable and that the onset of diffuse necking alone could cause final failure.

6.4 Island Formation and Propagation: Dominant Microstructural Feature

The feature that is influencing the formation and propagation of the islands is the clustering of similarly oriented grains or the clustering of large sized grains or both. Other microstructural features such as the PLC effect and the solute/precipitate structure have been eliminated in the previous section. For clustering of large sized grains that are surrounded by clusters of small grains, shown in figure 4a, can act as a soft area in the sample. In the cluster of large grains, there are fewer grain boundaries to encounter. If the area is locally weak, deformation can begin in a large grain, and then, with an applied stress, the resulting local stress will propagate the deformation in the direction shown (figure 4b).

If instead it is the cluster of similarly oriented grains that are dominating the oscillation behavior through the islands, then the islands could form and propagate in the following manner. In figure 4b, a cluster of grains with similar orientation (shaded) is surrounded by grains of different orientation or other clusters of similarly oriented grains. With the application of the tensile load, a locally weak area will begin deforming. The cluster with the most favorable orientation will begin deforming first within a particular grain or a group of grains. With further applied stress, the local stress distribution will drive the propagation of the deformation in the direction shown. This cluster of grains serves, essentially, as a single crystal. Deformation will be much easier to propagate through a cluster of grains with similar orientation rather than through neighboring grains of different orientation.

Particular textures can orient grains such that deformation occurs more easily. Although the material is polycrystalline, an ideal Schmid factor can be calculated for each grain to predict which orientation will yield first. The grain can be treated as a single crystal. Using the equation

$$\tau = \sigma \cos\alpha \cos\beta \tag{6.3}$$

where

τ = resolved shear stress

σ = applied tensile stress

α = angle between the tensile axis and the slip direction

β = angle between the tensile axis and the slip plane normal, and

$\cos\alpha\cos\beta$ = Schmid factor.

In addition, the critical resolved shear stress (CRSS) must also be considered in predicting the orientation most likely to slip first. The crystal with the combination of a high Schmid factor and a low CRSS will likely slip first. The CRSS for pure aluminum single crystals

ranges between 0.54-0.98 MPa [Honeycombe, 1984]. The Schmid factors for the common textures found in 6111-T4 are listed in Table 11. It is assumed that the rolling direction is aligned with the tensile axis.

According to Schmid factor calculations in Table 11, the S texture has the highest factor while the Cube texture has the lowest. Based on this data alone, the grains with the S orientation should yield first. The population of grains with the S texture cannot account for all the islands observed, however. The Cube texture is the predominating texture, and it is possible that grains with this orientation have a much lower CRSS. Therefore, it is possible that grains with the Cube orientation will yield first.

As was mentioned in section 3.2, EBSP microscopy reveals that there is clustering of grains with the S and Cube orientations (figures 12a and 12h, respectively). The distributions of these clusters also has directionality at an angle from the tensile axis/rolling direction, and this directionality is similar to the angle with which the islands lie in the gage section.

Table 11- Schmid factors for 6111-T4 textures.

Orientation	Miller Indices	Schmid Factor
Cube	{100}<001>	.4082
Goss	{110}<001>	.5774
R	{124}<211>	.7638
P	{011}<122>	.7698
Q	{013}<231>	.6901
Copper	{112}<111>	.7698
Brass	{011}<211>	.7071
S	{123}<634>	.8382

It is also possible that both clusters of large sized grains and clusters of similarly oriented grains could cause the islands and bands. In the locally weak area, where the deformation will begin, it maybe easier to begin and propagate deformation with one mechanism over the other. For instance, there may be a cluster of large sized grains that will be the easiest path of deformation. On the other hand, if the locally weak area does not have a cluster of large sized grains, but, instead, has a cluster of similarly oriented grains, then the deformation would preferentially propagate through this cluster. Another possible scenario is that the deformation can form with one cluster type, and then propagate through another type, or vice versa.

The ex-situ optical observations, detailed in section 5.9, reveal that there is clustering of similarly oriented grains. Further, these clusters can affect the deformation behavior. In figure 35, slip is more intense in one cluster than in the surrounding grains. Along the fracture surface, the crack will propagate along the grain boundaries of similarly oriented grains, then change direction when it encounters a void or different group of grains (figure 49).

Although the local texture variation and grain size distribution may be the dominant mechanisms behind the oscillations, the other microstructural features that were previously ruled out may still play a minor role in the oscillations. Lowering the test temperature does eliminate the PLC effect, but the oscillation character does change. With solution heat treatment, or conversely, with natural aging, the solute/precipitate structure changes the character as well. As mentioned above, the overall oscillation behavior is still present despite these changes in microstructure and temperature. The PLC effect and solute/precipitate structure are not trivial, but they do not dominate the oscillation behavior. This finding is reasonable since it would not necessarily be expected that one particular mechanism will completely control the deformation behavior, especially in a structural alloy.

These results can also help to explain why two-thirds of the tensile samples at 300K, 10^{-4} /s have low elongation and unstable work hardening behavior near the theoretical diffuse necking criterion. The two possible explanations were high inclusion and initial void population and island formation and propagation. The high inclusion and initial void populations were already ruled out in section 6.2.1. Such macroscopic features as clustering of similarly oriented grains and large sized grains are a significant area fraction of the gage area, even in a standard sized sample. At the particular test conditions of 300K and 10^{-4} /s, the effect of such features may be even more pronounced. Width and thickness measurements at these test conditions have also shown that diffuse and local necking can occur before the theoretical prediction of diffuse and local necking. If the specimen is sampling different types of clusters, then the work hardening drop off and elongation will ultimately depend on how well the clusters resist localized deformation. In two-thirds of the cases, the area sampled leads to unstable deformation behavior, the early onset of diffuse and local necking, and low elongation.

6.5 Model for Island Formation and Propagation

It is hypothesized here that the formation and propagation of the islands is a result of the superposition of the global stress distribution and the stress concentration at the deformation front. Stress concentrations arise in the matrix due to discontinuities in strain from adjacent regions; it is analogous to the concept of the Eshelby cycle. The shape change from the plastically deformed region in the undeformed body produces local stresses which act on the surrounding material. These two factors combine to produce a local stress distribution that would affect the formation and propagation of the macroscopic scale islands in the following manner, as shown in figure 66. During a tensile test, deformation first occurs in a locally weak area that is usually due to a geometric imperfection. In this area, a few grains begin to deform; this softening is reflected as a decrease in the slope of the stress-strain curve (figure 66a). These grains are part of a

cluster of either similarly oriented grains or large sized grains; they are favorably oriented to begin yielding first. The deformation of this area raises the local stress on neighboring grains, thus inducing them to deform as well. As this island continues to increase in size the slope in the stress-strain curve continues to decrease, which reflects the continued softening (figure 66b). When the deformation area encounters a sufficiently "hard" area, such as a cluster of differently oriented grains or a cluster of smaller sized grains, it stops increasing in size. Now, the local stress is not large enough to overcome obstacles in the surrounding, harder microstructure, thus the deformed area can no longer increase in size. The slope in the stress-strain curve no longer decreases (figure 66c). With further deformation, the area will harden, thus the slope of the stress-strain increases. When the area hardens to the point where it is more favorable to begin deformation in the next weakest area in the specimen, the slope of the stress-strain curve stops increasing (figure 66d). Further applied stress will initiate a new island in the next weakest area, and the slope in the stress-strain curve decreases due to the local softening. This process will continue until a large enough island or a group of islands will locally soften the sample such that a deformation band, which spans the width of the sample, will form. Several bands may form, as was seen on the 4.2K sample (figure 36), but the one that is weakest will preferentially deform. When this band causes a decrease in the work hardening rate from which the sample cannot recover, the local neck will begin forming in this band. The formation of the local neck can occur prior to the theoretical local necking criterion ($\theta = \frac{\sigma}{2}$), as was found with the width and thickness gage measurements (section 6.3.2). Finally, failure will occur.

7 SUMMARY & CONCLUSIONS

The deformation behavior of 6111-T4 was investigated to determine the cause of low tensile elongation. Tensile tests were conducted at selected temperatures, strain rates, and microstructures, and with different alloy systems to assess the roles of test parameters, microstructure and specimen geometry. The work hardening behavior was examined both qualitatively and quantitatively. Optical microscopy and SEM were utilized to quantify the microstructure and to characterize the deformation behavior. Both in-situ and ex-situ observations were made on the tensile samples to characterize the surface deformation behavior.

In 6111-T4 oscillations in the work hardening occurred and they are not due to the Portevin-LeChatelier (PLC) effect. These long wavelength oscillations do appear in the stress-strain curves in the literature, but their significance has not been noted. The oscillations here are found to produce a loss of elongation from the ideal hardening case. Ex-situ observations and low temperature tensile tests have shown that macroscopic scale deformation islands and bands are correlated with these oscillations. When an oscillation occurs, deformation bands and islands were observed on the specimen surface. The islands have been observed on samples at strains as small as 1%.

The formation and propagation of the islands and deformation bands are due to the clustering of similarly oriented grains and/or similar sized grains. Optical and EBSP microscopy have shown that clusters of large sized grains and clusters of similarly oriented grains occur in this alloy. The clusters of similarly oriented grains are aligned at an angle with respect to the tensile axis that is same as the alignment of the deformation bands and islands. Other microstructural variables such as solute/precipitate structure have been eliminated because the oscillations are still occur despite a solution heat treatment and quench.

Near diffuse necking, the work hardening dropped off dramatically in 6111-T4. In addition, two-thirds of the tensile samples tested at 300K and 10^{-4} /s had sharp drops in

work hardening around the diffuse necking criterion; one-third of these samples were able to maintain more stable deformation, and the drop off occurred just before the local necking criterion. Since the initial inclusion population was high in this alloy, the early drop in work hardening could be due to a higher initial inclusion and void count. A higher initial inclusion and void count could set up locally weak areas where the deformation could concentrate. The strain concentration would cause a faster drop in work hardening rate, and when the local strain reached a critical value, it would lead to the early onset of necking. From optical microscopy and SEM observations, the inclusion and void populations, which were difficult to quantify, were approximately the same for both stable and unstable tensile samples. For both sample types, there was not a significant void population near the fracture surface. The early drop in work hardening is thus due to the heterogeneous microstructure, clustering of similarly oriented grains and clustering of large sized grains, and not to the differences in their inclusion populations.

Since the deformation behavior near necking was of interest, measurements of the gage width and thickness were taken before and after straining. Both diffuse and local necks form prior to their respective theoretical predictions. These theoretical predictions are based on continuum behavior. The present results indicate that the local behavior can be very different from the macroscopic work hardening behavior. Contrary to continuum model predictions, the specimen can form a local neck while the macroscopic work hardening rate remains greater than the true stress or the one-half true stress value. As local necking continues to progress, it can cause the macroscopic work hardening to drop sharply. Therefore, the inhomogeneous microstructure and the local deformation behavior play a significant role in the macroscopic deformation behavior.

From these results the following conclusions can be made. First, the work hardening oscillations are due to the formation and propagation of deformation islands and deformation bands. Second, the microstructural features dominating the formation and propagation of the islands and deformation bands are the clustering of similarly oriented

grains and the clustering of large sized grains. Third, the sharp drop in work hardening near the diffuse necking criterion for 300K, 10^{-4} /s test samples is due to the inhomogeneous deformation arising from these clusters. The clusters act as locally soft areas in the sample that can concentrate the strain. When the local strain reaches a critical value, a local neck will form, and then a sharp drop in the work hardening can result. Fourth, diffuse and local necks form prior to their respective continuum theoretical criteria.

Since inhomogeneous deformation is lowering the elongation, and the clustering of similarly oriented grains and large sized grains is the primary cause behind the inhomogeneous deformation, then the elongation of 6111-T4 can be improved by eliminating the clustering of the grains. Elimination of this clustering can be accomplished by altering the processing. For instance, more cross rolling can help to eliminate the clustering of similarly oriented grains and produce a more random local texture distribution in the sheet. Other researchers [Bryant, Beaudoin, and Demeri, 1996] have also suggested that altering the processing can help to improve the formability.

8 OUTSTANDING ISSUES AND SUGGESTED FUTURE WORK

There are some issues that still need resolution. A direct correlation between the work hardening oscillations and localized deformation can be conducted by performing real-time analysis of the stress-strain behavior in conjunction with in-situ observations of the deformation behavior and/or strain localizations. A more statistically significant sampling of the narrow gage section tensile specimen should be performed. Finally, since for this work only one grain orientation and grain size distribution was available, it would be useful to conduct this work on samples with different grain orientation and grain size distributions.

REFERENCES

Adams, B. L., S. I. Wright and K. Kunze, "Orientation Imaging: The Emergence of a New Microscopy", *Met. Trans. A*, v. 24A, no. 4, 1993, p. 819-831.

Anderson, T. L., **Fracture Mechanics**, CRC Press, Inc., 1995.

Bishop, M and K. E. Fletcher, "Diffusion in Aluminium," *Int. Met. Rev.*, v. 17, September, 1972, p. 203-25.

Bryant, J.D., A. J. Beaudoin, and M. Demeri, "Effect of Crystallographic Texture on Formability in AA6111 Autobody Sheet", **Aluminum and Magnesium For Automotive Applications**, eds. J. D. Bryant and D. R. White, The Minerals, Metals & Materials Society, 1996, p. 85-95.

Bull, M. J., G. B. Burger, A. K. Gupta, P. W. Jeffrew and D. J. Lloyd, "The Microstructural Properties of Aluminum Sheet Alloys Used for Automotive Structure and Body Applications," Alumatec '94.

Bunge, H. J., "General Outline and Series Expansion Method," **Quantitative Texture Analysis**, eds. H.J. Bunge and C. Esling, 1982, p. 1-72.

Cetlin, P. R., A. S. Gülec and R. E. Reed-Hill, *Met. Trans.*, v. 4, 1973, 513.

Chan, J. W., private communication, 1999.

Chihab, K., Y. Estrin, L. P. Kubin and J. Vergnol, *Scr. Met.*, v. 21, 1987, 203.

Chu, D., *Cryogenic Mechanical Behavior of Vintage III Aluminum-Copper-Lithium Alloy 2090-T81*, M.S. Thesis, December 1990.

Dingley, D. J., "Diffraction From Sub-Micron Areas Using Electron Backscattering in a Scanning Electron Microscope", *Scanning Electron Microscopy*, v. 2, 1984, p. 569-575.

Dingley, D. J. and K. Baba-Kishi, "Electron Backscatter Diffraction in the Scanning Electron Microscope", *Microscopy and Analysis*, May, 1990.

Edington, J. W., **Electron Diffraction in the Electron Microscope**, v. 2, Macmillan, London, 1975.

Engler, O., "Nucleation and Growth During Recrystallisation of Aluminium Alloys Investigated by Local Texture Analysis," *Mat. Sci. Engr.*, October, 1996, v. 12, p. 859-872.

Fujita, H. and T. Tabata, *Acta Met.*, v. 25, 1977, 793.

Ghosh, A. K., *Met. Trans.*, v. 5, 1974, 1607.

Gillis, P. P. and S. E. Jones, *Int. J. Mech. Sci.*, v. 21, 1979, 109.

Glazer, J., *The Strength-Toughness Combination of the Aluminum-Lithium Alloys 2090 and 2091 at Cryogenic Temperatures*, Ph.D. Thesis, July 1989.

Honeycombe, R. W. K., **The Plastic Deformation of Metals**, Edward Arnold Publishers, Maryland, 1984, p. 12.

Jalinier, J. M., N. Christodoulou, B. Baudelet and J. J. Jonas, **Formability: Analysis, Modeling, and Experimentation**, 29.

Kim, I. S. and M. C. Chaturvedi, *Mat. Sci. Engr.*, v. 37, 1979, 165.

Krenn, C. R., *The Crystallography of Fatigue Crack Initiation in Incoloy-908 and A-286 Steel*, M. S. Thesis, December 1996.

McClintock, F. A., "Plasticity Aspects of Fracture," Fracture: An Advanced Treatise, ed. H. Liebowitz, volume III, Academic Press, New York, 1971, p. 48-225.

Michael, J. R. and R. P. Goehner, "Crystallographic Phase Identification in the Scanning Electron Microscope: Backscattered Electron Kikuchi Patterns Imaged with a CCD-Based Detector", *MSA Bulletin*, v. 23, no. 2, 1993, p. 168-175.

Phillips, V. A. and A. J. Swain, *J. Inst. Met.*, v. 81, 1952-3, 625.

Portevin, A. and F. Le Chatelier, *CR Acad. Sci.*, v. 176, 1923, 507.

Portevin, A. and F. Le Chatelier, *Trans. Am. Soc. Steel Treat.*, v. 530, 1924, 457.

Ramage, R. M., J. D. Bryant, and A. J. Beaudoin, **Automotive Alloys II**, ed. S. K. Das, The Minerals, Metals and Materials Society, 1998, p. 19-26.

Randle, V., **Microtexture Determination and Its Applications**, Institute of Metals, London, 1992.

Reed-Hill, R. E. and A. S. Gülec, *Met. Trans. A*, v. 6A, 1975, p. 461.

Robinson, J. M., *Int. Mat. Rev.*, v. 39, no. 6, 1994, p. 217.

Robinson, J. M. and M. P. Shaw, *Mat. Sci. Engr.*, v. A174, 1994, p. 1.

Robinson, J. M. and M. P. Shaw, *Int. Mat . Rev.*, v. 39, no. 3, 1994, p. 113.

Rodriguez, P., *Bull. Mater. Sci.*, v. 6, no. 4, 1984, p. 653.

Thomas, G, **Transmission Electron Microscopy of Metals**, Wiley, New York, 1962.

Tong, W., "Strain Characterization of Propagative Deformation Bands," *J. Mech. and Phys. Sol.*, v. 46, no. 10, October 1998, p. 2087-102.

Tseng, C., *Work Hardening Behavior in Aluminum Alloy 2090*, M.S. Thesis, December 1993.

APPENDIX A

```
'Based on program originally written by Tom Mason.  This program was modified by C.
R.
'Krenn and has been further modified to calculate misorientation angles for 6111-T4.
Option Explicit
'
'  Public txtRefPsi1 As Single
'  Public txtRefPhi As Single
'  Public txtRefPsi2 As Single
'
'
'
'Public Sub calc()
'Declaring variables from reference orientation
'Dim RefPsi1 As Single
'Dim RefPhi As Single
'Dim RefPsi2 As Single
'Dim Angle As Single
'declaring variables from cubic symmetry file
'Dim CubicSymmIndex As Single     'the symmetry matrix no.
'declaring variables from Matrix operations
'Dim Diagonal1 As Single          'Diagonal of matrix AnotherTransformMatrix
'Dim Diagonal2 As Single          'Diagonal of matrix Another TransformMatrix
'Dim Diagonal3 As Single          'Diagonal of matrix AnotherTransformMatrix
'Dim DetAnotherTransformMatrix As Single  'Determinant of AnotherTransformMatrix
'Dim TraceAnotherTransformMatrix As Single        'trace of AnotherTransformMatrix
```

```
☐'declaring variables for minimum angle
☐Dim Theta As Single            'Theta is the misorientation angle between reference orientation and
                                'grain orientation
☐Dim MinTheta As Single         'Minimum theta for
☐Dim arg As Double              'argument for ArcTan
☐'Declaring indices
☐Dim i As Integer               'i is index number
☐Dim a As Integer               'a is index number for 24 cubic symmetry matrices
☐Dim b As Integer               'b is index number of inputting matrix elements into
                                'SymmMatrix(a,b,c)
☐Dim c As Integer               'c is index number of inputting matrix elements into SymmMatrix(a,b,c)
☐Dim d As Integer               'd is index number for matrix TP(d,e)
☐Dim e As Integer               'e is index number for matrix TP(d,e)
☐Dim index As Integer           'index for matrix operation involving the reference matrix elements
                                'and the symmetric matrices
☐Dim g As Integer               'g is index number for TransformRefMatrix(g,m)
☐Dim m As Integer               'm is index number for TransformRefMatrix(g,m)
☐Dim n As Integer               'n is index number for SymmMatrix(index,g,n) during operation with
                                'the reference matrix
☐Dim index2 As Integer          'index2 for matrix operation involving the data matrix and the cubic
                                'symmetry matrices
```

```
Dim index3 As Integer          'index3 for counting from 0 to number of data rows in
original data
                                'file
Dim p As Integer          'p is index for TransformDataMatrix(p,r)
Dim r As Integer          'r is index for TransformDataMatrix(p,r)
Dim t As Integer          't is index for DataMatrix(t,r)
Dim w As Integer          'w is index for AnotherTransformMatrix(w,x)
Dim x As Integer          'x is index for AnotherTransformMatrix(w,x)
Dim y As Integer          'y is index for TransformDataMatrix(x,y)
Dim q As Integer          'q is index for TP(q,s)
Dim s As Integer          's is index for TP(q,s)
Dim z As Integer          'z is index for saving data to files
Dim pi As Single          'pi is the value of pi
Dim saveindex As Integer      'saveindex is index for saving the min angle to file

'Dimensioning arrays from data file
Dim xpos(10000)
Dim ypos(10000)
Dim posno(10000)
Dim Psi1(10000)
Dim Phi(10000)
Dim Psi2(10000)
Dim Column7(10000)
Dim DataMatrix(3, 3)      'orientation matrix from data file, 3x3
'Dimensioning arrays from reference orientation
Dim ref(3, 3)         'reference orientation matrix, 3x3 matrix
'Dimensioning arrays from cubic symmetry file
```

```
Dim SymmMatrix(24, 3, 3)
'Dimensioning array for minimum theta calculation
Dim TP(3, 3)
'Dimensioning arrays for matrix operations
Dim TransformRefMatrix(3, 3)
Dim TransformDataMatrix(3, 3)
Dim AnotherTransformMatrix(3, 3)

Dim saveFileName As String

'calling over the variables from the startup form
saveFileName = frmEbspStart.TxtFilename.Text
Angle = frmEbspStart.TxtAngle.Text
RefPsi1 = frmEbspStart.txtRefPsi1.Text
RefPhi = frmEbspStart.txtRefPhi.Text
RefPsi2 = frmEbspStart.txtRefPsi2.Text

'open files for input and for saving
Open "c:/Personal/Carol/Ebsp/Test.txt" For Input As #1
Open "c:/Personal/Carol/Ebsp/cubsym.txt" For Input As #2
Open "c:/Personal/Carol/Ebsp/" + saveFileName For Append As #3

i = 0                'zero index number for inputting data file
pi = 3.141592654

'calculate the direction cosines for reference 3x3 orientation matrix
```

```
        ref(1, 1) = Cos(RefPsi1 * pi / 180) * Cos(RefPsi2 * pi / 180) - Sin(RefPsi1 * pi /
                180) * Sin(RefPsi2 * pi / 180) * Cos(RefPhi * pi / 180)
        ref(1, 2) = -Cos(RefPsi1 * pi / 180) * Sin(RefPsi2 * pi / 180) - Sin(RefPsi1 * pi /
                180) * Cos(RefPsi2 * pi / 180) * Cos(RefPhi * pi / 180)
        ref(1, 3) = Sin(RefPsi1 * pi / 180) * Sin(RefPhi * pi / 180)
        ref(2, 1) = Sin(RefPsi1 * pi / 180) * Cos(RefPsi2 * pi / 180) + Cos(RefPsi1 * pi /
                180) * Sin(RefPsi2 * pi / 180) * Cos(RefPhi * pi / 180)
        ref(2, 2) = -Sin(RefPsi1 * pi / 180) * Sin(RefPsi2 * pi / 180) + Cos(RefPsi1 * pi /
                180) * Cos(RefPsi2 * pi / 180) * Cos(RefPhi * pi / 180)
        ref(2, 3) = -Cos(RefPsi1 * pi / 180) * Sin(RefPhi * pi / 180)
        ref(3, 1) = Sin(RefPsi2 * pi / 180) * Sin(RefPhi * pi / 180)
        ref(3, 2) = Cos(RefPsi2 * pi / 180) * Sin(RefPhi * pi / 180)
        ref(3, 3) = Cos(RefPhi * pi / 180)

'Input data file

Do While Not EOF(1)
   Input #1, posno(i), xpos(i), ypos(i), Psi1(i), Phi(i), Psi2(i), Column7(i)
   i = i + 1
Loop

'Input cubic symmetry file
For a = 1 To 24
   Input #2, CubicSymmIndex
   For b = 1 To 3
      For c = 1 To 3
         Input #2, SymmMatrix(a, b, c)
```

```
    Next c
  Next b
Next a

'Initialize matrix TP

For d = 1 To 3
  For e = 1 To 3
    TP(d, e) = 0#
  Next e
Next d


'  Transform Data Matrix wrto 24 matrices

For index3 = 0 To i
  If Column7(index3) < 0 Then
    GoTo 10
  End If

      DataMatrix(1, 1) = Cos(Psi1(index3) * pi / 180) * Cos(Psi2(index3) * pi / 180) -
                         Sin(Psi1(index3) * pi / 180) * Sin(Psi2(index3) * pi / 180) *
                         Cos(Phi(index3) * pi / 180)
      DataMatrix(1, 2) = -Cos(Psi1(index3) * pi / 180) * Sin(Psi2(index3) * pi / 180) -
                         Sin(Psi1(index3) * pi / 180) * Cos(Psi2(index3) * pi / 180) *
                         Cos(Phi(index3) * pi / 180)
      DataMatrix(1, 3) = Sin(Psi1(index3) * pi / 180) * Sin(Phi(index3) * pi / 180)
```

```
DataMatrix(2, 1) = Sin(Psi1(index3) * pi / 180) * Cos(Psi2(index3) * pi / 180) +
                   Cos(Psi1(index3) * pi / 180) * Sin(Psi2(index3) * pi / 180) *
                   Cos(Phi(index3) * pi / 180)
DataMatrix(2, 2) = -Sin(Psi1(index3) * pi / 180) * Sin(Psi2(index3) * pi / 180) +
                   Cos(Psi1(index3) * pi / 180) * Cos(Psi2(index3) * pi / 180) *
                   Cos(Phi(index3) * pi / 180)
DataMatrix(2, 3) = -Cos(Psi1(index3) * pi / 180) * Sin(Phi(index3) * pi / 180)
DataMatrix(3, 1) = Sin(Psi2(index3) * pi / 180) * Sin(Phi(index3) * pi / 180)
DataMatrix(3, 2) = Cos(Psi2(index3) * pi / 180) * Sin(Phi(index3) * pi / 180)
DataMatrix(3, 3) = Cos(Phi(index3) * pi / 180)

'Find minimum theta with respect to grain orientation by comparing to all 24 symmetries

MinTheta = pi / 2      'set minimum angle at pi/2

' Transform RefMatrix wrto 24 symmetric matrices

For index = 1 To 24
  For g = 1 To 3
    For m = 1 To 3
        TransformRefMatrix(g, m) = 0#      'initialize Transformed Reference Matrix
      For n = 1 To 3
        TransformRefMatrix(g, m) = TransformRefMatrix(g, m) +
                   SymmMatrix(index, g, n) * ref(n, m)
      Next n
    Next m
  Next g
```

```
For index2 = 1 To 24
  For p = 1 To 3
    For r = 1 To 3
      TransformDataMatrix(p, r) = 0#
      For t = 1 To 3
       TransformDataMatrix(p,    r)    =    TransformDataMatrix(p,    r)    +
                    SymmMatrix(index2, p, t) * DataMatrix(t, r)
      Next t
    Next r
  Next p

  'More Matrix operations
  For w = 1 To 3
    For x = 1 To 3
      AnotherTransformMatrix(w, x) = 0#
      For y = 1 To 3
       AnotherTransformMatrix(w,   x)   =   AnotherTransformMatrix(w,   x)   +
                    TransformRefMatrix(w, y) * TransformDataMatrix(x, y)
      Next y
    Next x
  Next w

  'Find diagonal of AnotherTransformMatrix
      Diagonal1 = AnotherTransformMatrix(1, 1) * (AnotherTransformMatrix(2, 2)
                    * AnotherTransformMatrix(3, 3) - AnotherTransformMatrix(3,
                    2) * AnotherTransformMatrix(2, 3))
```

```
Diagonal2 = -AnotherTransformMatrix(1, 2) * (AnotherTransformMatrix(2,
            1) * AnotherTransformMatrix(3, 3) -
            AnotherTransformMatrix(3, 1) * AnotherTransformMatrix(2,
            3))
Diagonal3 = AnotherTransformMatrix(1, 3) * (AnotherTransformMatrix(2, 1)
            * AnotherTransformMatrix(3, 2) - AnotherTransformMatrix(3,
            1) * AnotherTransformMatrix(2, 2))

'Find determinant
DetAnotherTransformMatrix = Diagonal1 + Diagonal2 + Diagonal3

'Find Trace
TraceAnotherTransformMatrix = AnotherTransformMatrix(1,1) +
            AnotherTransformMatrix(2,2) + AnotherTransformMatrix(3, 3)

'Find minimum angle by comparing to previous operation with cubic symmetry
matrix
If DetAnotherTransformMatrix < 0# Then
  TraceAnotherTransformMatrix = -TraceAnotherTransformMatrix
End If
arg = (TraceAnotherTransformMatrix - 1#) / 2#

'arg can't be 1 for this approximation of acos
If Abs(arg) = 1 Then
  arg = Sgn(arg) * (Abs(arg) - 0.0000000001)
End If
```

```
        Theta = Atn(-arg / Sqr(-arg * arg + 1)) + 2 * Atn(1)
        If Theta < MinTheta Then
          MinTheta = Theta
        End If
          For q = 1 To 3
            For s = 1 To 3
              TP(q, s) = AnotherTransformMatrix(q, s)
            Next s
          Next q

      Next index2
    Next index
10    If Column7(saveindex) < 0 Then
        Write #3, posno(saveindex), xpos(saveindex), ypos(saveindex), -1, -1
      Else
        MinTheta = MinTheta * 180 / pi
        If MinTheta < Angle Or MinTheta > -Angle Then
          Write #3, posno(saveindex), xpos(saveindex), ypos(saveindex), MinTheta, 10
        Else
          Write #3, posno(saveindex), xpos(saveindex), ypos(saveindex), MinTheta, 0
        End If
      End If

      saveindex = saveindex + 1

Next index3
```

```
    Beep
    Beep

End Sub
```

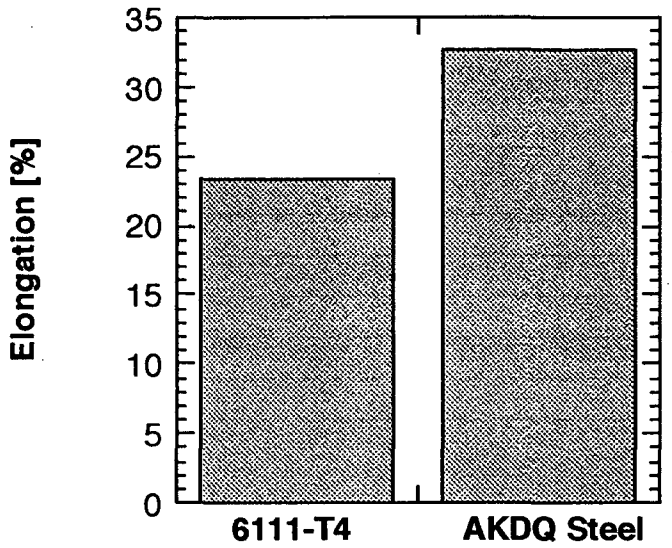

Figure 1: Uniaxial tensile elongations for 6111-T4 and AKDQ steel.

a)

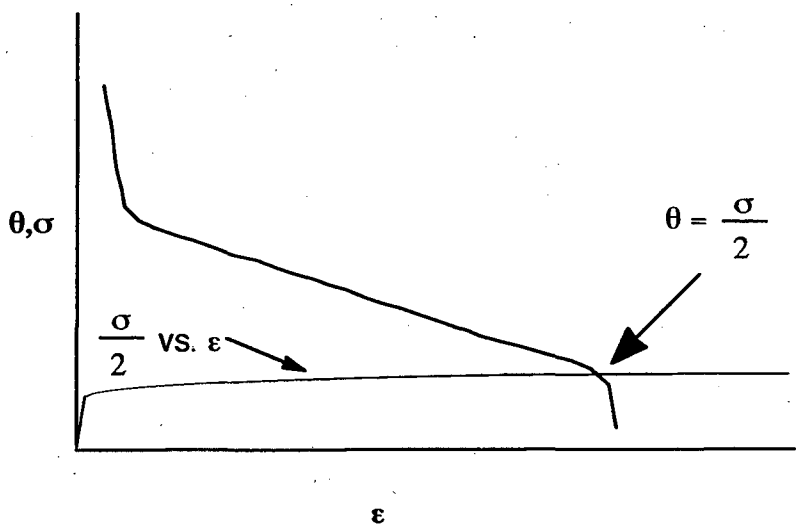

Figure 2a: Schematic plot of the work hardening rate, θ, and one-half true stress, $\frac{\sigma}{2}$, versus true strain, ε. The upper curve is the work hardening rate, and the lower curve (shaded) is the $\frac{\sigma}{2}$ vs. ε. Where the two curves meet is where the local necking criterion theoretically occurs.

b)

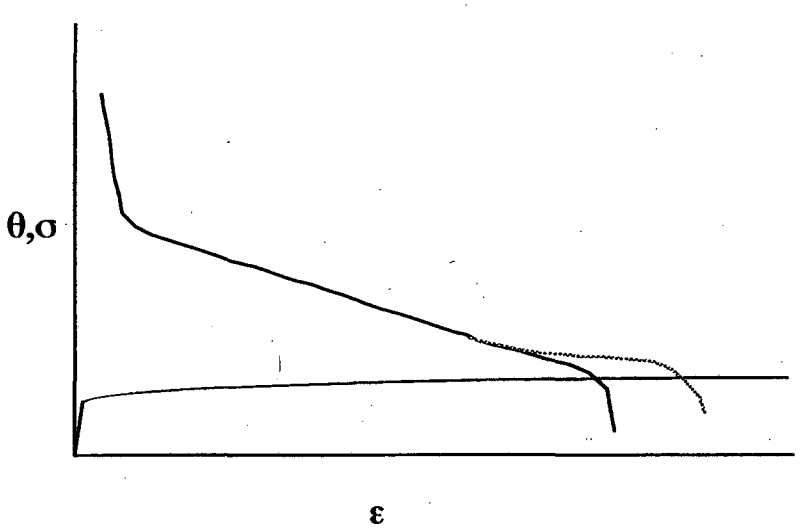

Figure 2b: A higher work hardening rate at higher strains (shaded curve) will delay the onset of necking and increase the elongation of the material.

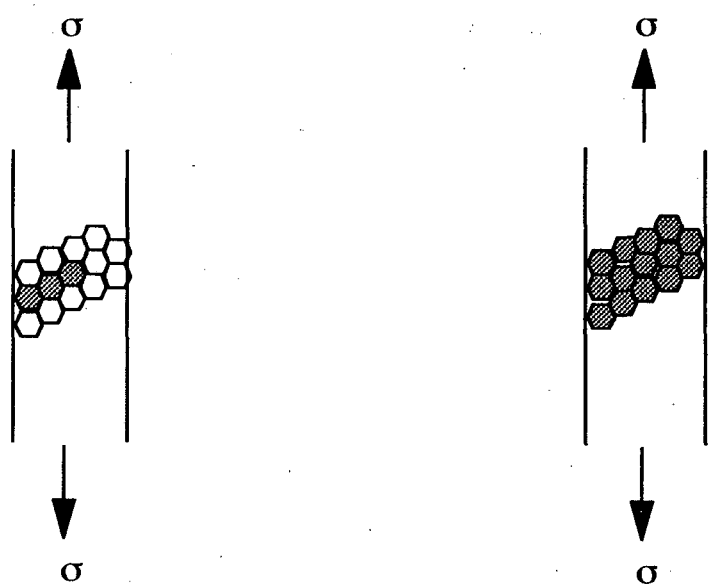

Figure 3: Local deformation occurs on the macroscopic scale. The size can range from deformation occurring in a few grains (left), or deformation islands, to spanning the width of the sample (right), or deformation bands.

a)

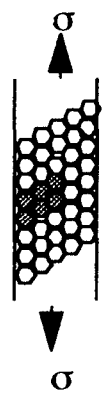

Figure 4a: Deformation islands and bands can form and propagate through a cluster of similarly oriented grains. The shaded grains have an orientation that is different from the surrounding grains.

b)

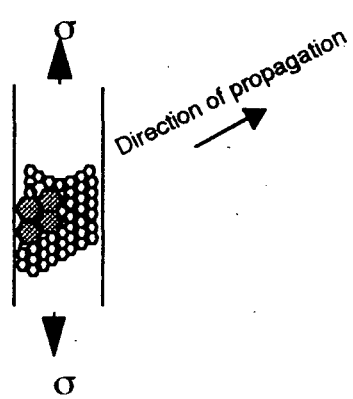

Figure 4b: The shaded grains form a cluster of large sized grains. These large sized grains act as a "soft" area through which islands can form and propagate. The arrow indicates the direction in which the deformation will propagate.

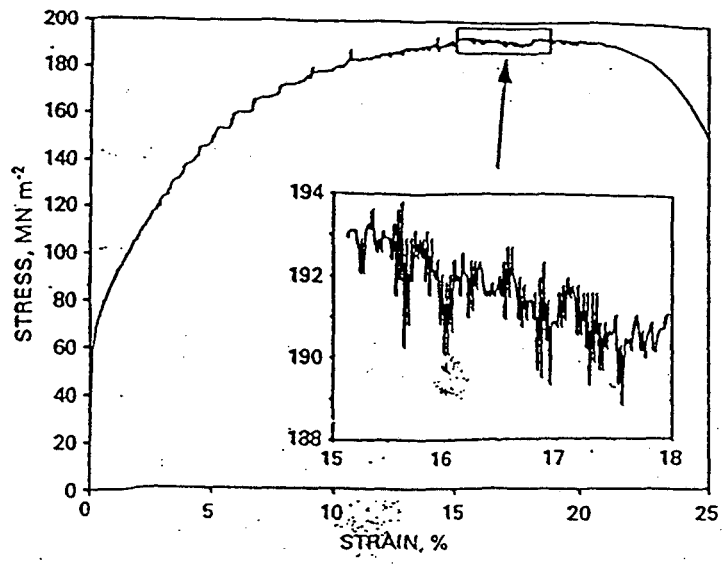

Figure 5: Stress-strain curve of 6061 [Robinson, 1994]. Serrations due to the PLC effect can be seen in the curve and are magnified in the inset. Longer wavelength oscillations, of varying amplitude, are also seen in the figure.

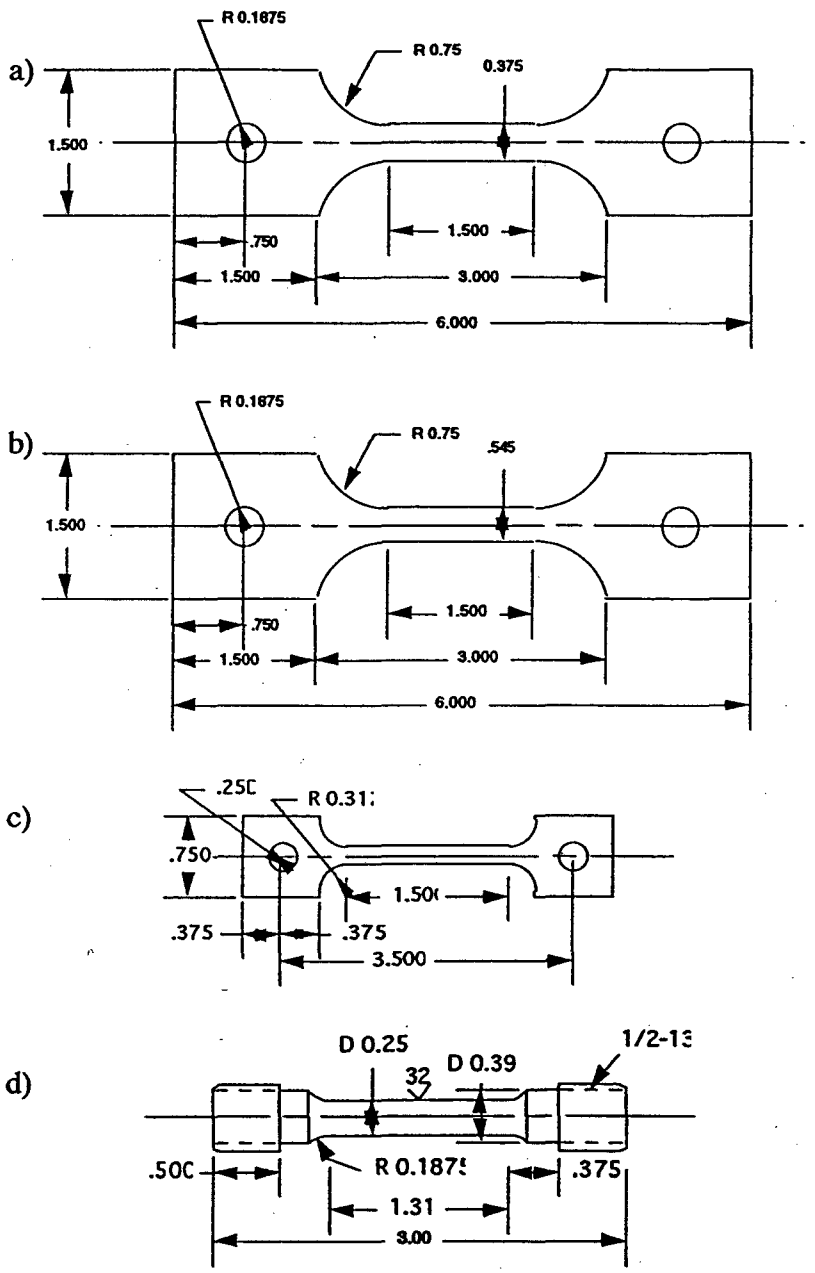

Figure 6: Drawings of the specimen dimensions for various tensile samples: a) standard, b) 6111-T4 wide, c) narrow [Chan] and d) round cross-section [Chan]. Note: drawings are not to scale.

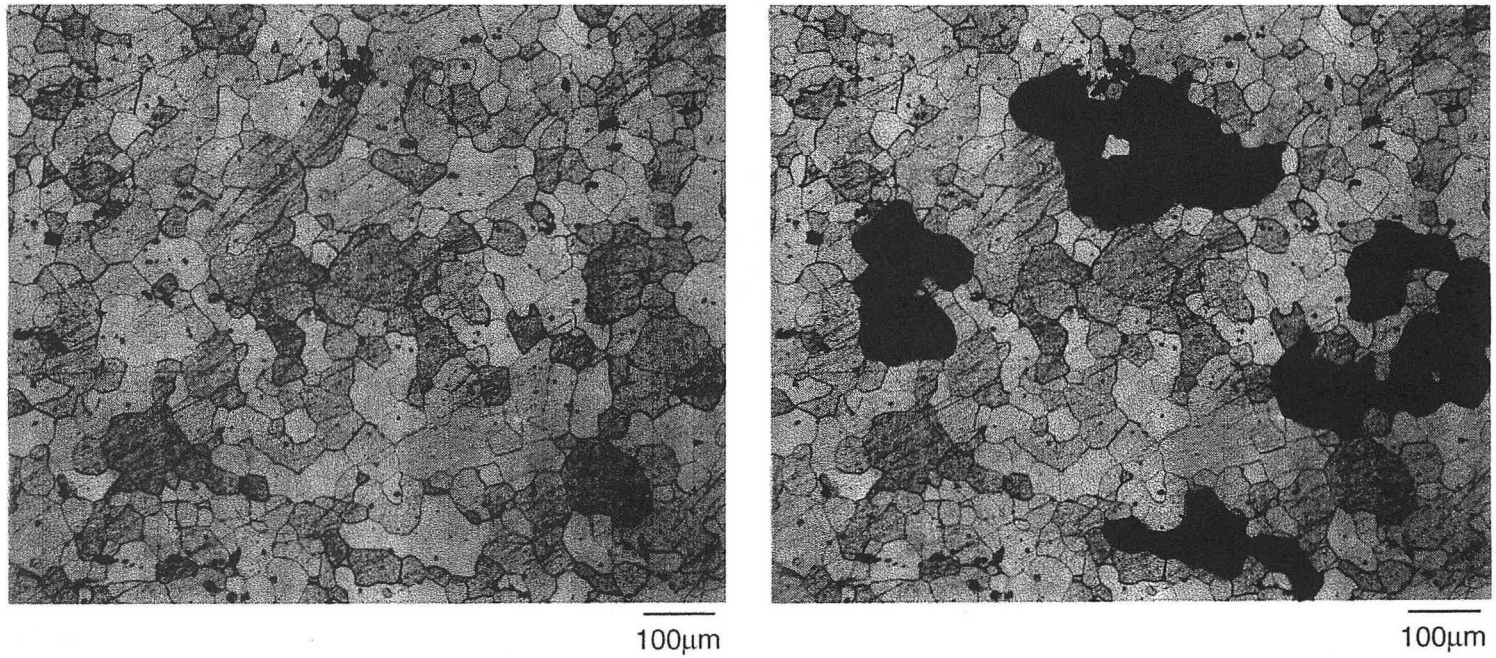

a) b)

Figure 7: a) Optical micrograph of the grain structure in 6111-T4. There is clustering of grains with similar shades of gray. b) Same micrograph as that in a); clusters of large sized grains (> 50 μm) are colored in black.

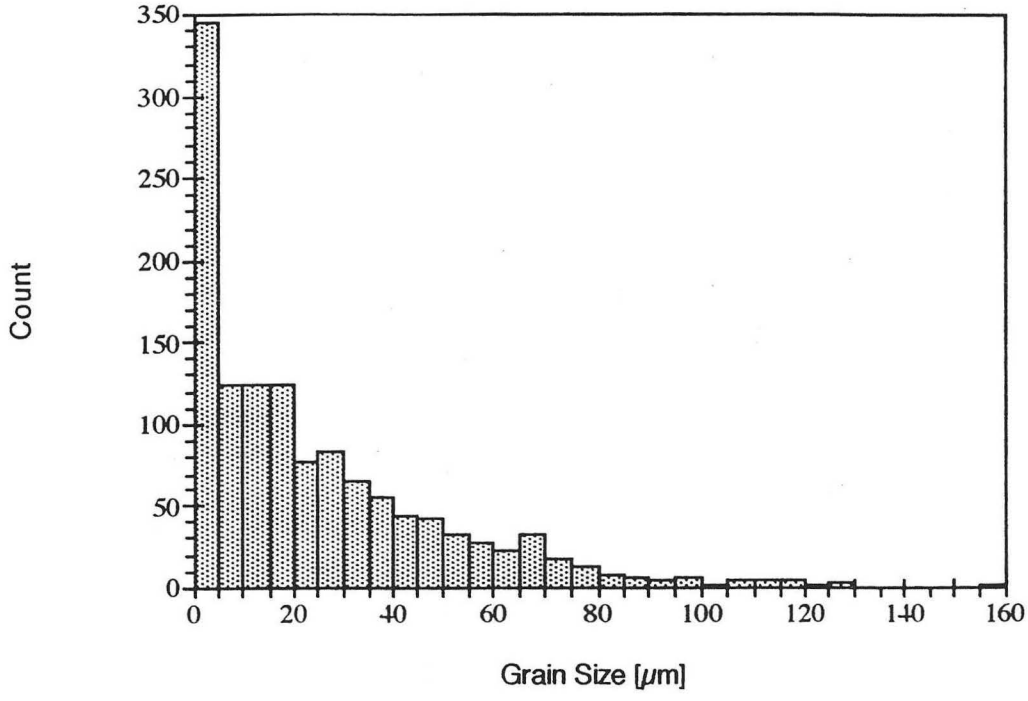

Figure 8: Histogram of the grain size distribution in 6111-T4.

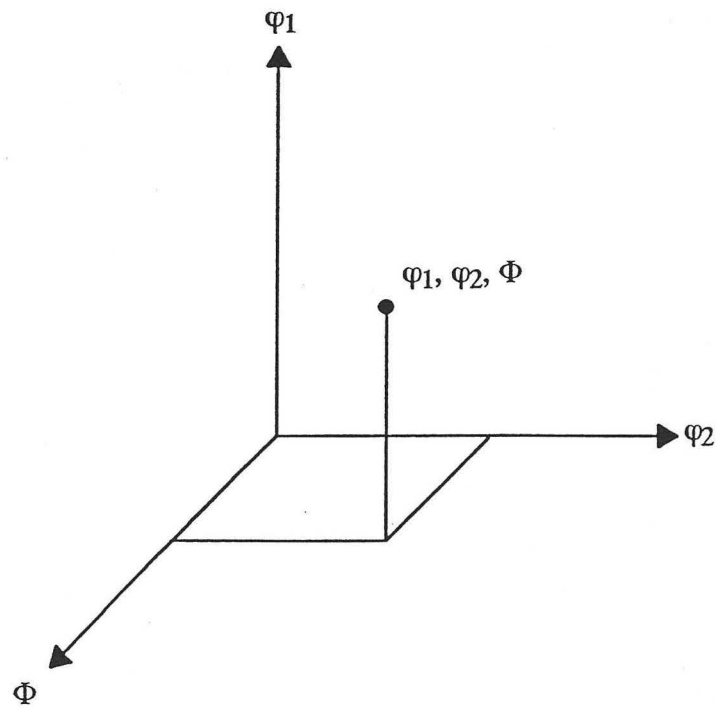

Figure 9: Plot of an orientation in Euler space.

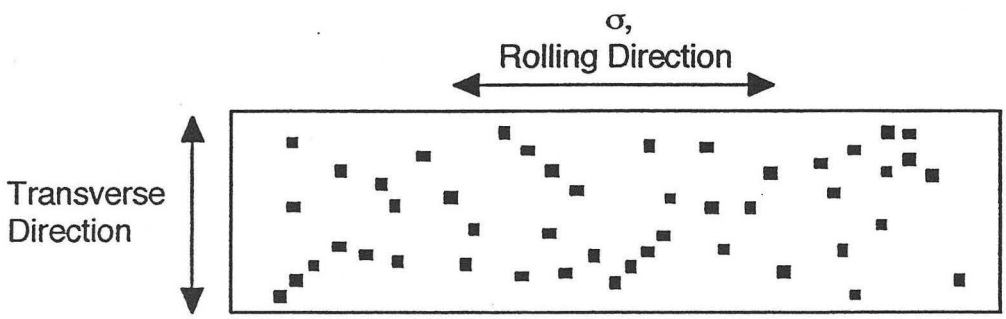

Figure 10: Schematic of grains with a particular orientation (dots) at a particular x-y location in a gage section of a tensile sample. This kind of plot is useful for determining which clusters of a particular orientation are located.

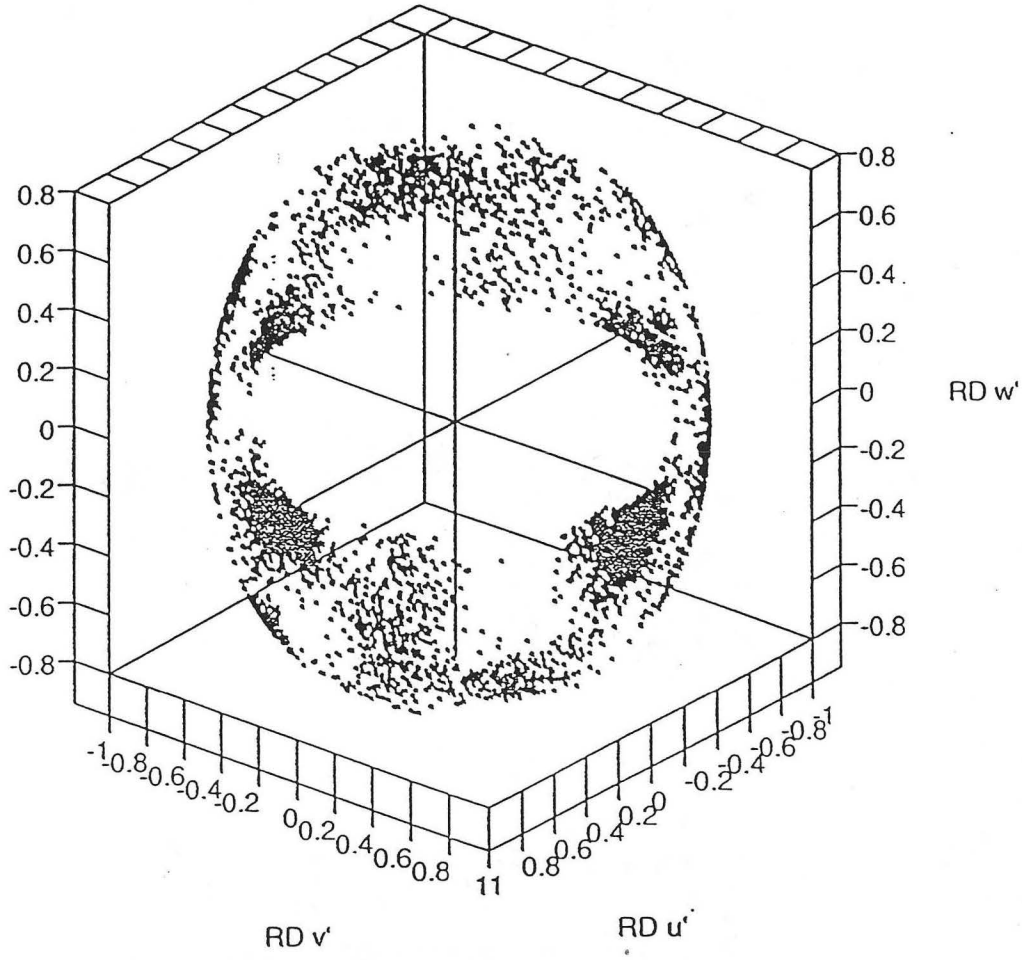

Figure 11: Euler angle plot of orientations found in a 6111-T4 sample. There is evidence of clustering of the orientations.

a)

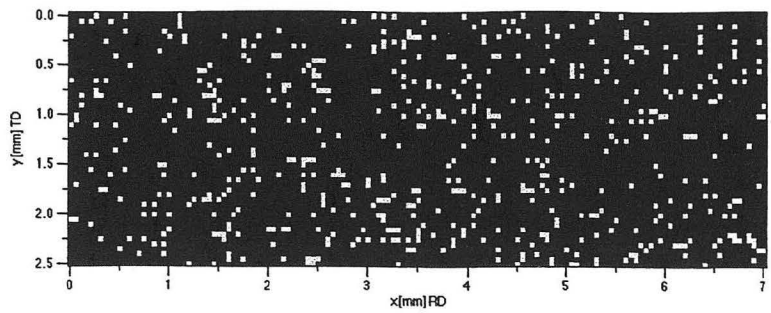

b)

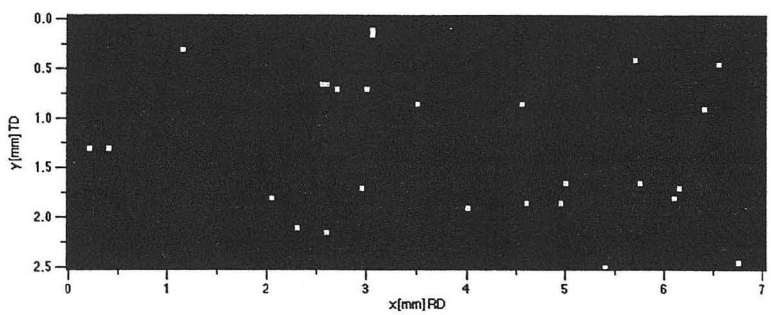

c)

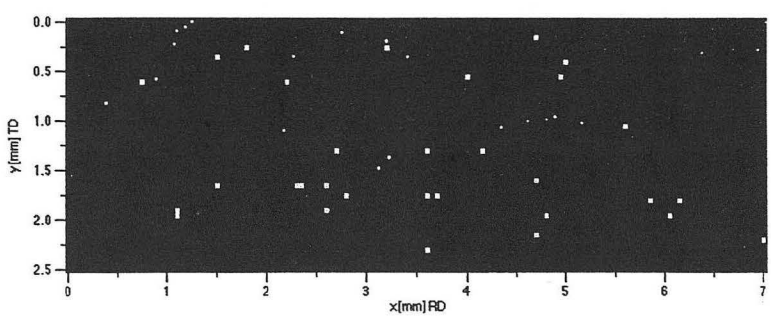

Figure 12: Plots of grains with a particular orientation at their respective x-y coordinates in the gage section: a) Cube {100}<001>, b) Goss {110} <001>, and c) R {124}<211>. Rolling direction (RD), which is also the direction of the tensile axis, is in the x-direction, and the transverse direction (TD) is in the y-direction. Clustering of grains is observed in the Cube texture.

d)

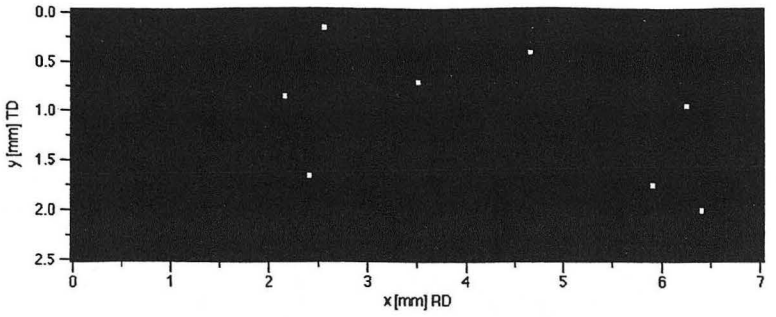

e)

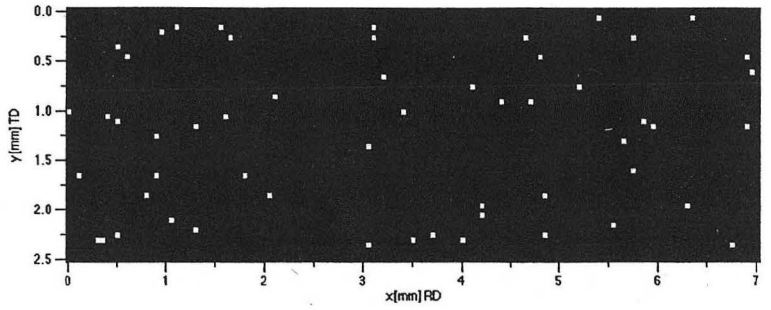

f)

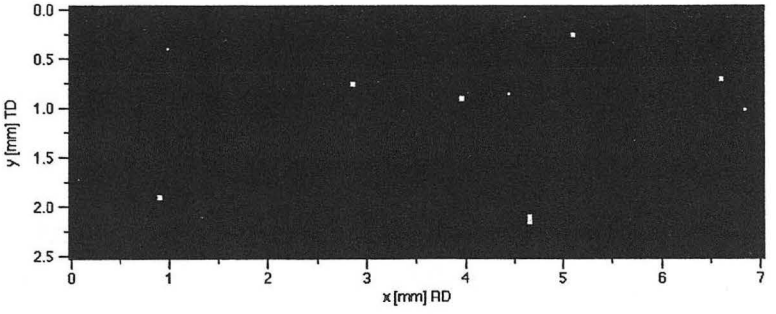

Figure 12: Plots of the grains with a particular orientation at their respective x-y coordinates in the gage section: d) P {011}<122>, e) Q {013}<231>, and f) Copper {112}<111>. Rolling direction (RD), also the tensile direction, is in the x-direction, and the transverse direction (TD) is in the y-direction:

g)

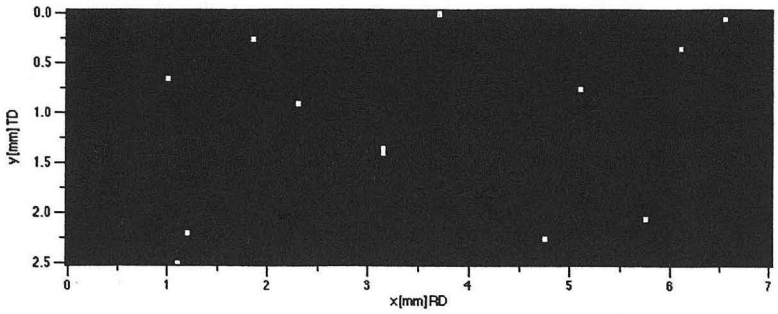

h)

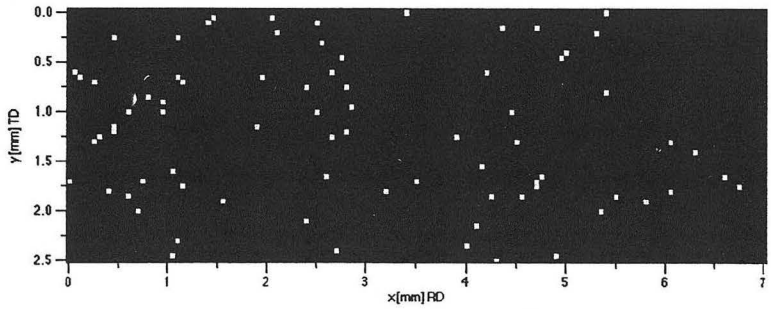

Figure 12: Plots of the grains with a particular orientation at their respective x-y coordinates in the gage section: g) Brass {{011}<211> and h) S {123}<634>. Rolling direction (RD), also the tensile direction, is in the x-direction, and the transverse direction (TD) is in the y-direction. The S texture has clusters of grains, and many of these clusters are at an angle to the rolling and tensile directions.

a)

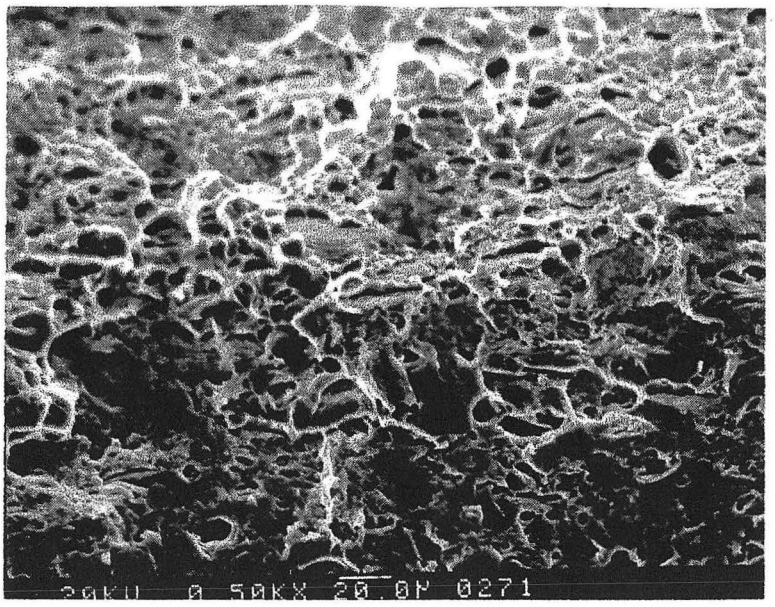

b)

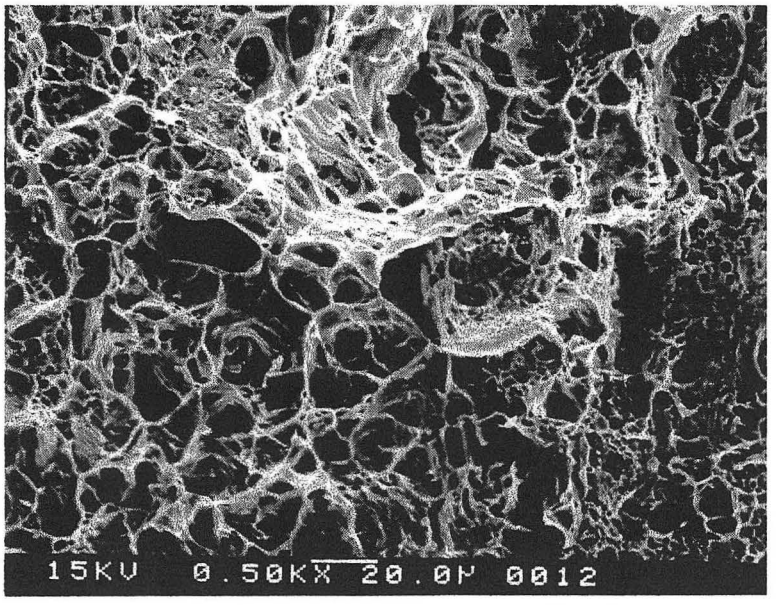

Figure 13: SEM micrographs of the fracture surfaces of 6111-T4, in the longitudinal direction, at various test conditions. a) 10^{-4} /s, 300K and b) 10^{-1} /s, 300K. The fracture micromode is ductile for both test conditions.

c)

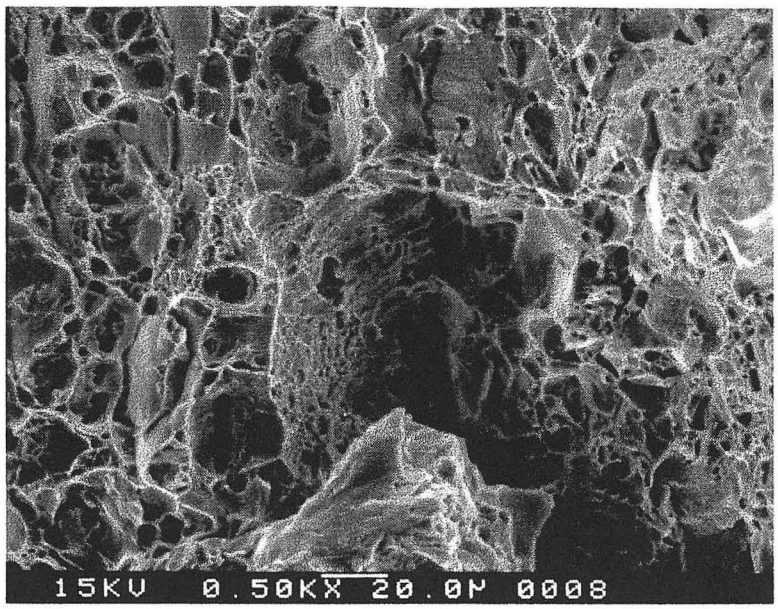

d)

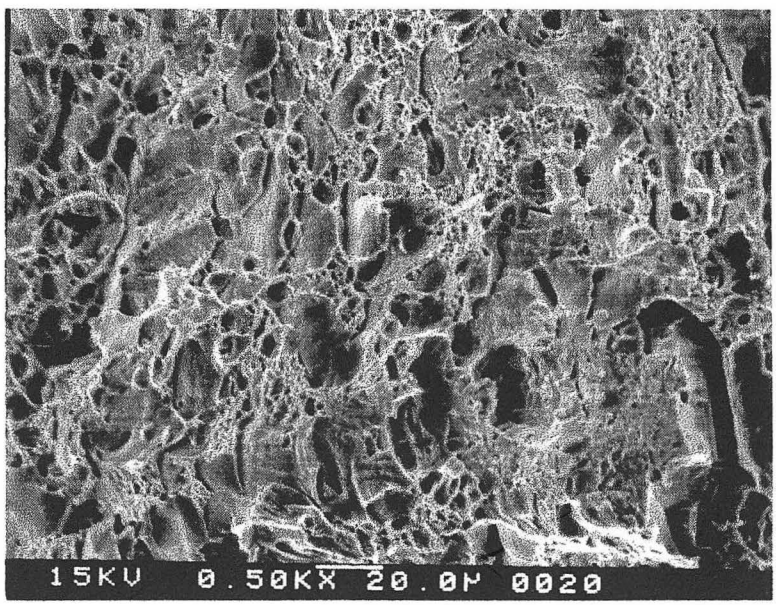

Figure 13: SEM micrographs of the fracture surfaces of 6111-T4 in the longitudinal direction at various test conditions. c) 10^{-4} /s, 77K and d) 10^{-1} /s, 77K. The fracture micromode is ductile for both test conditions.

e)

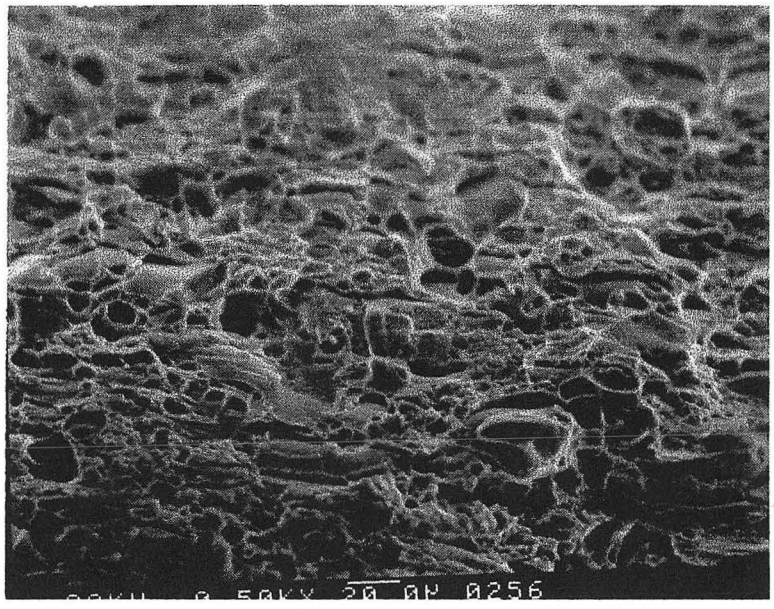

Figure 13e: SEM micrograph of the fracture surface of 6111-T4 in the longitudinal direction at 4K, 10^{-1} /s. The fracture micromode remains ductile.

a)

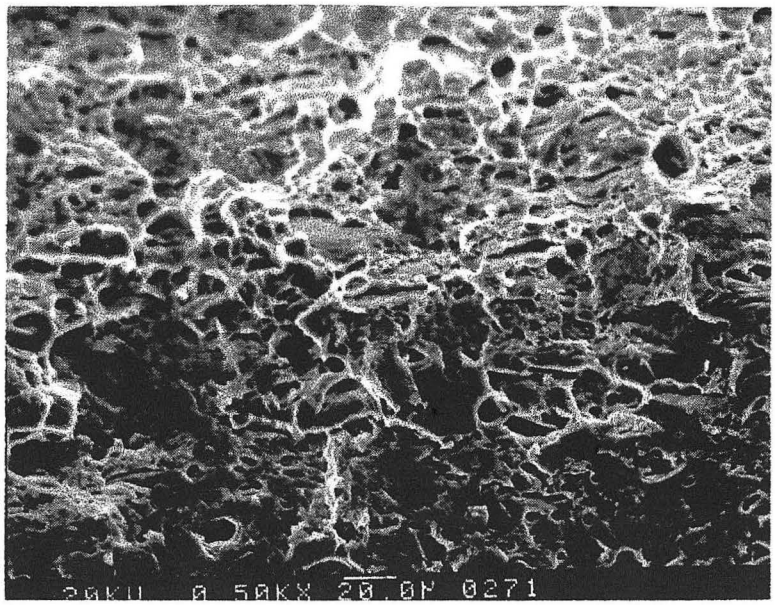

b)

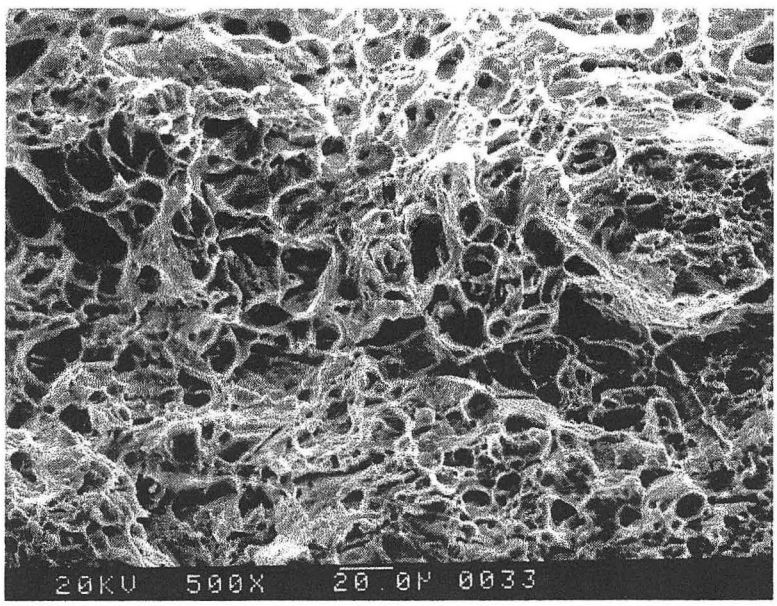

Figure 14: SEM micrographs of the fracture surfaces of 6111-T4, in the transverse direction, at various test conditions. a) 10^{-4} /s, 300K and b) 10^{-1} /s, 300K. The fracture micromode is ductile for both test conditions.

c)

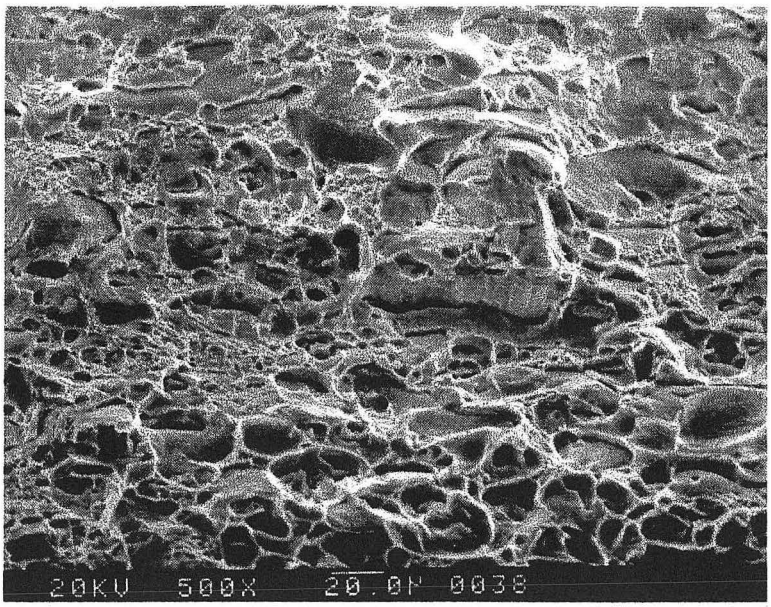

d)

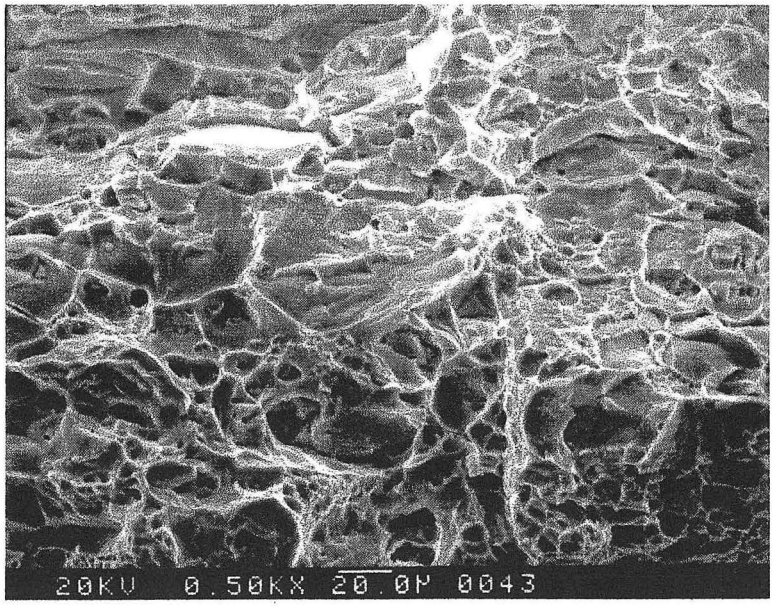

Figure 14: SEM micrographs of the fracture surfaces of 6111-T4 in the transverse direction at various test conditions. c) 10^{-4} /s, 77K and d) 10^{-1} /s, 77K. The fracture micromode is ductile for both test conditions.

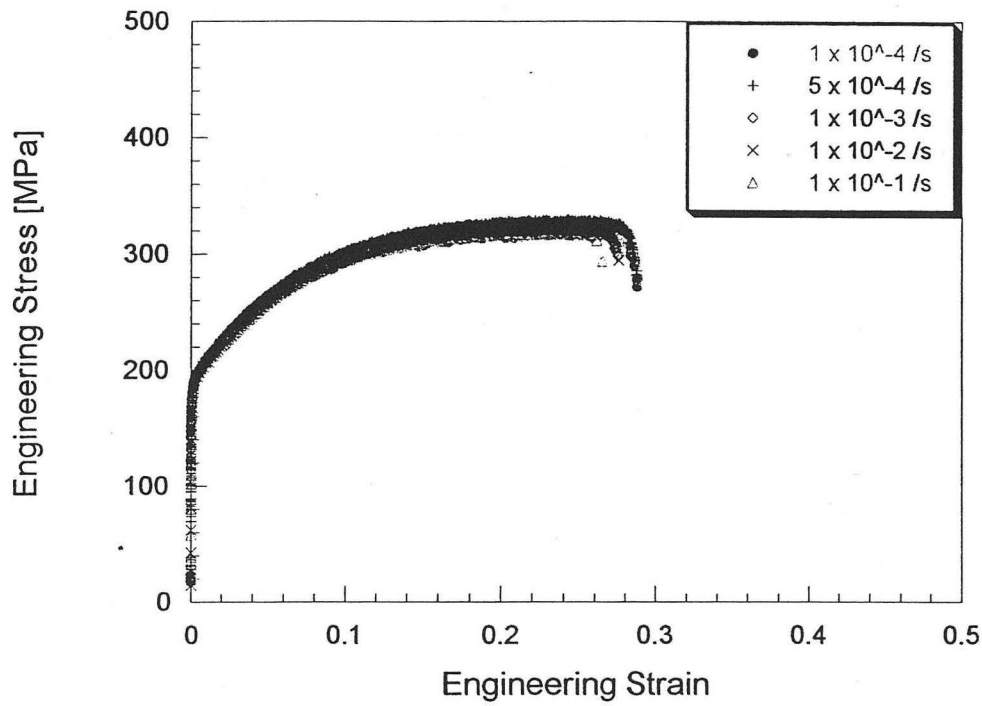

Figure 15: Engineering stress-strain curves of 6111-T4 longitudinal samples at 300K and at strain rates of 10^{-4}, 5×10^{-4}, 10^{-3}, 10^{-2}, and 10^{-1} /s . Despite the three orders of magnitude increase in strain rate, the stress-strain behavior does not significantly change.

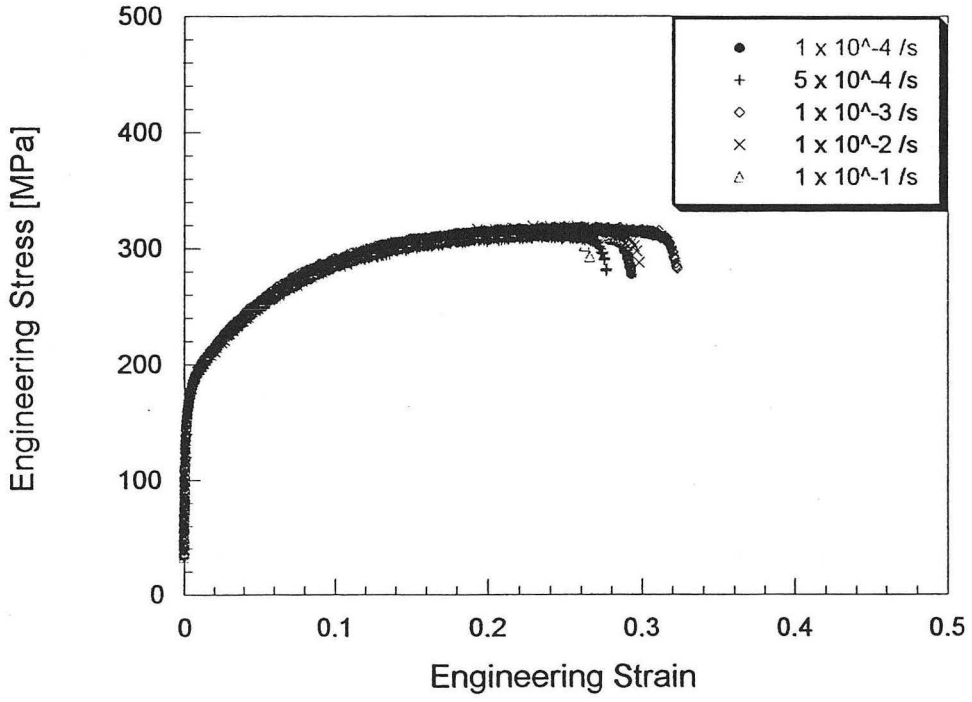

Figure 16: Engineering stress-strain curves of 6111-T4 transverse samples at 300K and at strain rates of 10^{-4}, 5×10^{-4}, 10^{-3}, 10^{-2}, and 10^{-1} /s . Despite the three orders of magnitude increase in strain rate, the stress-strain behavior does not significantly change.

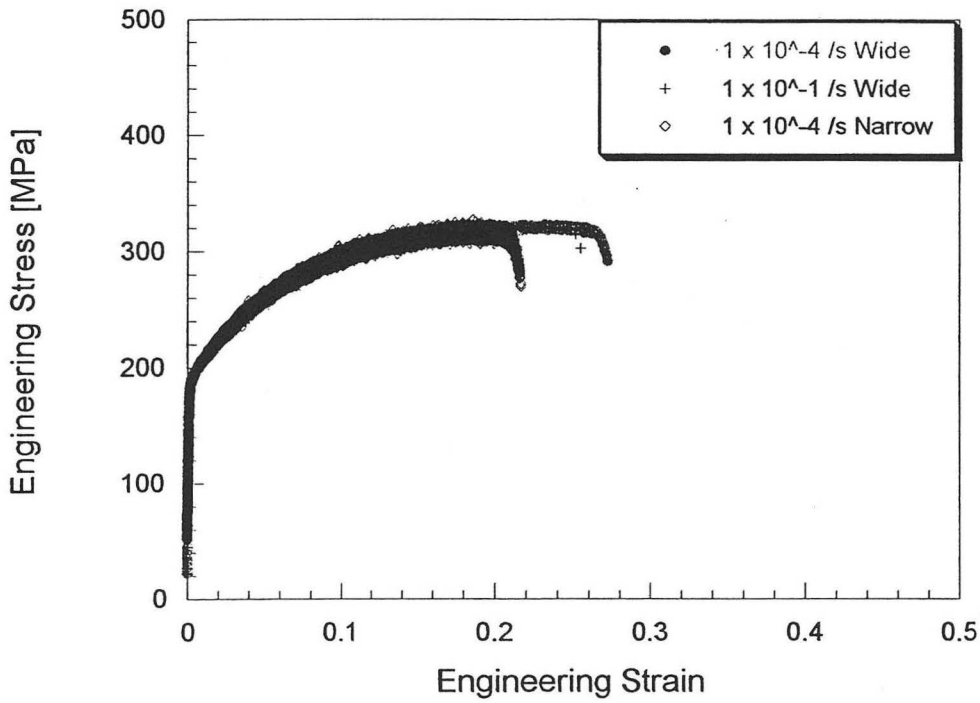

Figure 17: Engineering stress-strain curves of 6111-T4 at 300K and at strain rates of 10^{-4} and 10^{-1} /s with a change in geometry. Only minor changes in stress-strain behavior occur when the gage width increases.

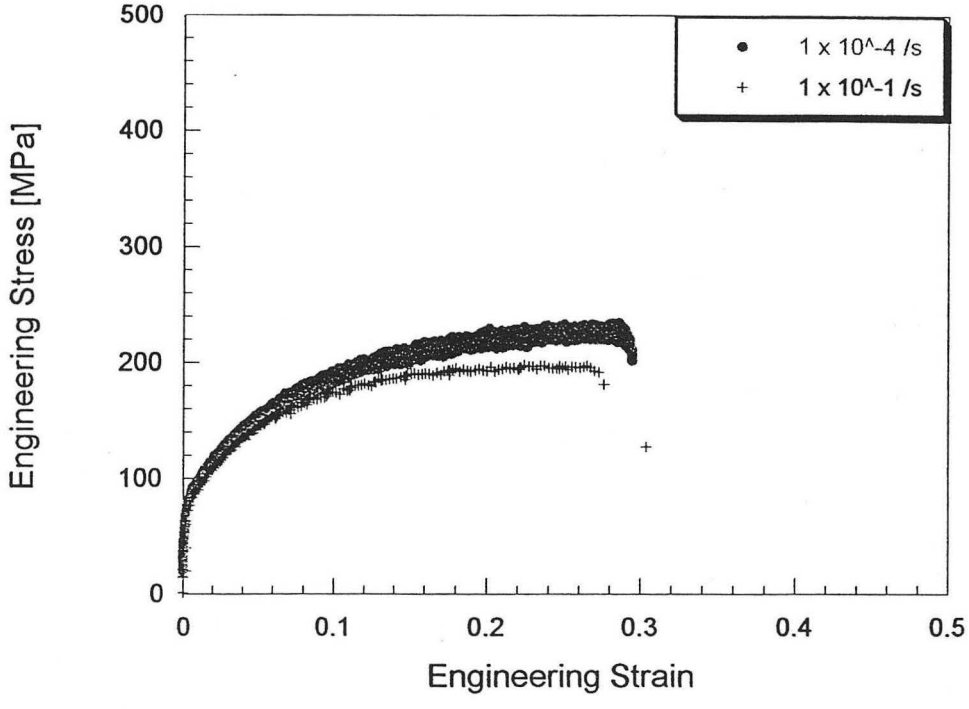

Figure 18: Engineering stress-strain curves of 6111 SHT at 300K and at strain rates of 10^{-4} and 10^{-1} /s. The stress-strain behavior changes with increasing strain rate.

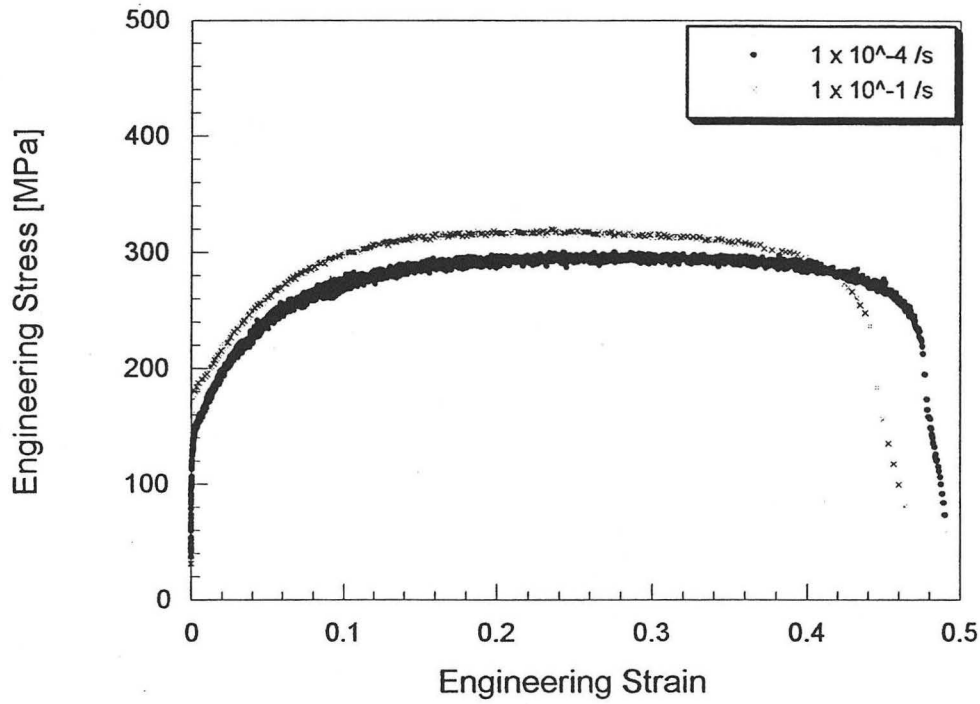

Figure 19: Engineering stress-strain curves of AKDQ steel at 300K and at strain rates of 10^{-4} /s (solid circles) and 10^{-1} /s (x). A change in strain rate does change the stress-strain behavior.

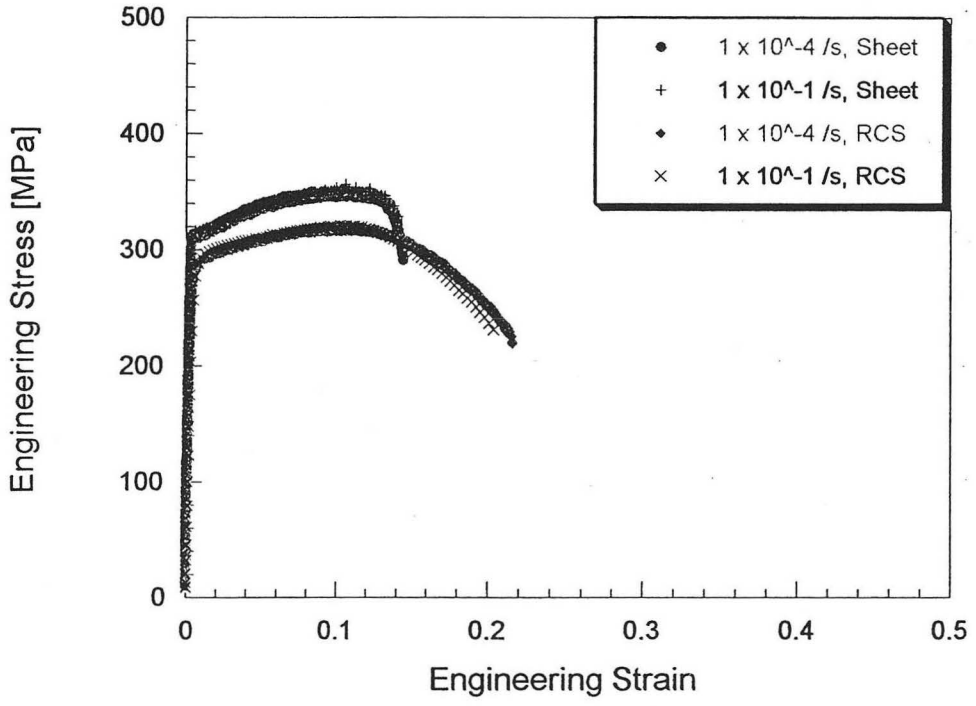

Figure 20: Engineering stress-strain curves of 6061-T6 at 300K and at strain rates of 10^{-4} and 10^{-1} /s for sheet and round cross-section samples. Minor changes occur in the stress-strain behavior with increasing strain rate. The stress-strain behavior changes dramatically with change in specimen geometry.

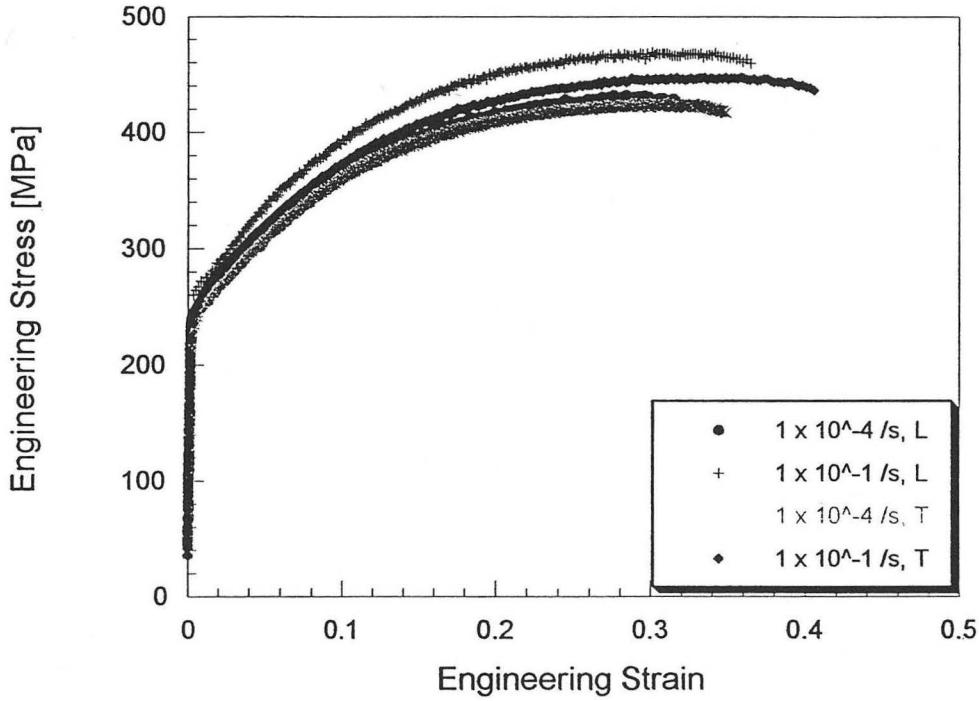

Figure 21: Engineering stress-strain curve of 6111-T4 at 77K and at strain rates of 10^{-4} and 10^{-1} /s for longitudinal and transverse samples. As compared with the 300K curves (figures 15 (longitudinal) and 16 (transverse)), the 77K behavior changes more dramatically with an increase in strain rate.

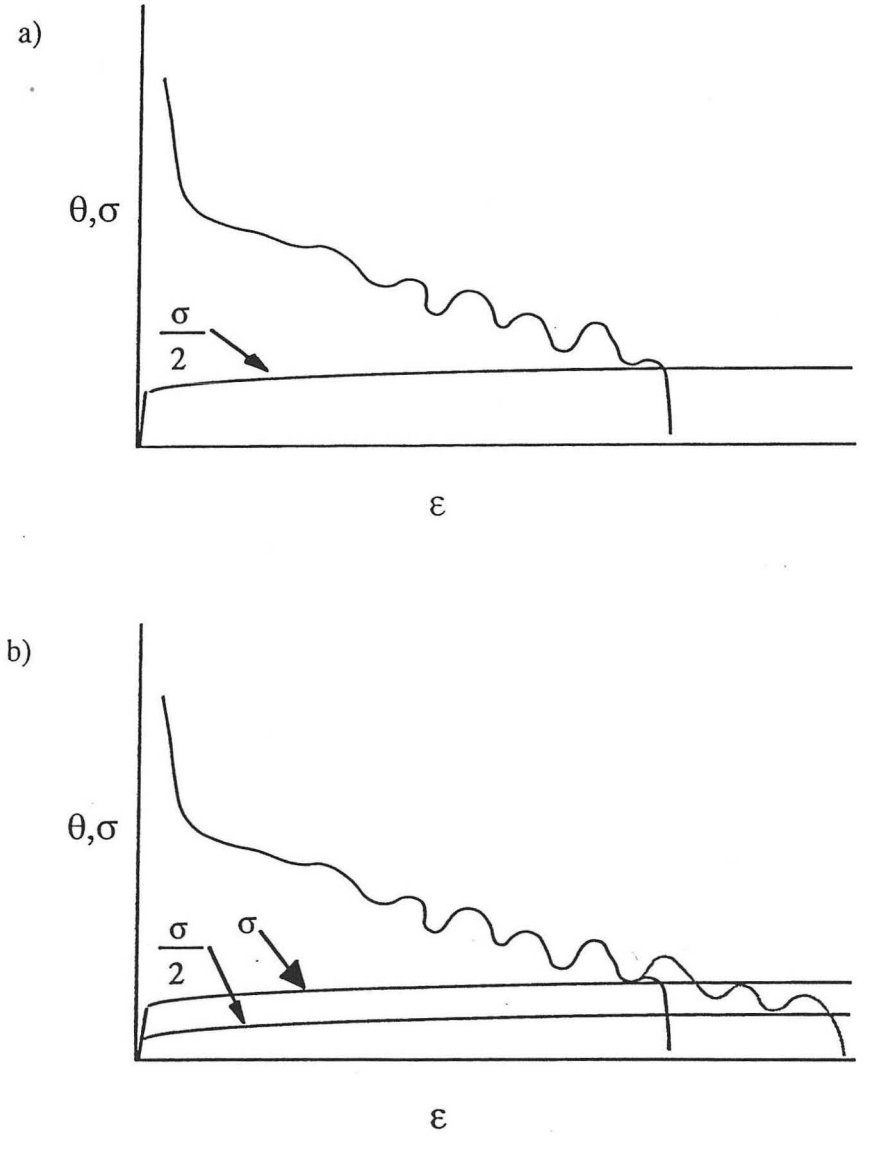

Figure 22: a) Schematic of a work hardening plot with oscillations. b) Schematic work hardening plot displaying a gradual work hardening drop off (shaded curve) versus a sharp drop off (solid) near the diffuse necking criterion.

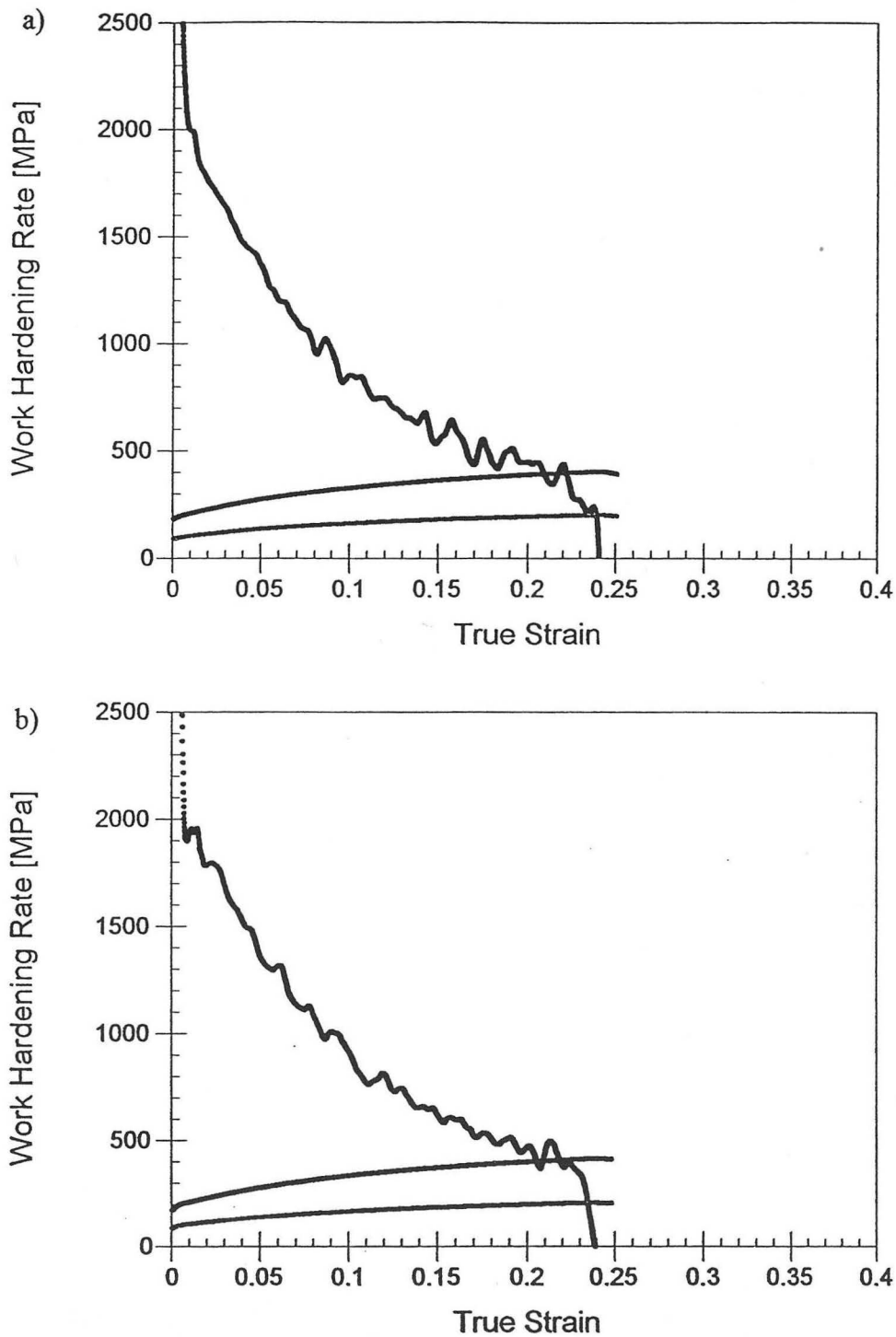

Figure 23: Plots of θ and $\frac{\sigma}{2}$ vs. ε for 6111-T4 longitudinal specimens tested at 300K: a) 10^{-4} /s and b) 5×10^{-4} /s.

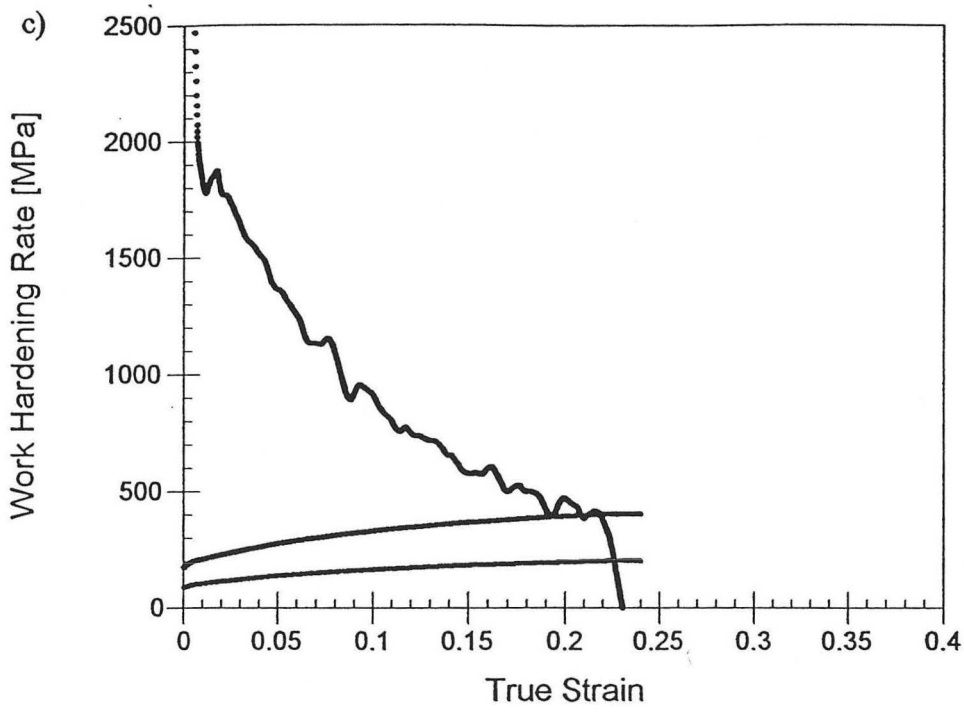

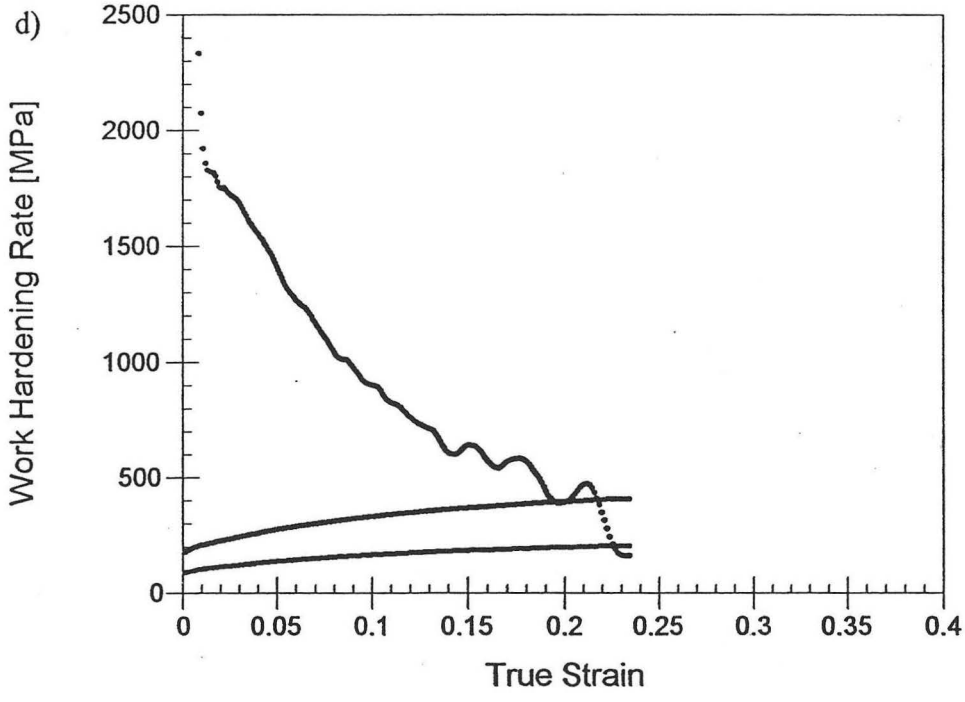

Figure 23: Plots of θ and $\frac{\sigma}{2}$ vs. ε for 6111-T4 longitudinal specimens tested at 300K: c) 10^{-3} /s and d) 10^{-2} /s.

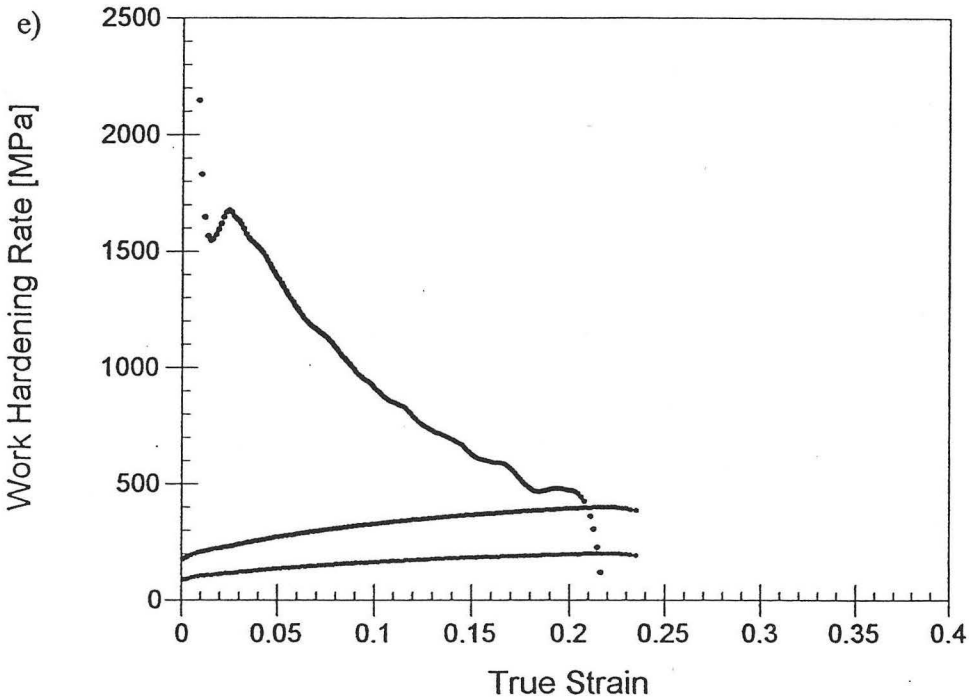

Figure 23: Plots of θ and $\frac{\sigma}{2}$ vs. ε for 6111-T4 longitudinal specimen tested at 300K: e) 10^{-1} /s.

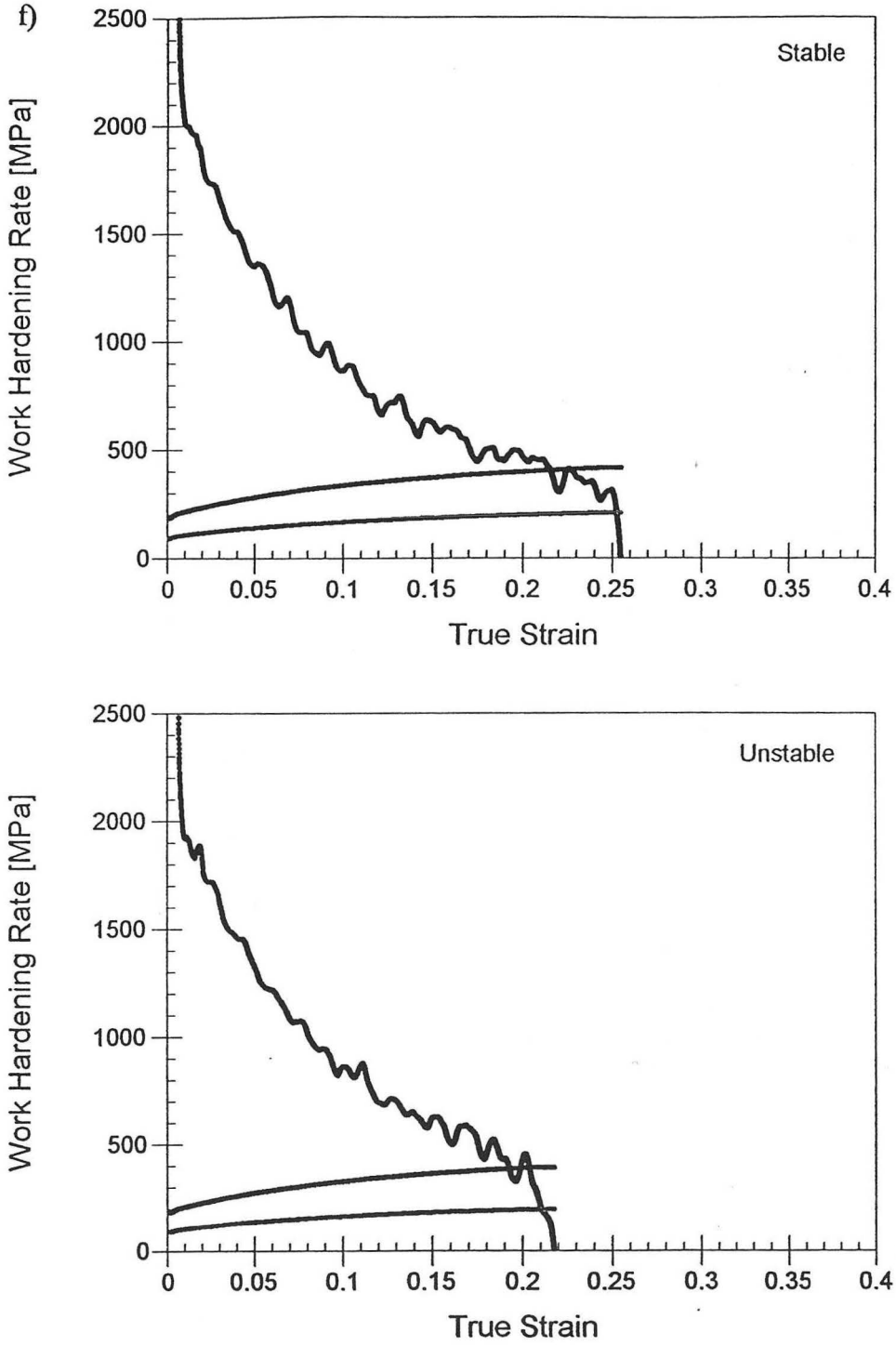

Figure 23: Plots of θ and $\frac{\sigma}{2}$ vs. ε for 6111-T4 longitudinal specimens tested at 300K: f) stable versus unstable at 10^{-4} /s.

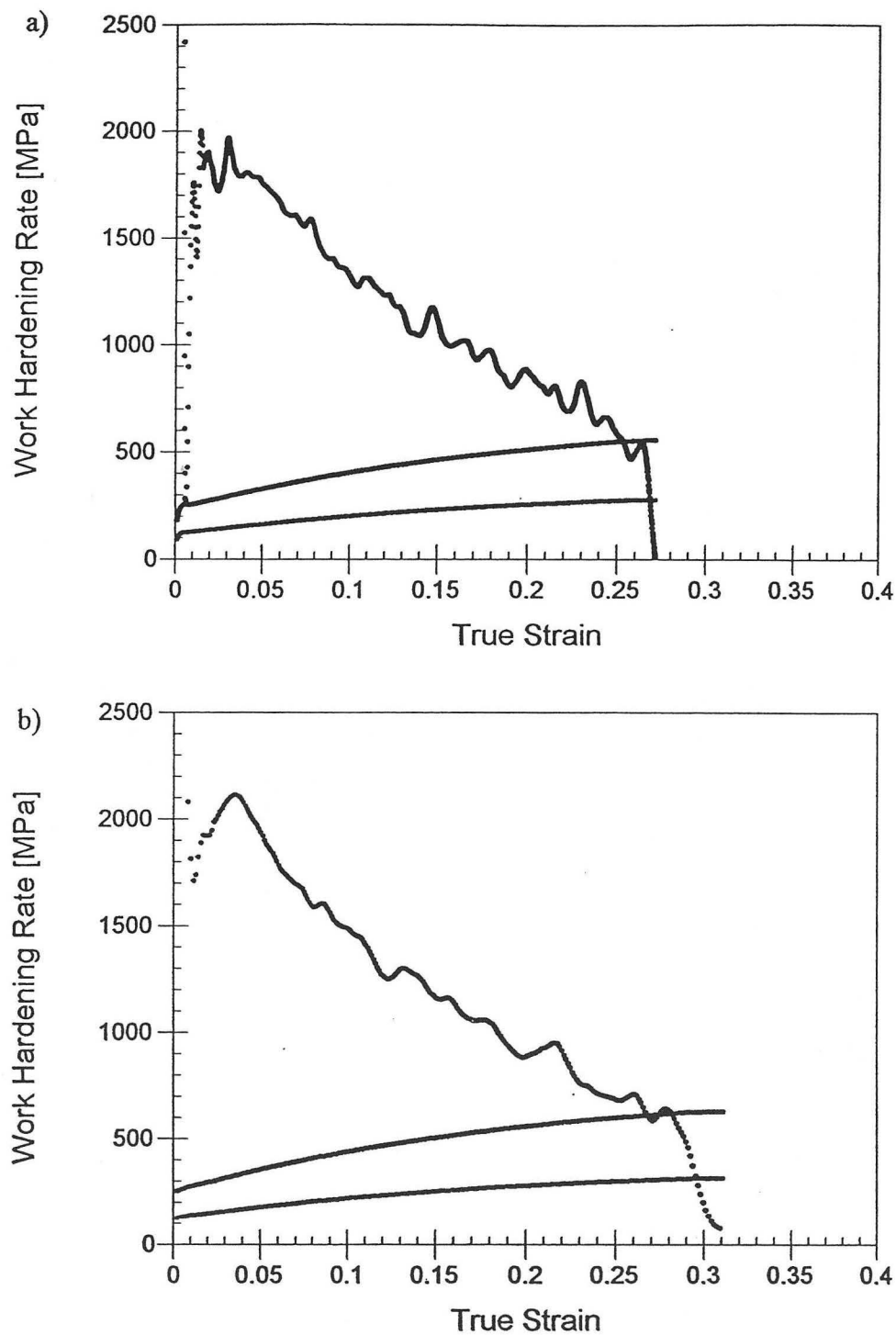

Figure 24: Plots of θ and $\frac{\sigma}{2}$ vs. ε for 6111-T4 longitudinal specimens tested at 77K: a) 10^{-4} /s and b) 10^{-1} /s.

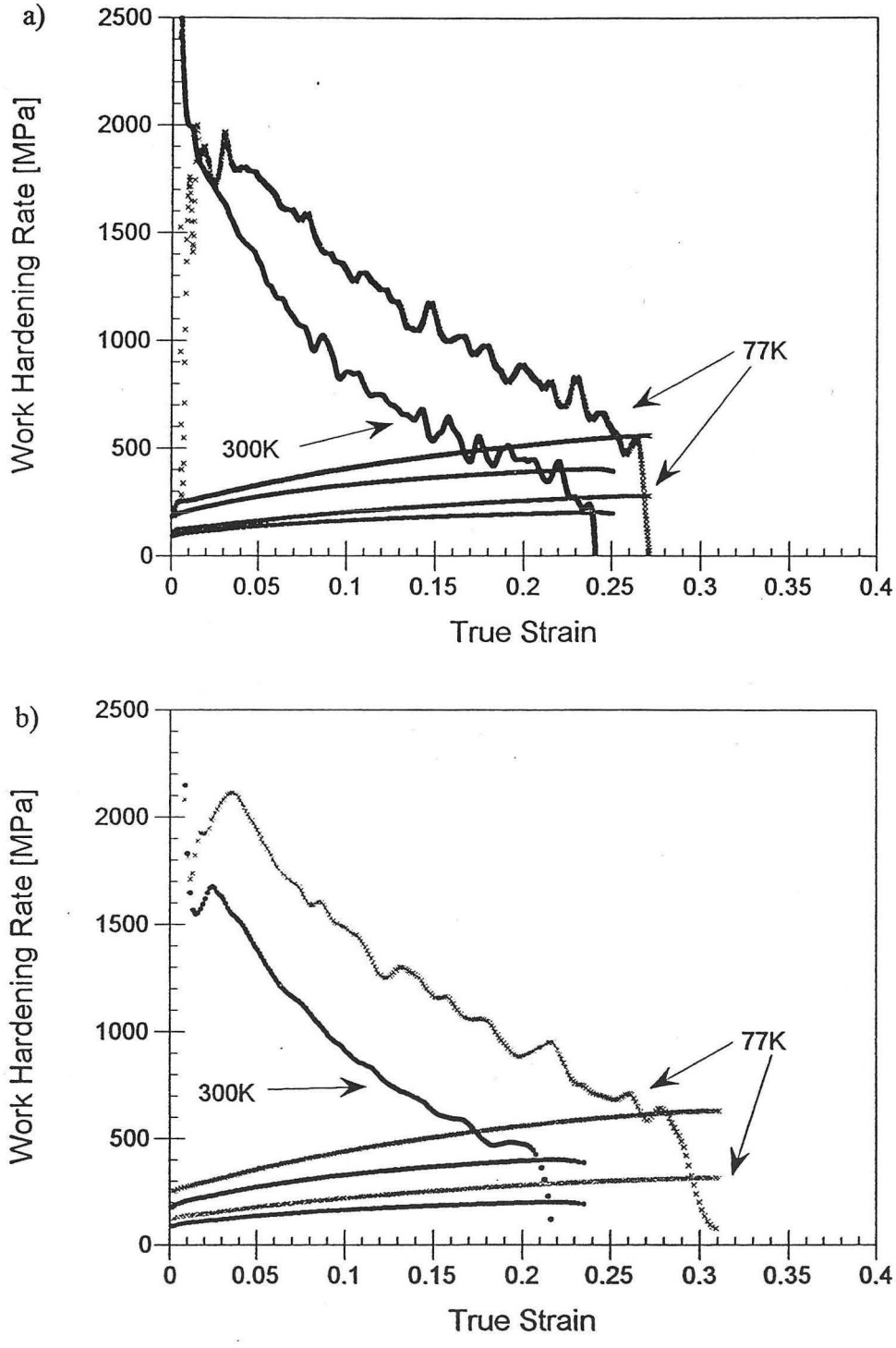

Figure 25: Plots of θ and $\frac{\sigma}{2}$ vs. ε for 6111-T4 longitudinal specimens tested at 300K and 77K: a) 10^{-4} /s and b) 10^{-1} /s.

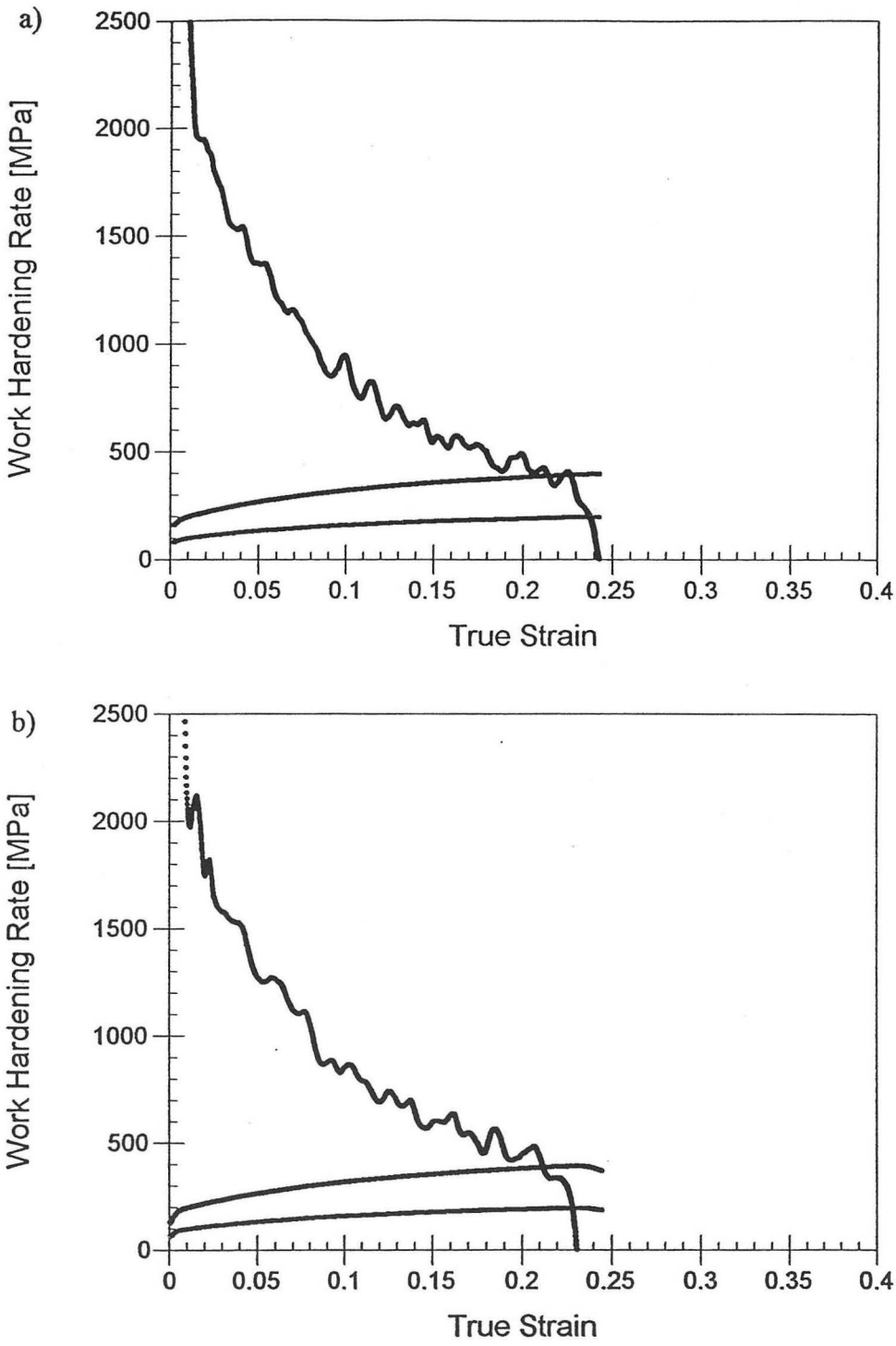

Figure 26: Plots of θ and $\frac{\sigma}{2}$ vs. ε for 6111-T4 transverse specimens tested at 300K: a) 10^{-4} /s and b) 5×10^{-4} /s.

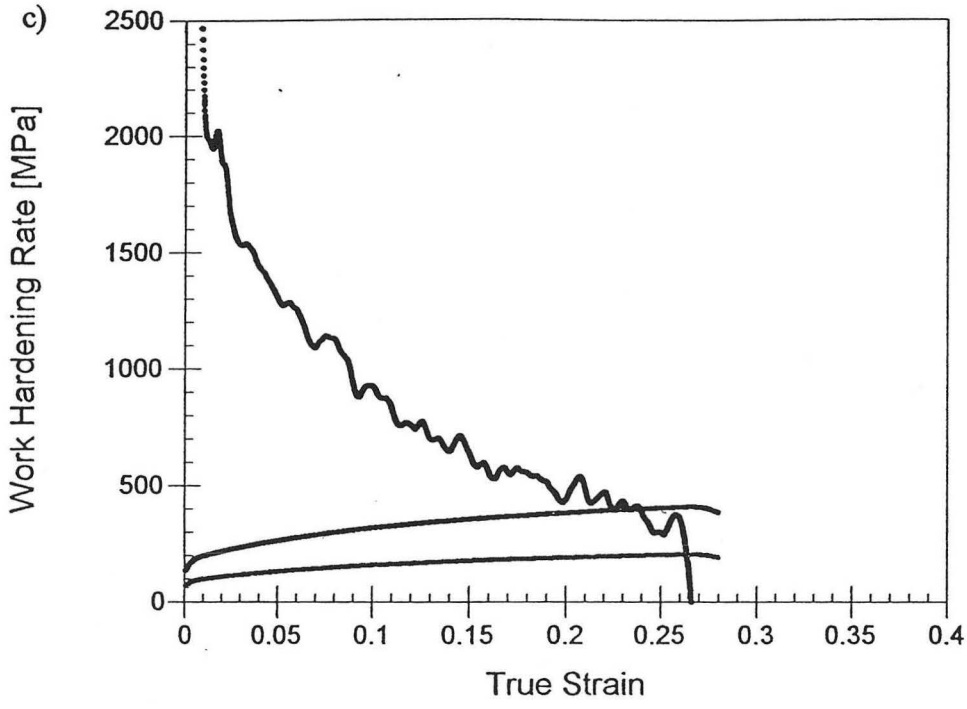

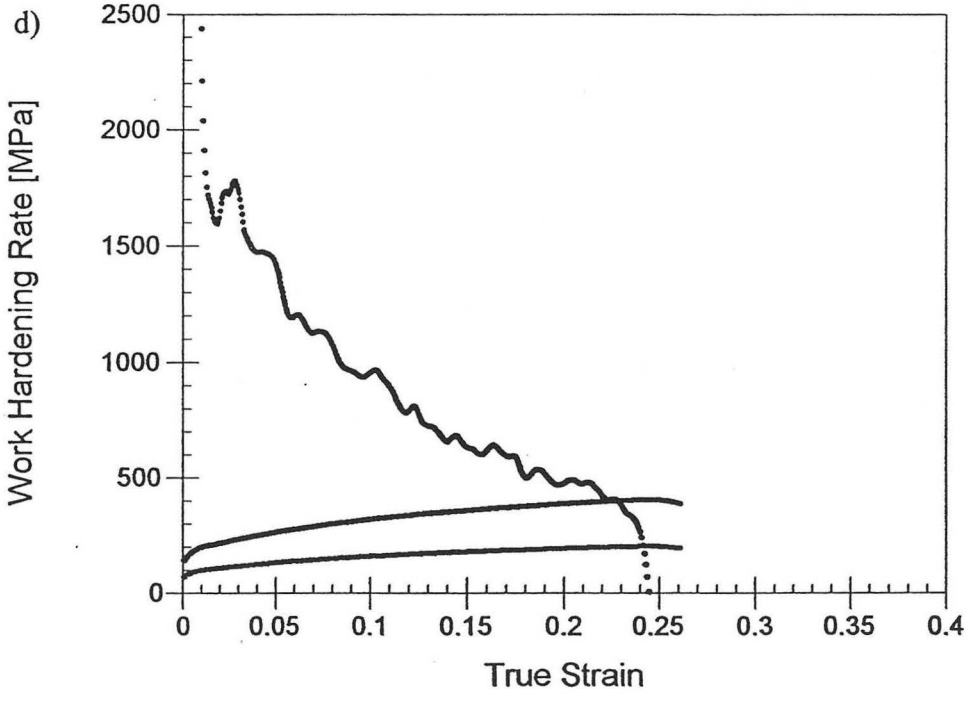

Figure 26: Plots of θ and $\frac{\sigma}{2}$ vs. ε for 6111-T4 transverse specimens tested at 300K: c) 10^{-3} /s and d) 10^{-2} /s.

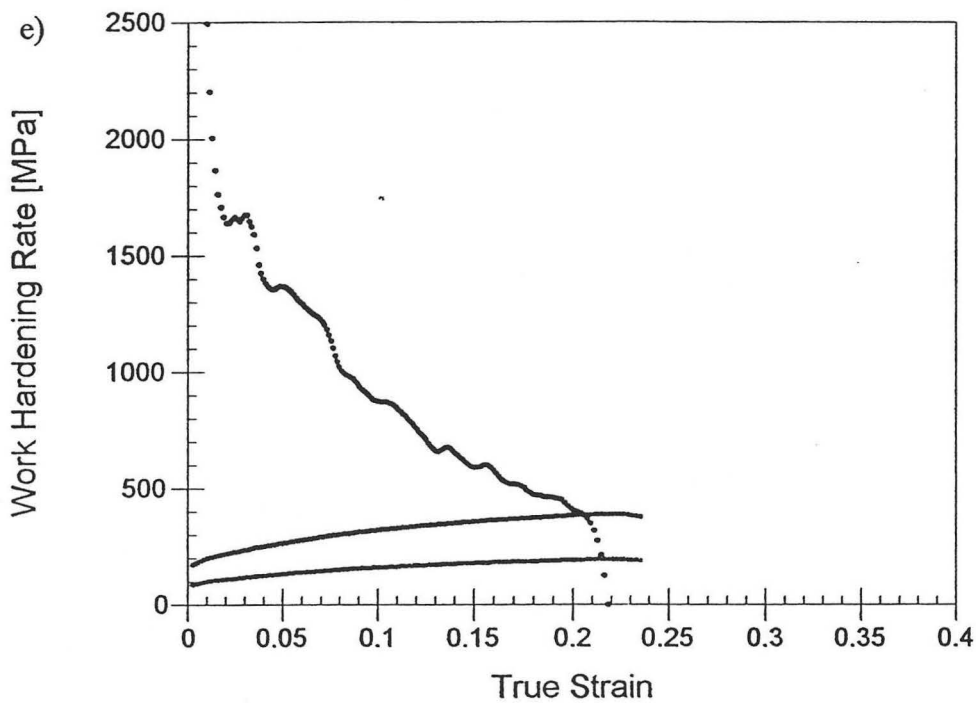

Figure 26: Plots of θ and $\frac{\sigma}{2}$ vs. ε for 6111-T4 transverse specimens tested at 300K: e) 10^{-1} /s.

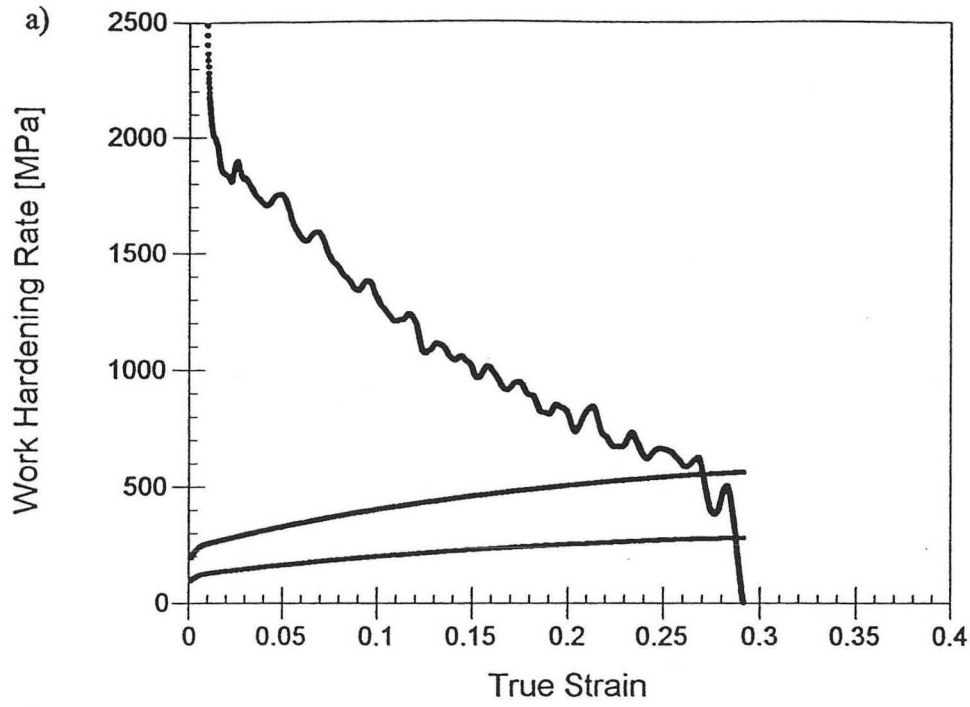

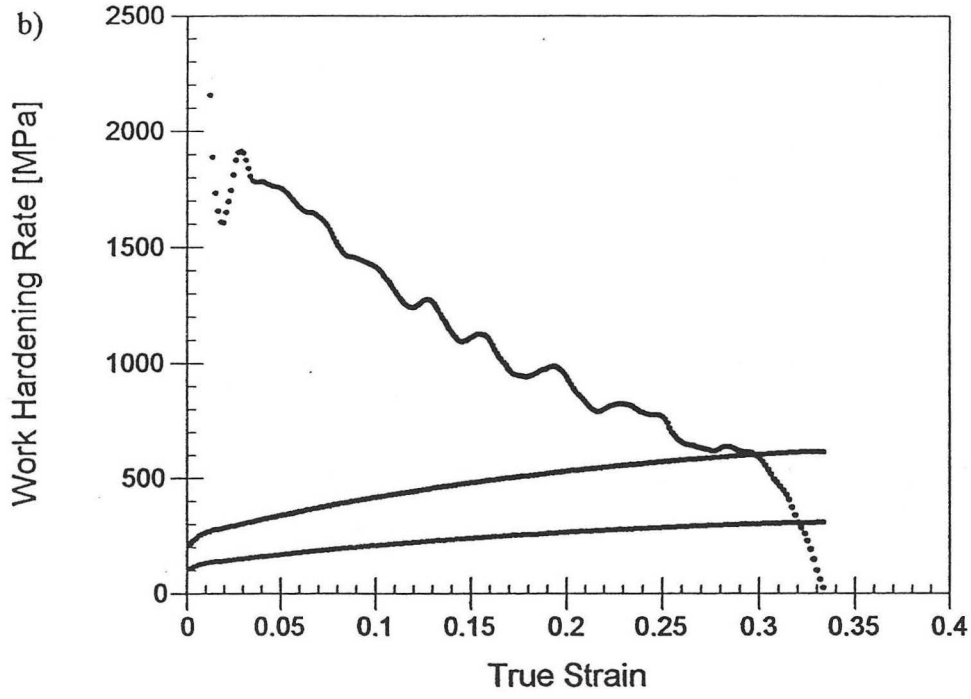

Figure 27: Plots of θ and $\frac{\sigma}{2}$ vs. ε for 6111-T4 transverse specimens tested at 77K: a) 10^{-4} /s and b) 10^{-1} /s.

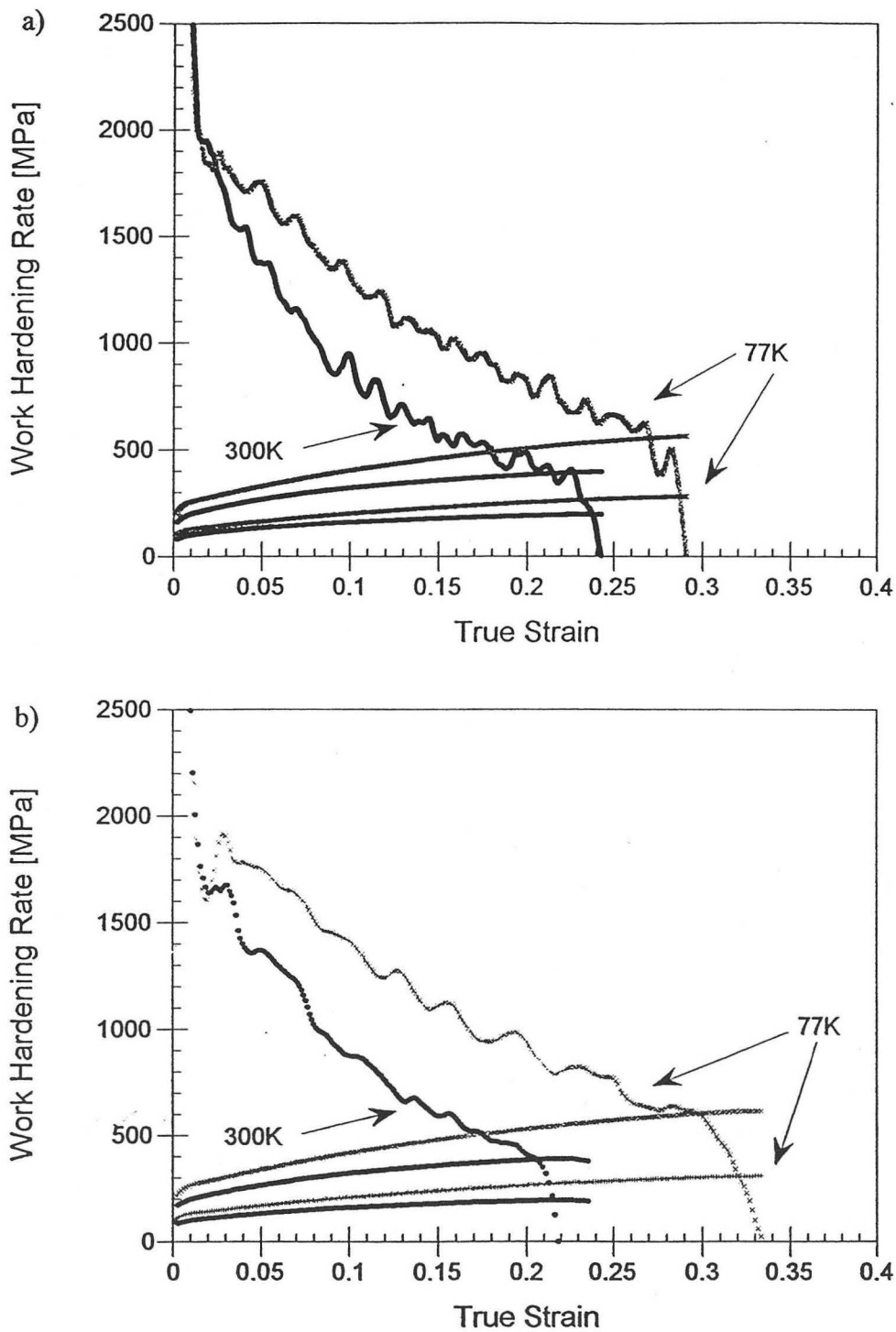

Figure 28: Plots of θ and $\frac{\sigma}{2}$ vs. ε for 6111-T4 transverse specimens tested at 300K and 77K: a) 10^{-4} /s and b) 10^{-1} /s.

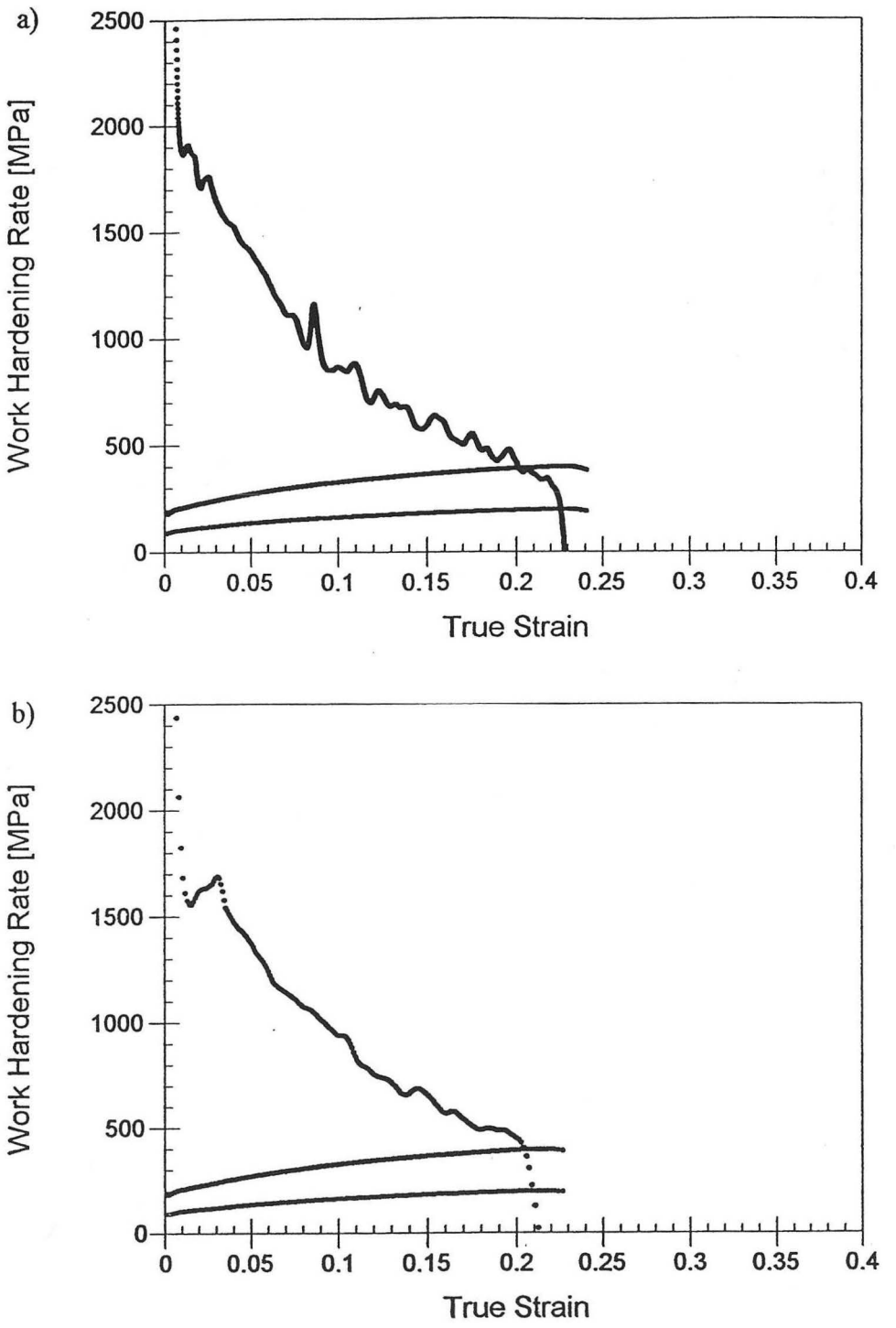

Figure 29: Plots of θ and $\frac{\sigma}{2}$ vs. ε for 6111-T4 wide specimens tested at 300K: a) 10^{-4} /s and b) 10^{-1} /s.

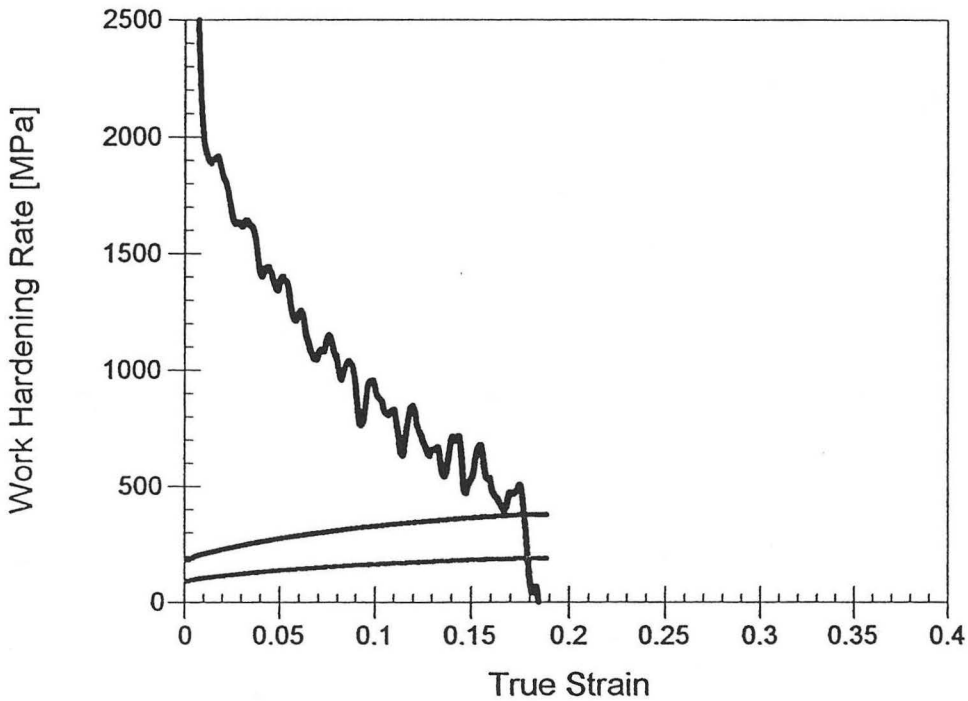

Figure 30: Plots of θ and $\frac{\sigma}{2}$ vs. ε for 6111-T4 narrow specimen tested at 300K: a) 10^{-4} /s.

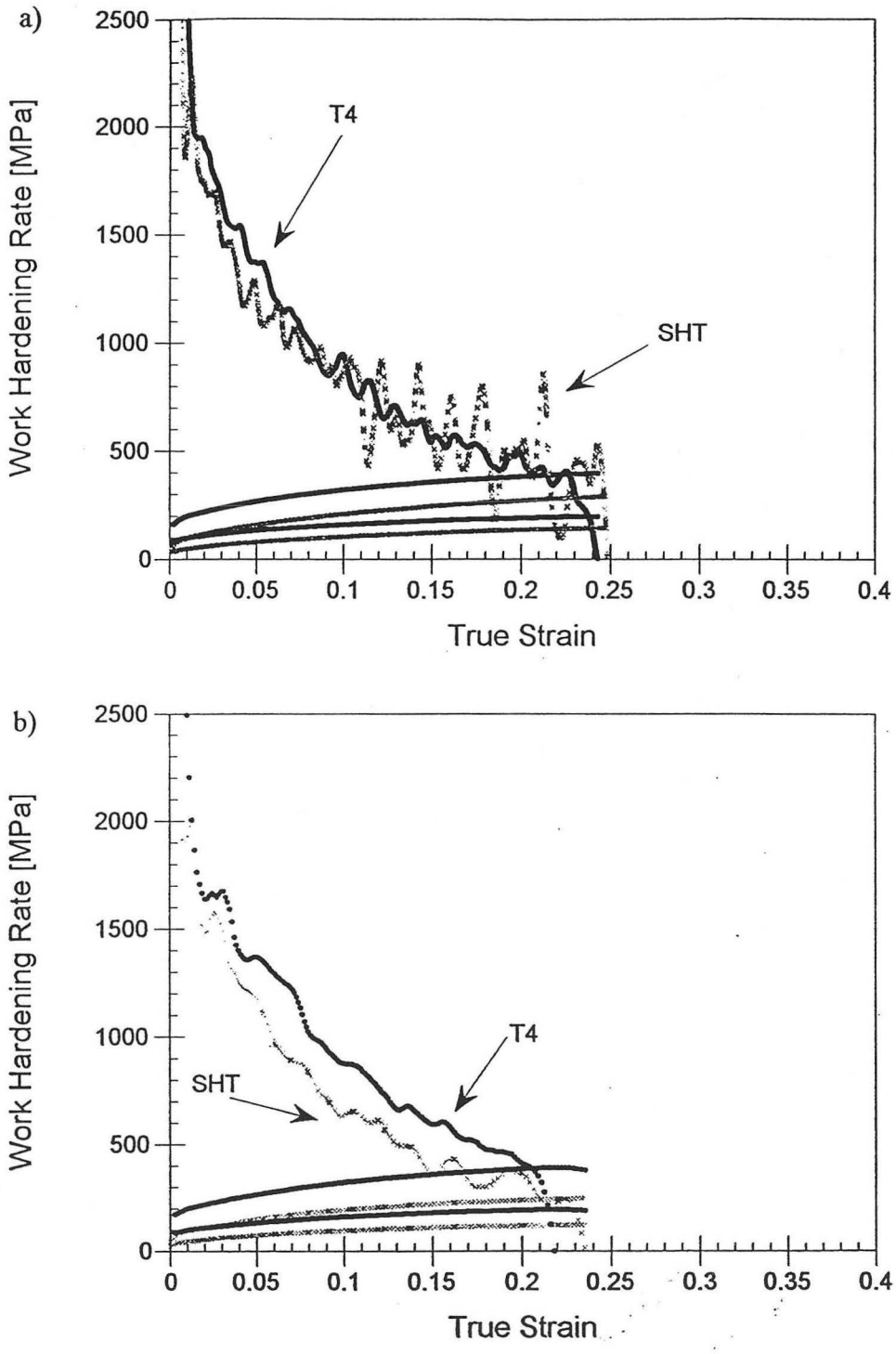

Figure 31: Plots of θ and $\frac{\sigma}{2}$ vs. ε for 6111 SHT and -T4 transverse specimens tested at 300K: a) 10^{-4} /s and b) 10^{-1} /s.

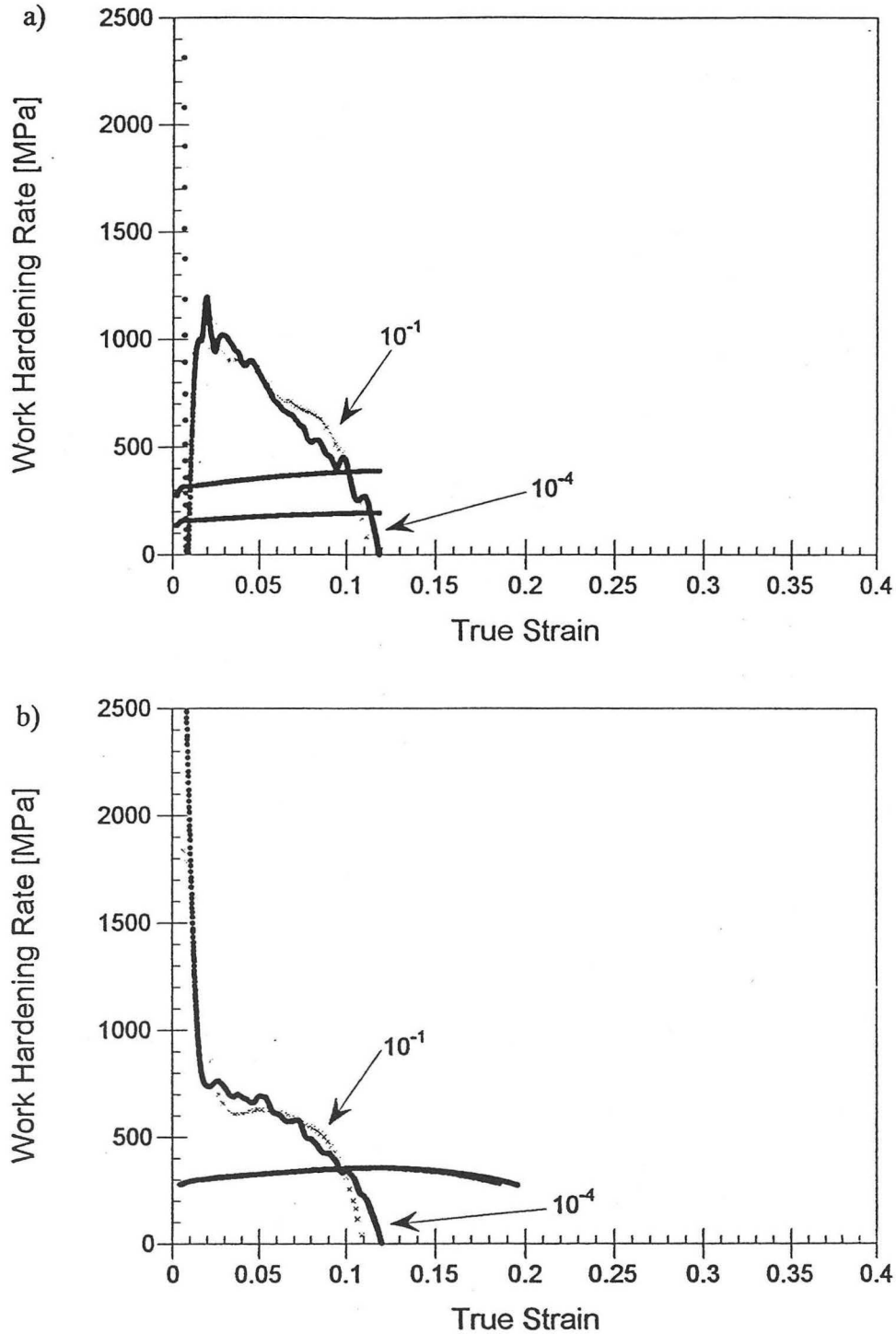

Figure 32: Plots of θ and $\frac{\sigma}{2}$ vs. ε for 6061-T6 specimens tested at 300K and strain rates of 10^{-4} /s and 10^{-1} /s: a) sheet and b) round cross-section specimens.

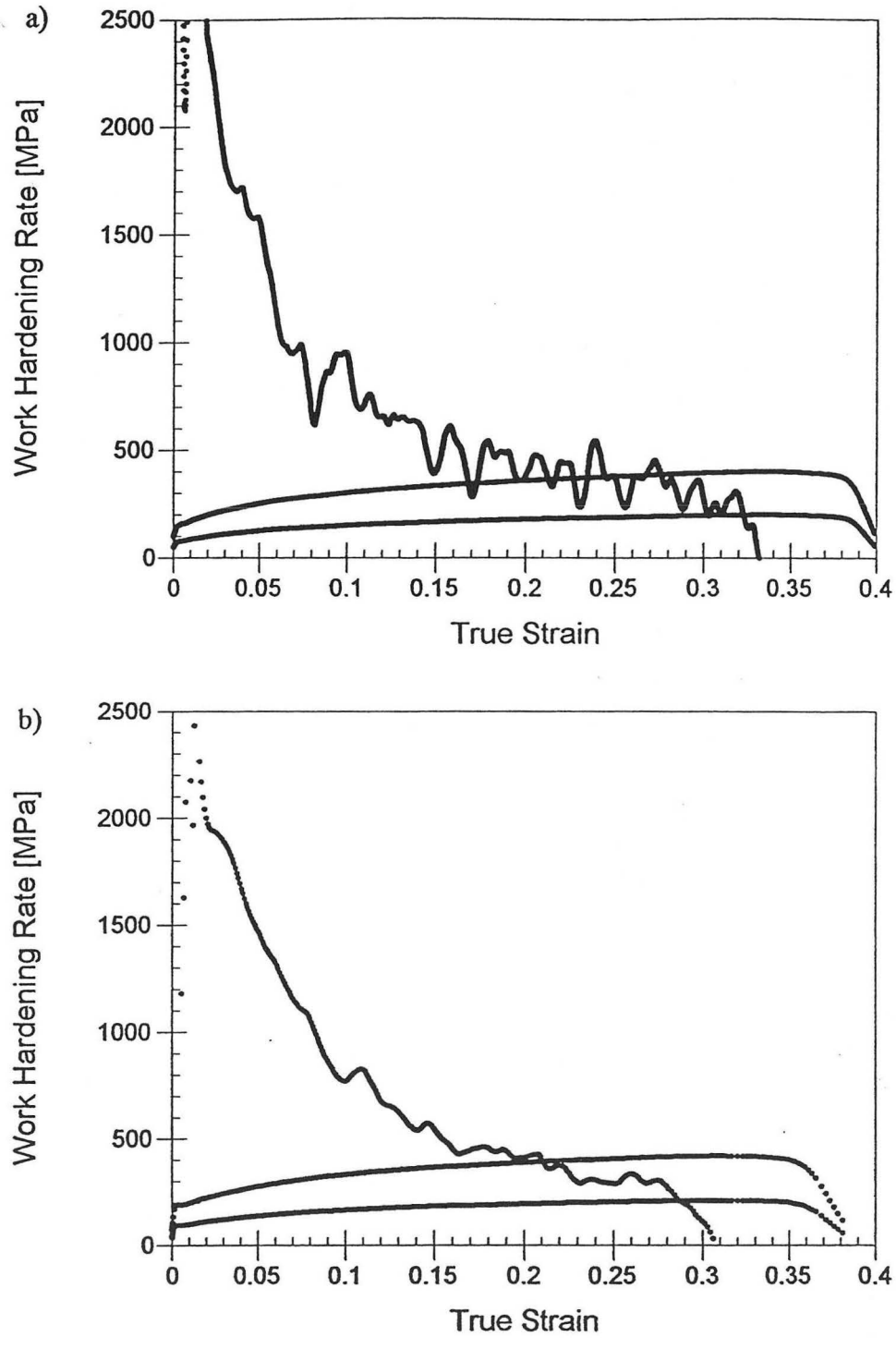

Figure 33: Plots of θ and $\frac{\sigma}{2}$ vs. ε for AKDQ steel at 300K and strain rates of a) 10^{-4} /s and b) 10^{-1} /s.

a)

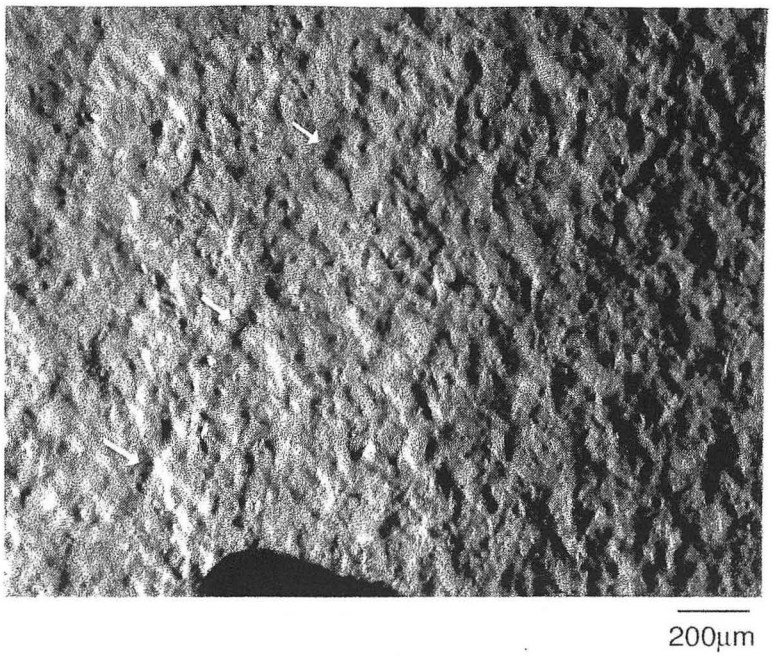

b)

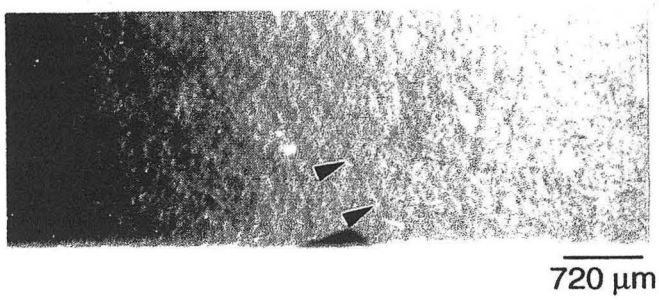

Figure 34: Optical micrographs of areas of local deformation (arrows) that have formed on a sample that was polished and strained to 1% plastic strain. a) Higher magnification and b) lower magnification (photo is inverted from a)). The local deformation areas are approximately 40 μm wide and range from 400-800 μm long.

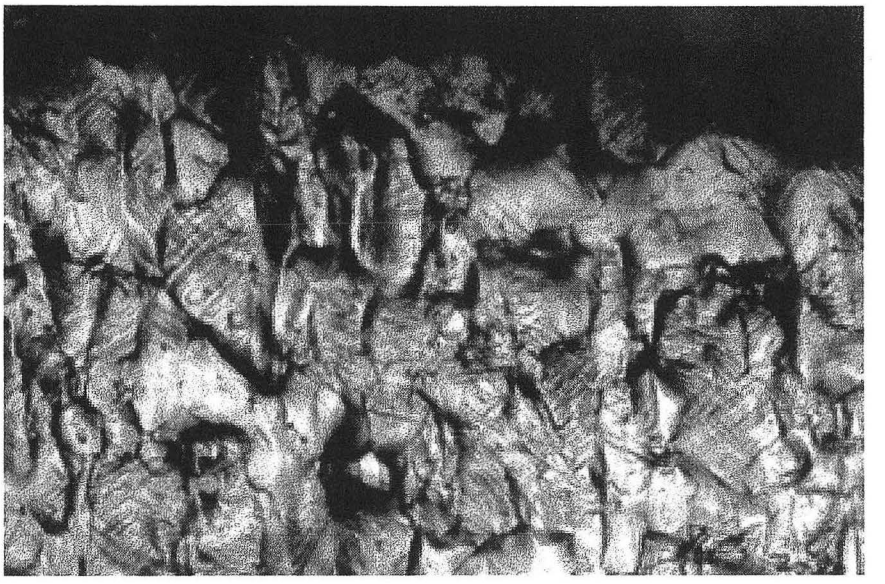

100 μm

Figure 35: Optical micrograph of 6111-T4 (4.2K, 10^{-4} /s) specimen surface. Fracture surface is at the top of the micrograph. Intense slip occurs in some grains but not in others.

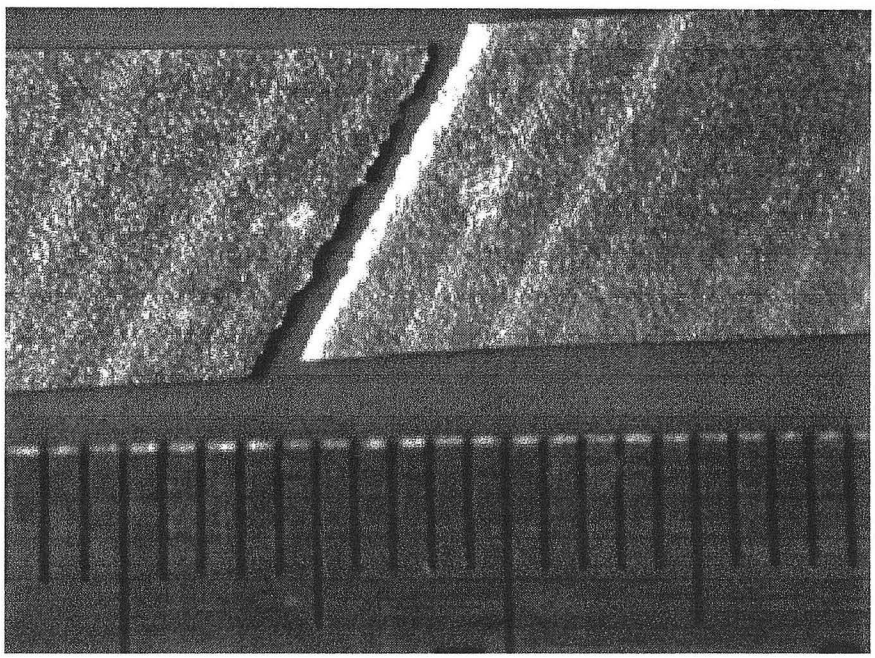

Figure 36: Optical micrograph of 6111-T4 (4.2K, 10^{-4} /s) specimen surface. Several deformation bands are visible. Each division on the scale is 1 mm.

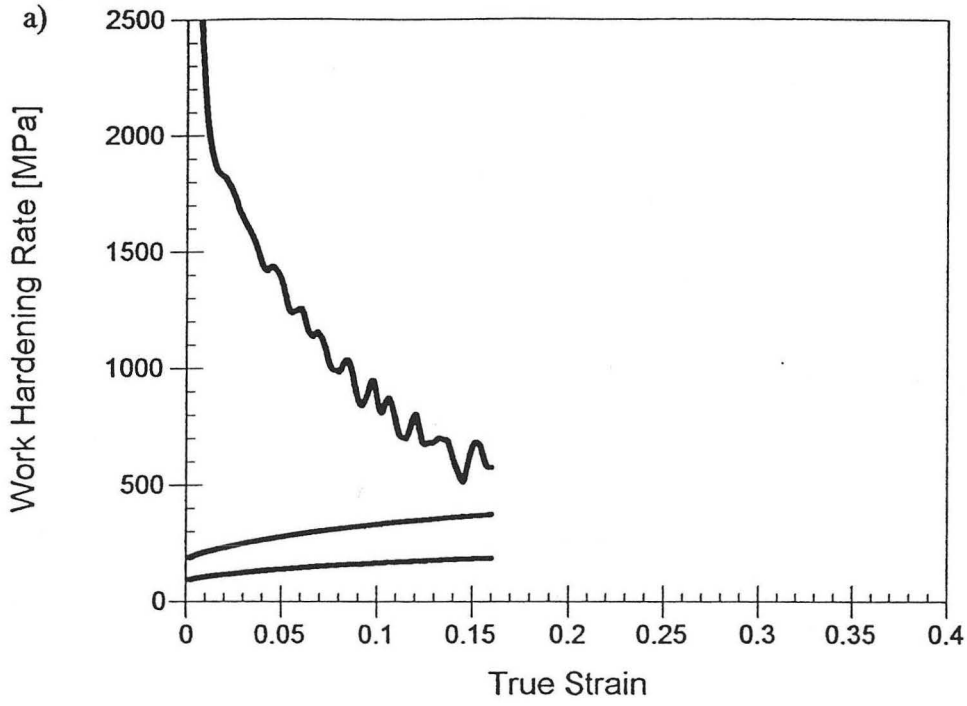

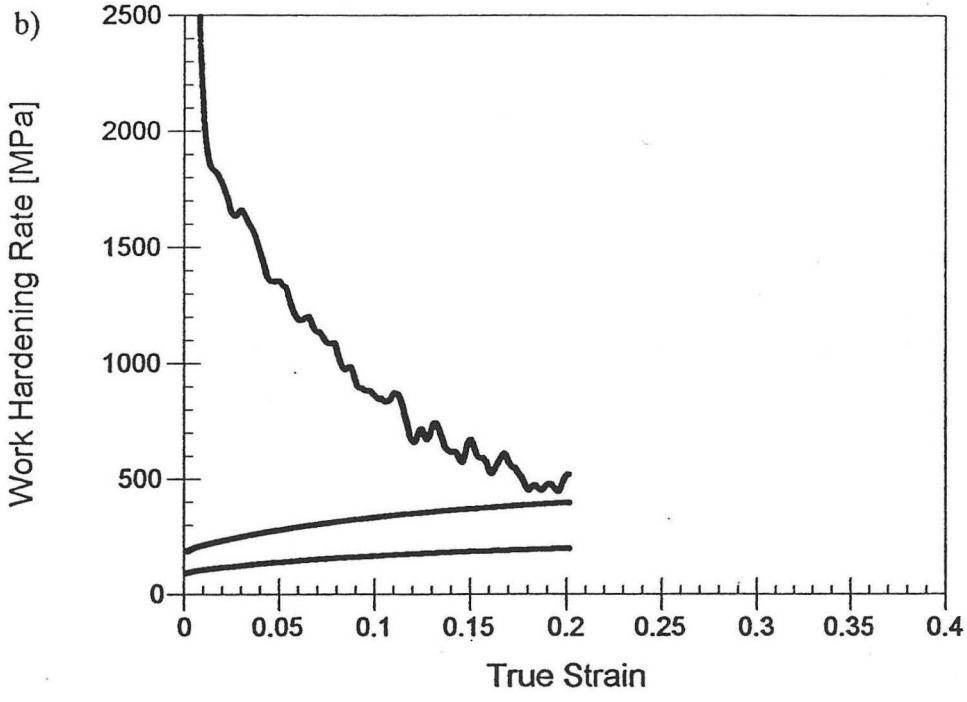

Figure 37: Plots of θ and $\frac{\sigma}{2}$ vs. ε for 6111-T4 (300K and 10^{-4} /s) specimens used for measuring width and thickness changes: a) BDN1 and b) BDN2.

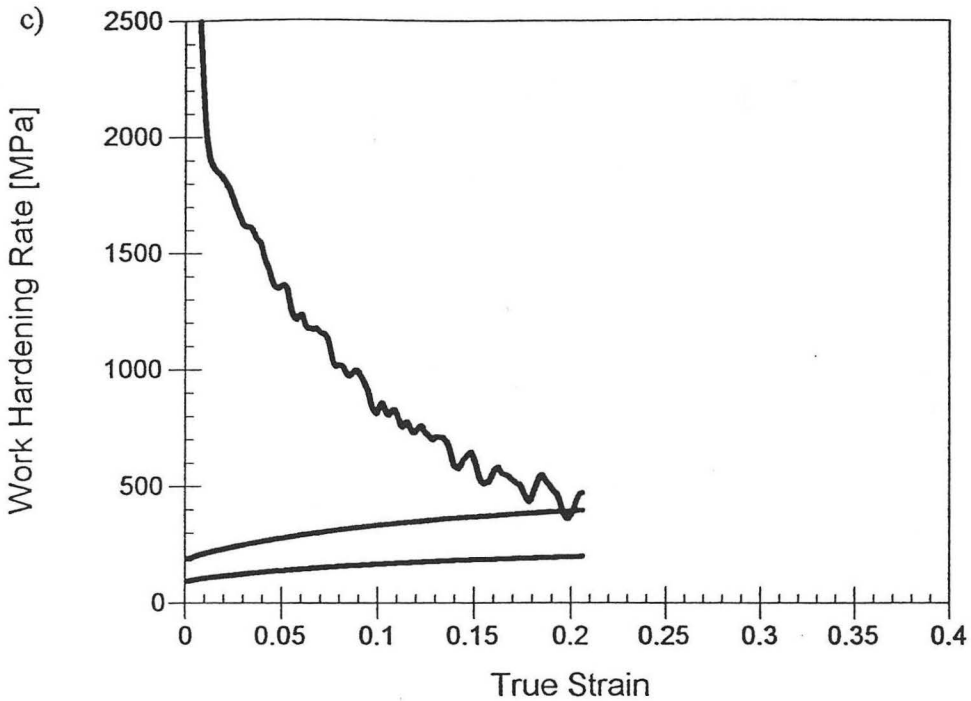

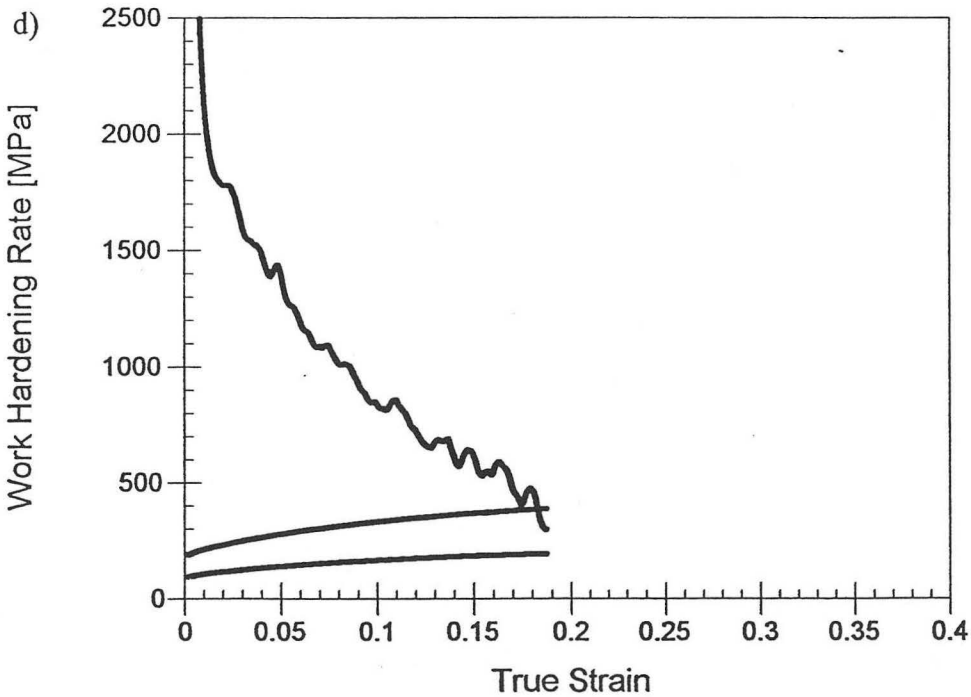

Figure 37: Plots of θ and $\frac{\sigma}{2}$ vs. ε for 6111-T4 (300K and 10^{-4} /s) specimens used for measuring width and thickness changes: c) BDN3 and d) DN1.

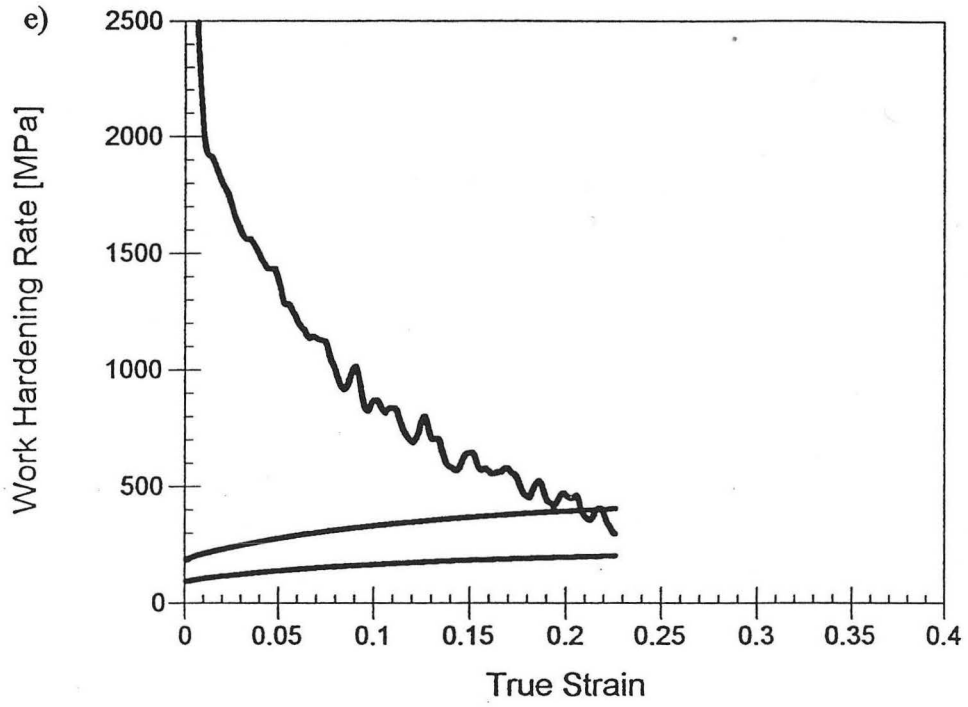

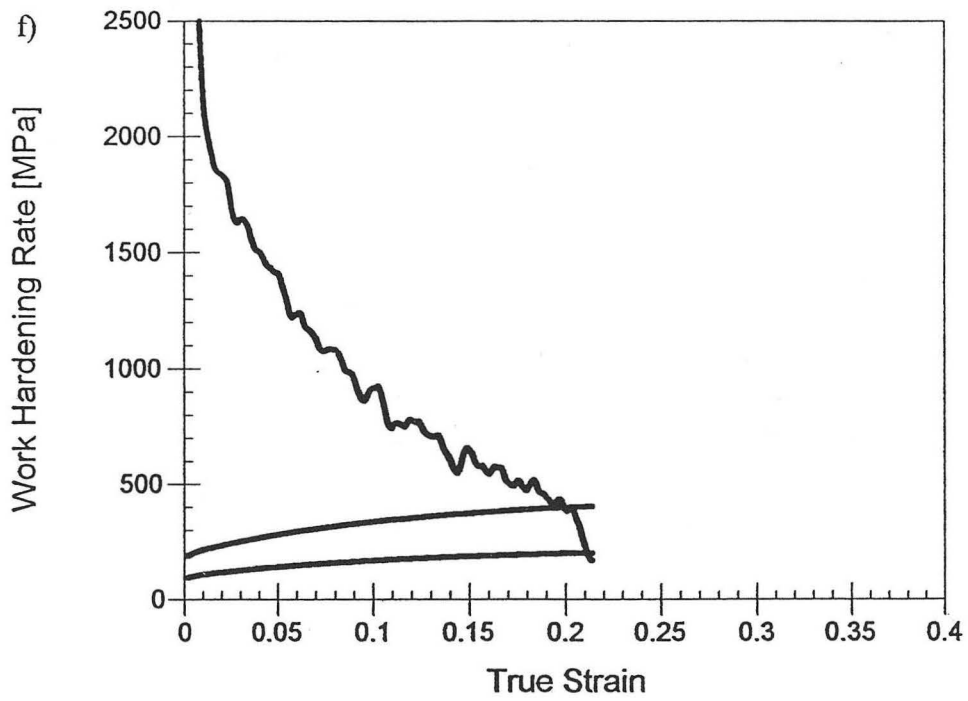

Figure 37: Plots of θ and $\frac{\sigma}{2}$ vs. ε for 6111-T4 (300K and 10^{-4} /s) specimens used for measuring width and thickness changes: e) DN2 and f) LN.

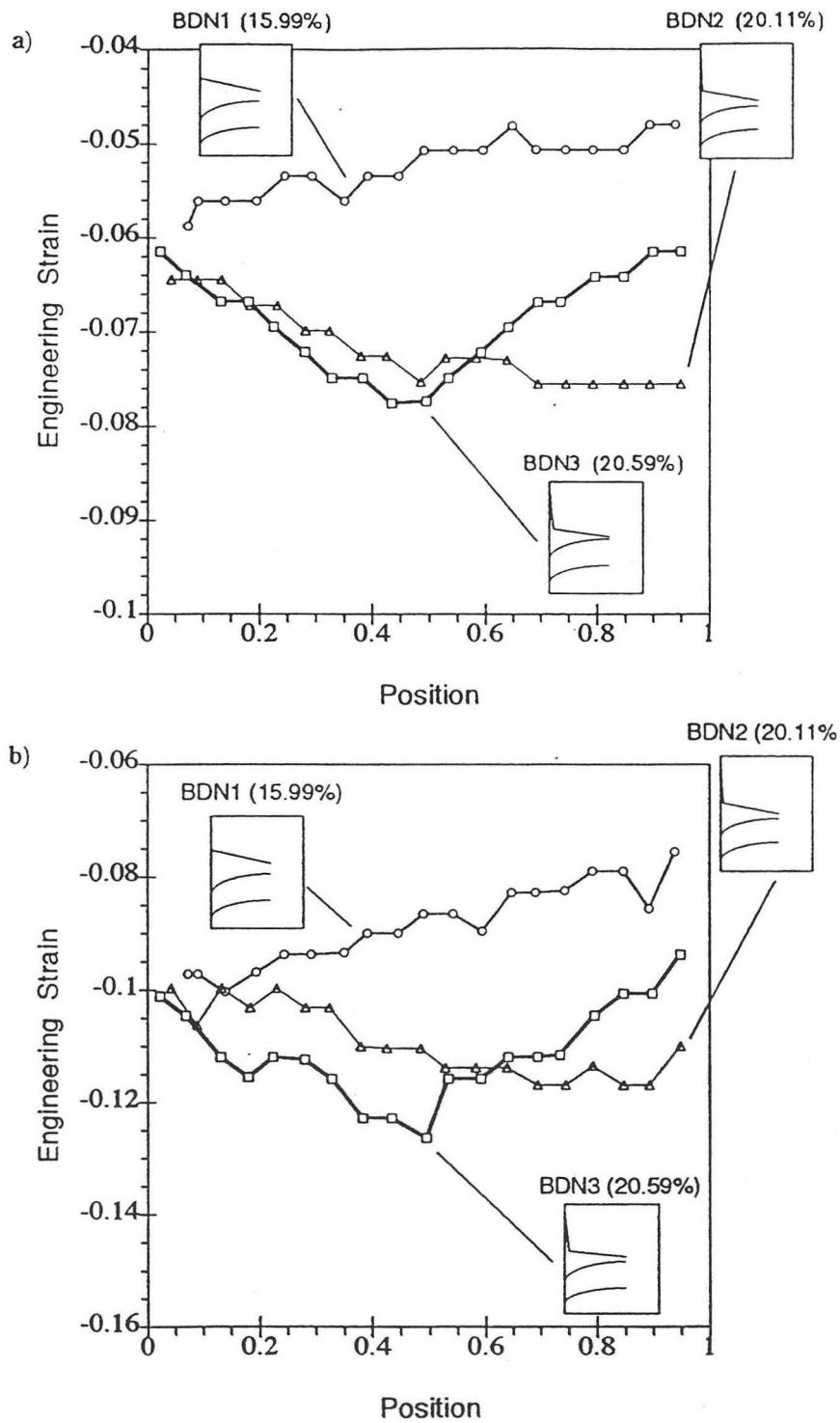

Figure 38: Engineering strain vs. position in the gage section for BDN1, BDN2 and BDN3 in the a) width and b) thickness directions.

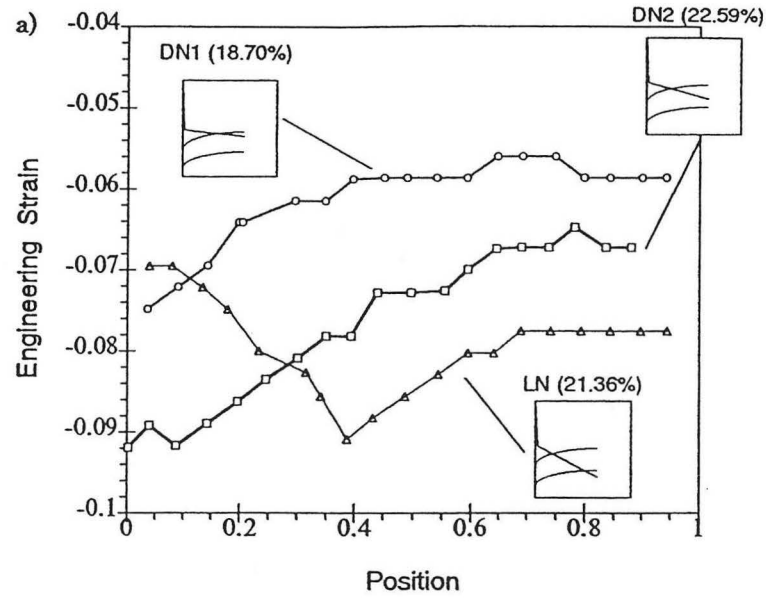

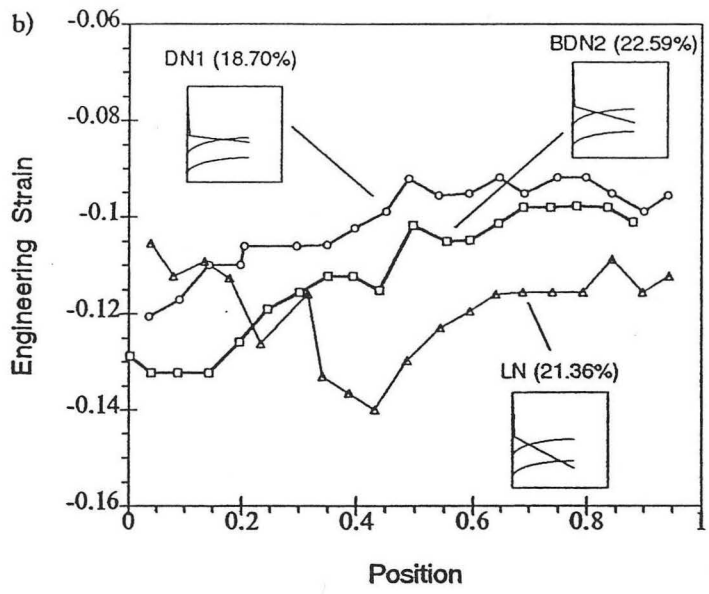

Figure 39: Engineering strain vs. position in the gage section for DN1, DN2 and LN in the a) width and b) thickness directions.

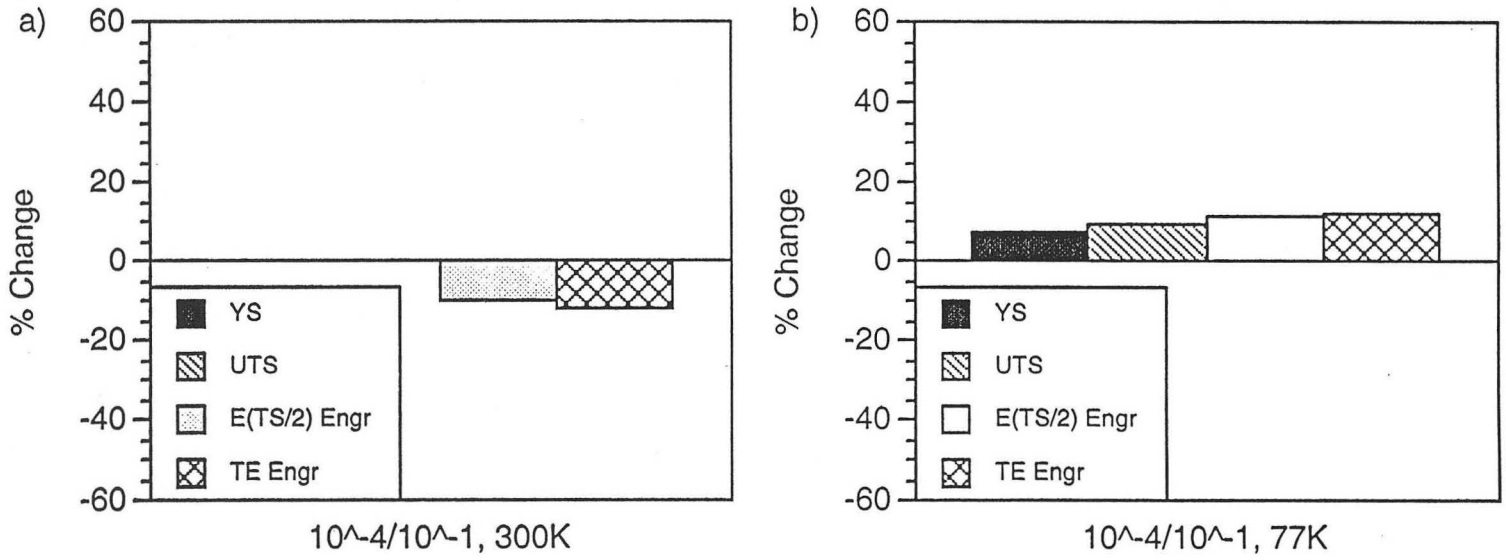

Figure 40: Percent change in mechanical properties for 6111-T4 longitudinal samples when increasing the strain rate from 10^{-4} /s to 10^{-1} /s at a) 300K and b) 77K.

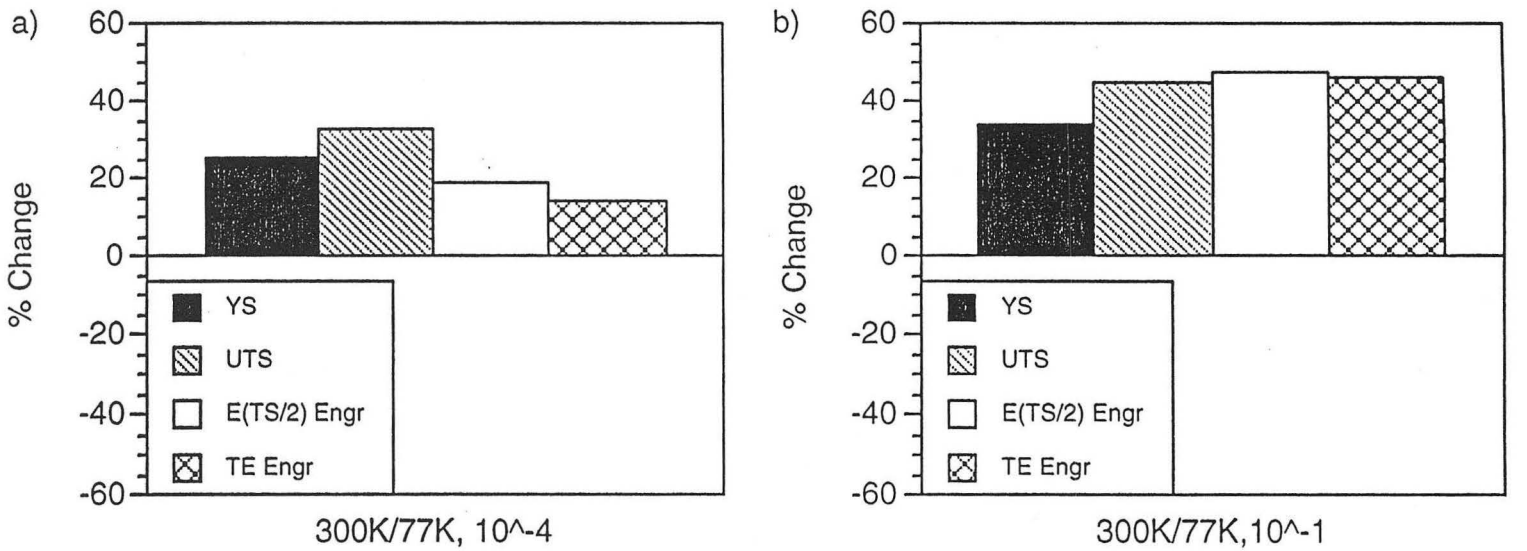

Figure 41: Percent change in mechanical properties for 6111-T4 longitudinal samples when decreasing the test temperature from 300K to 77K at a constant strain rate of a) 10^{-4} /s and b) 10^{-1} /s.

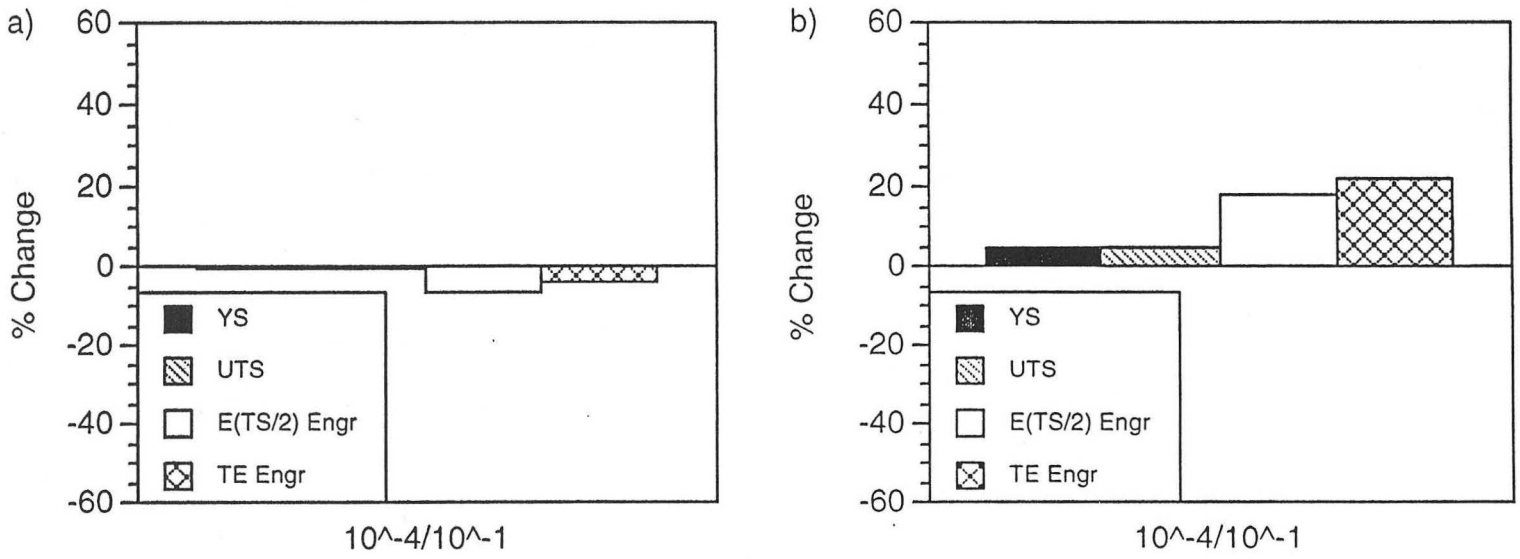

Figure 42: Percent change in mechanical properties for 6111-T4 transverse samples when increasing the strain rate from 10^{-4} /s to 10^{-1} /s at a) 300K and b) 77K.

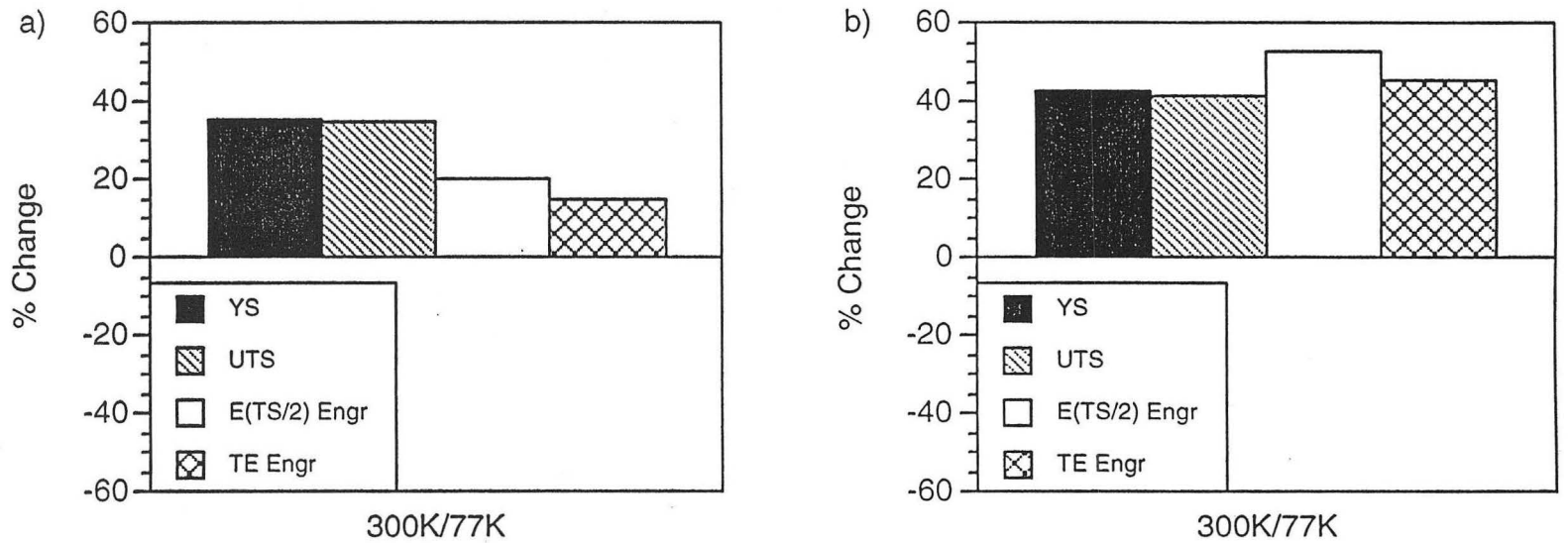

Figure 43: Percent change in mechanical properties for 6111-T4 transverse samples when the test temperature decreases from 300K to 77K at a) 10^{-4} /s and b) 10^{-1} /s.

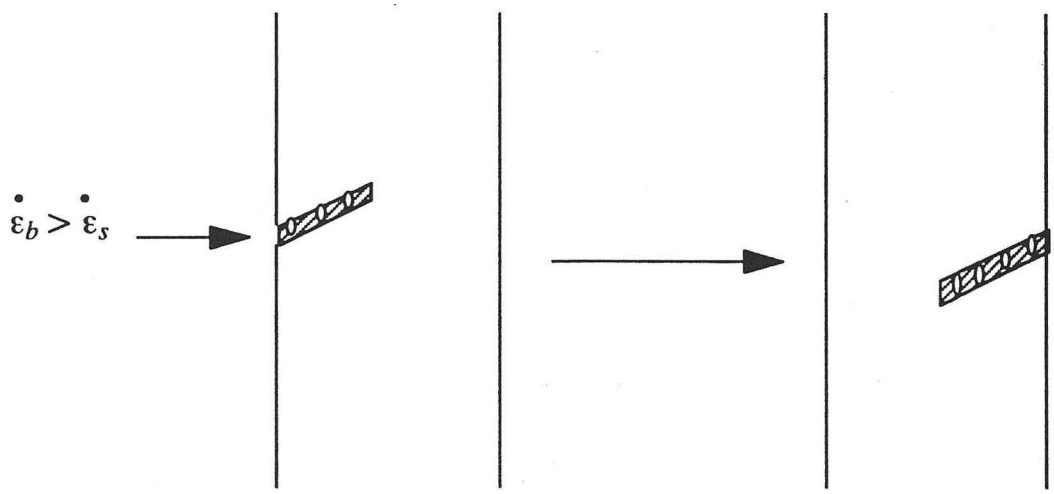

Figure 44: Schematic of how low strain rate sensitivity can cause deformation to localize in the next weakest area. The next weakest area is due to void growth.

a)

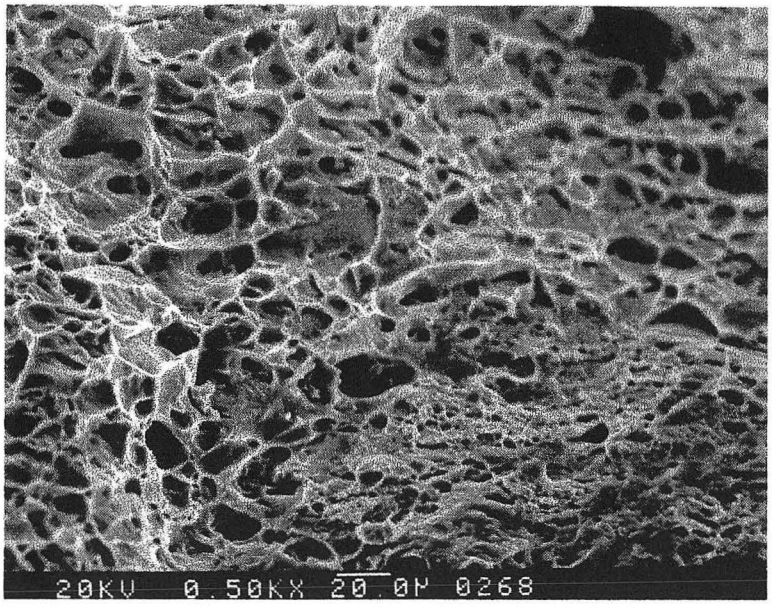

b)

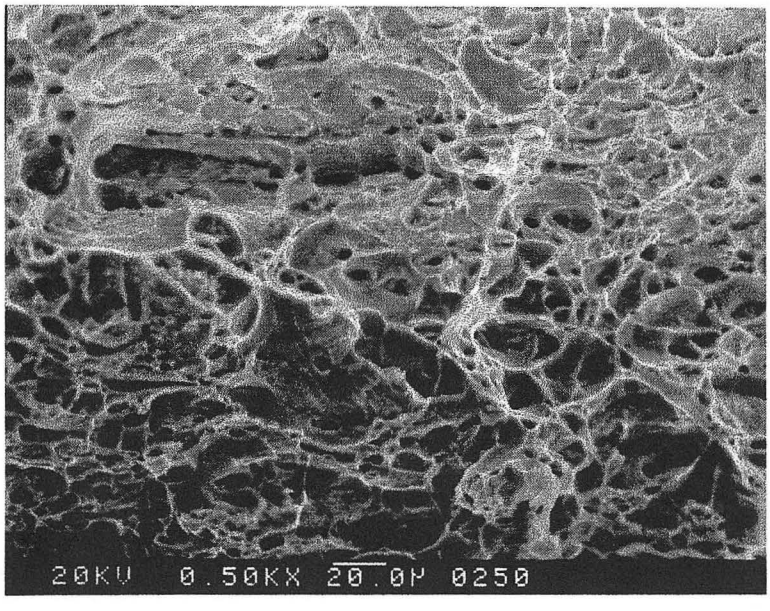

Figure 45: SEM micrographs of the fracture surfaces for 6111-T4 samples (300K and 10^{-4} /s) which displayed a) unstable and b) stable deformation behavior.

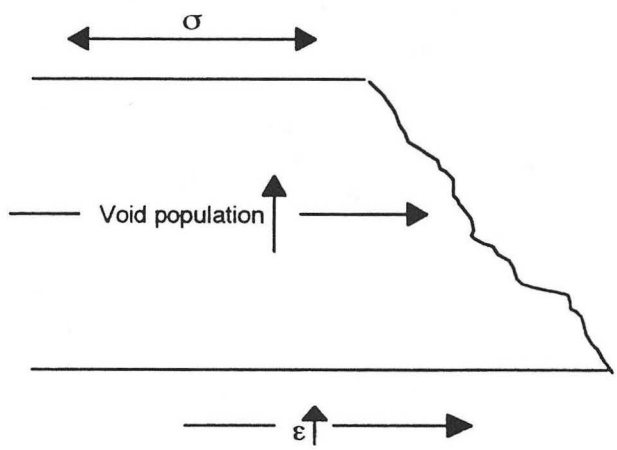

Figure 46: Schematic of the strain gradient in the LT plane of the fractured tensile specimen. The gradient increases from left to right, as the fracture surface is approached. The void population increases from left to right, as the strain gradient increases.

a)

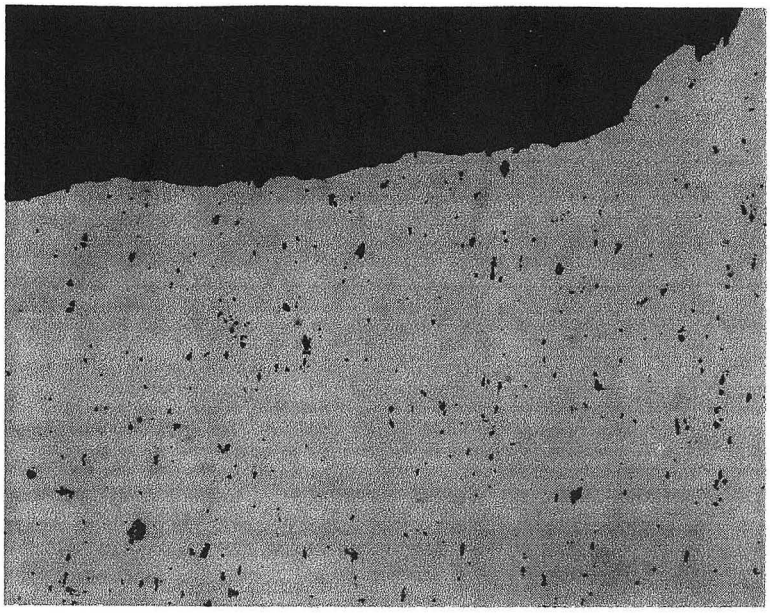

100 μm

b)

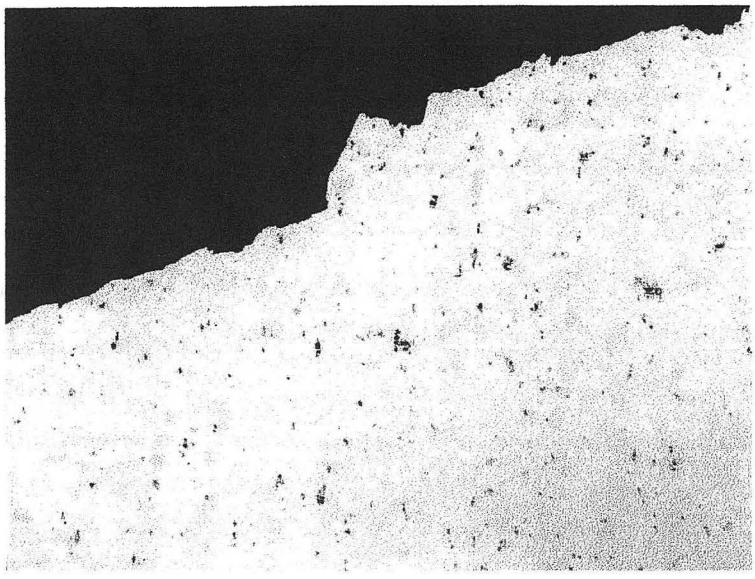

100 μm

Figure 47: Optical micrographs of the region near the fracture surface (top of micrographs) for the a) stable deformation sample and b) unstable deformation sample at 300K and 10^{-4} /s. No obvious differences are seen in their void distributions.

a)

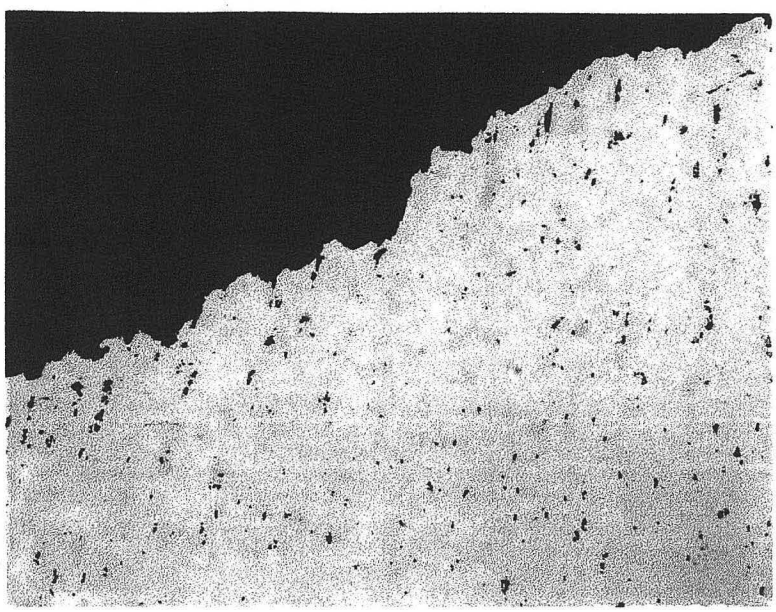

100 μm

b)

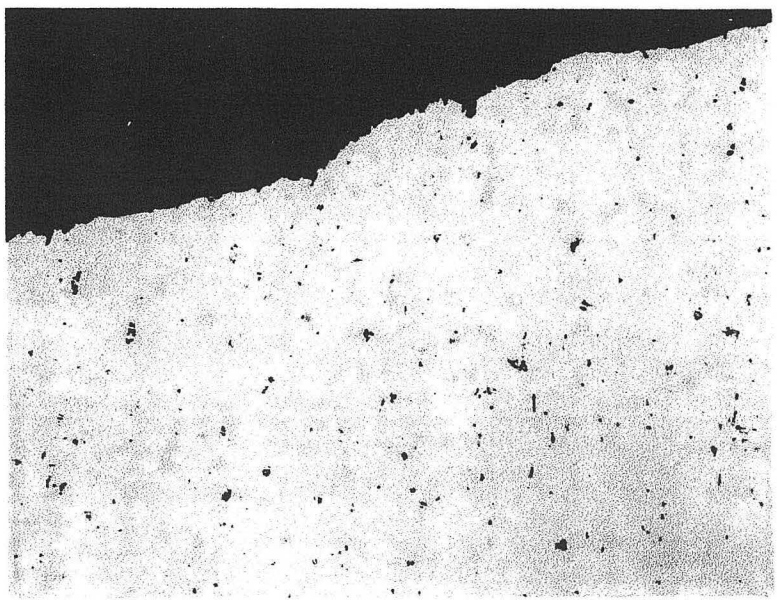

100 μm

Figure 48: Optical micrographs of typical fracture surfaces for both stable and unstable samples (300K and 10^{-4} /s). The fracture surface has regions that have a) a jagged appearance and b) a flat fracture surface.

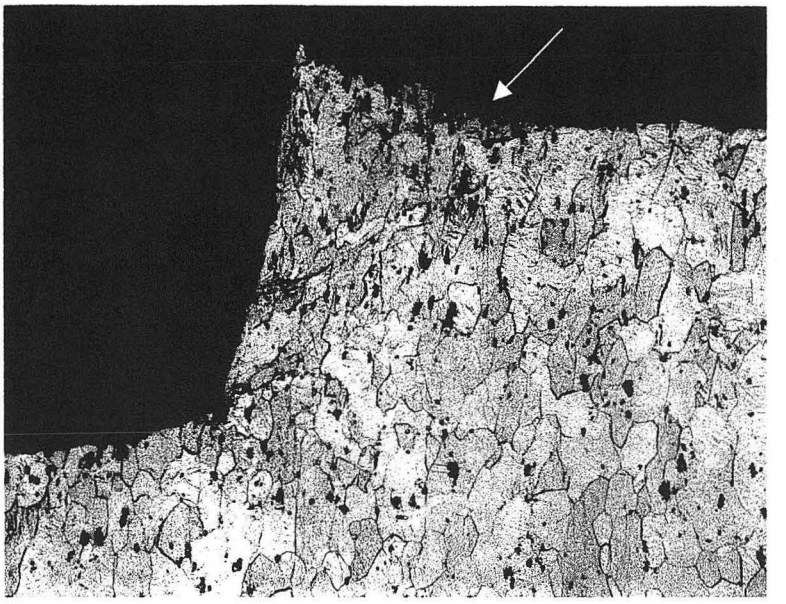

100 μm

Figure 49: Optical micrographs of the etched fracture surface (300K, 10^{-4} /s. Fracture occurs along grain boundaries as well as through grains. Fracture through grains of similar contrast can be seen at the arrow.

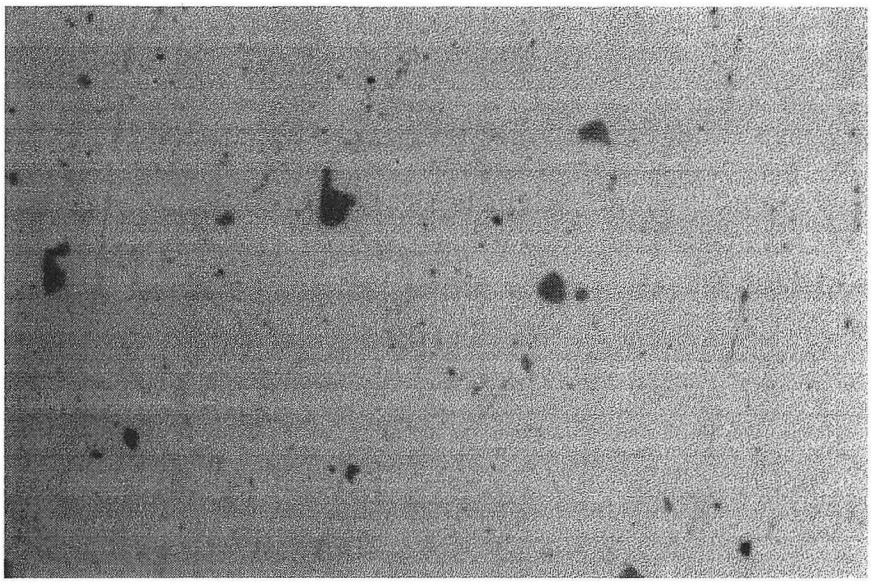

25 μm

Figure 50: Optical micrographs of the grip section of a prepolished tensile sample. No fractured particles are visible; therefore, the polishing procedure does not introduce fractured particles.

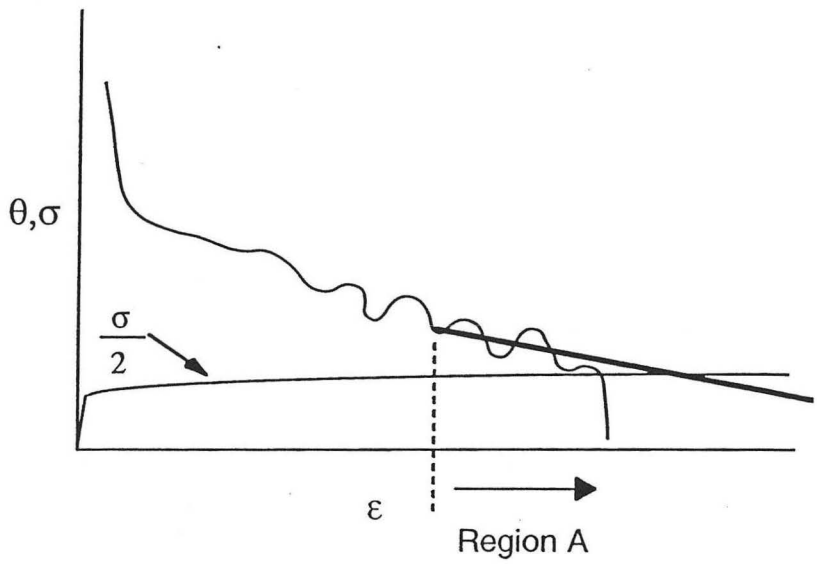

Figure 51: Schematic of a work hardening curve ($\theta, \frac{\sigma}{2}$ vs. ε). A line can be fitted to the latter region (region A).

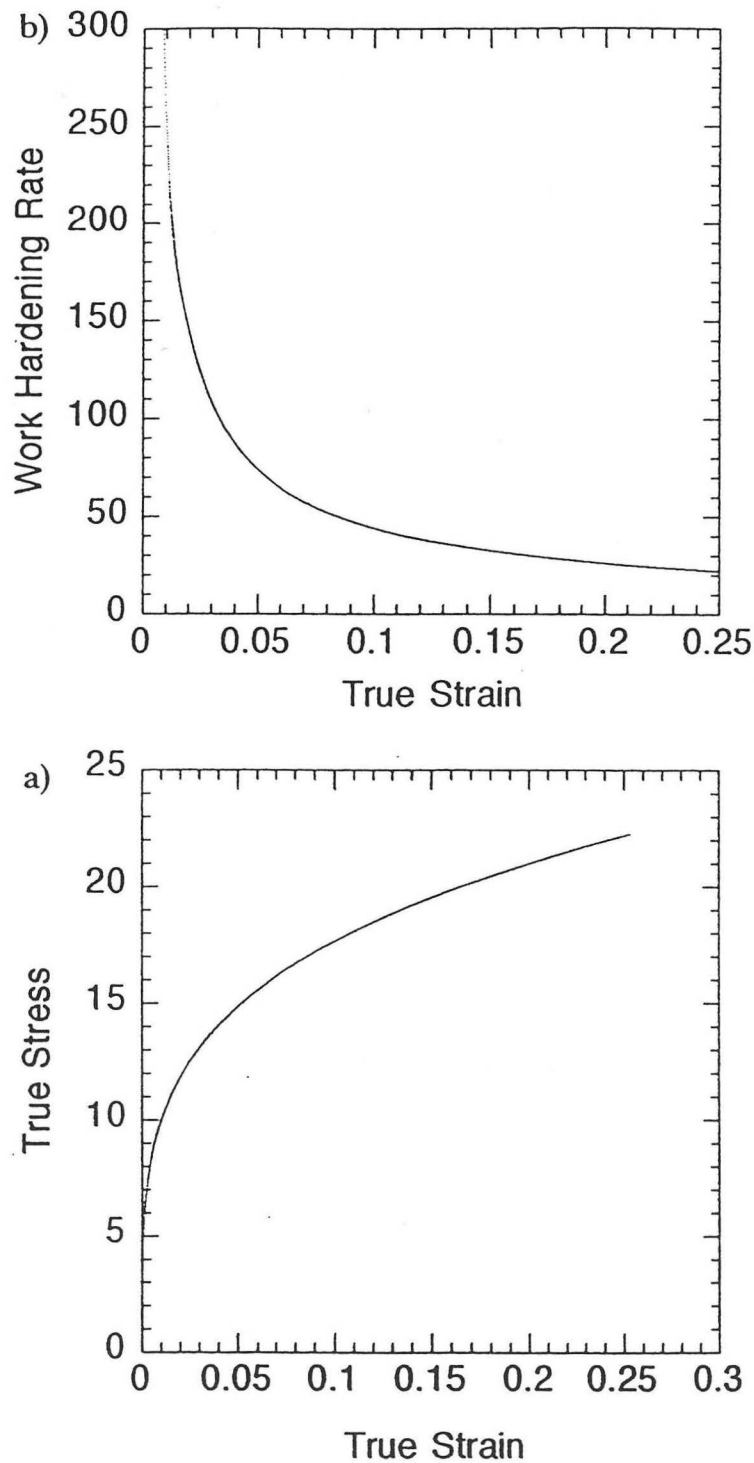

Figure 52: a) True stress-strain curve and b) work hardening curve of data generated by using the parabolic relationship $\sigma = K\varepsilon^{0.2}$. No oscillations are introduced during the data processing.

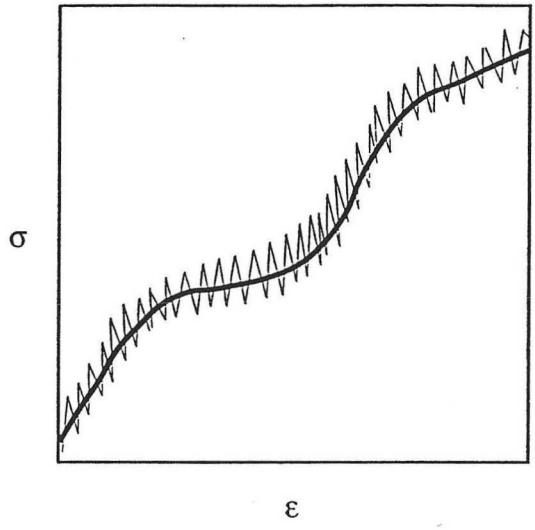

Figure 53: Schematic of how long wavelength oscillations (heavy line) often seen in stress-strain curves from the literature. These oscillations are observed in the stress-strain curve such as in figure 5 but have not been addressed. In materials that exhibit serrated flow, these oscillations occur simulataneously with the serrations (light line).

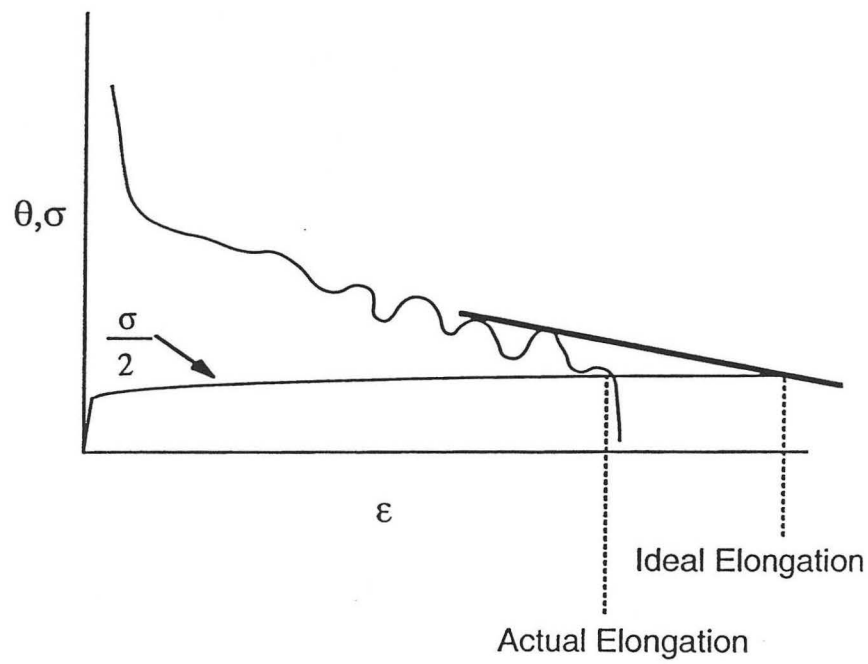

Figure 54: Schematic of obtaining an ideal elongation from the work hardening plot.

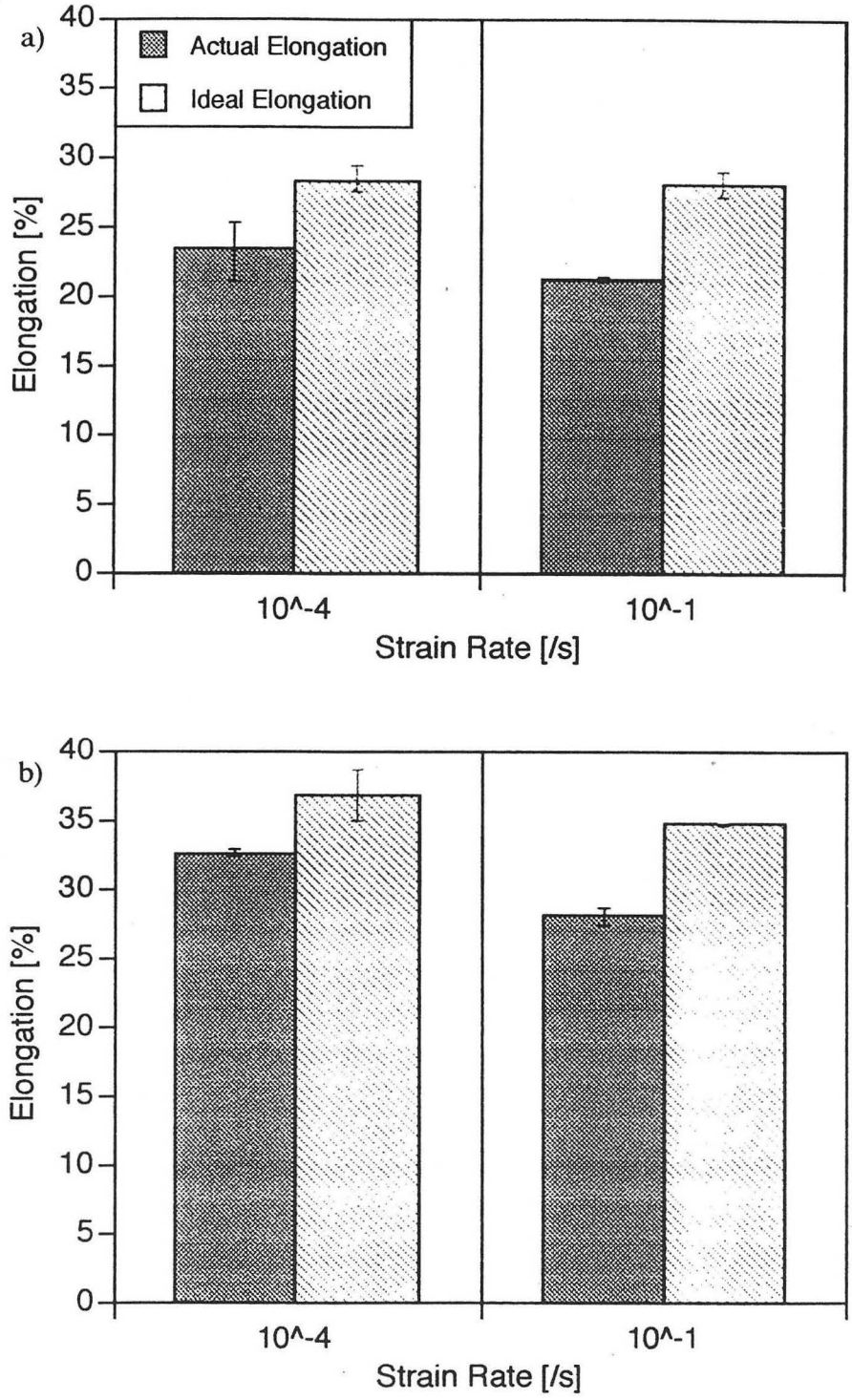

Figure 55: Actual and ideal elongations at 300K and at 10^{-4} /s and 10^{-1} /s for a) 6111-T4 and b) AKDQ steel.

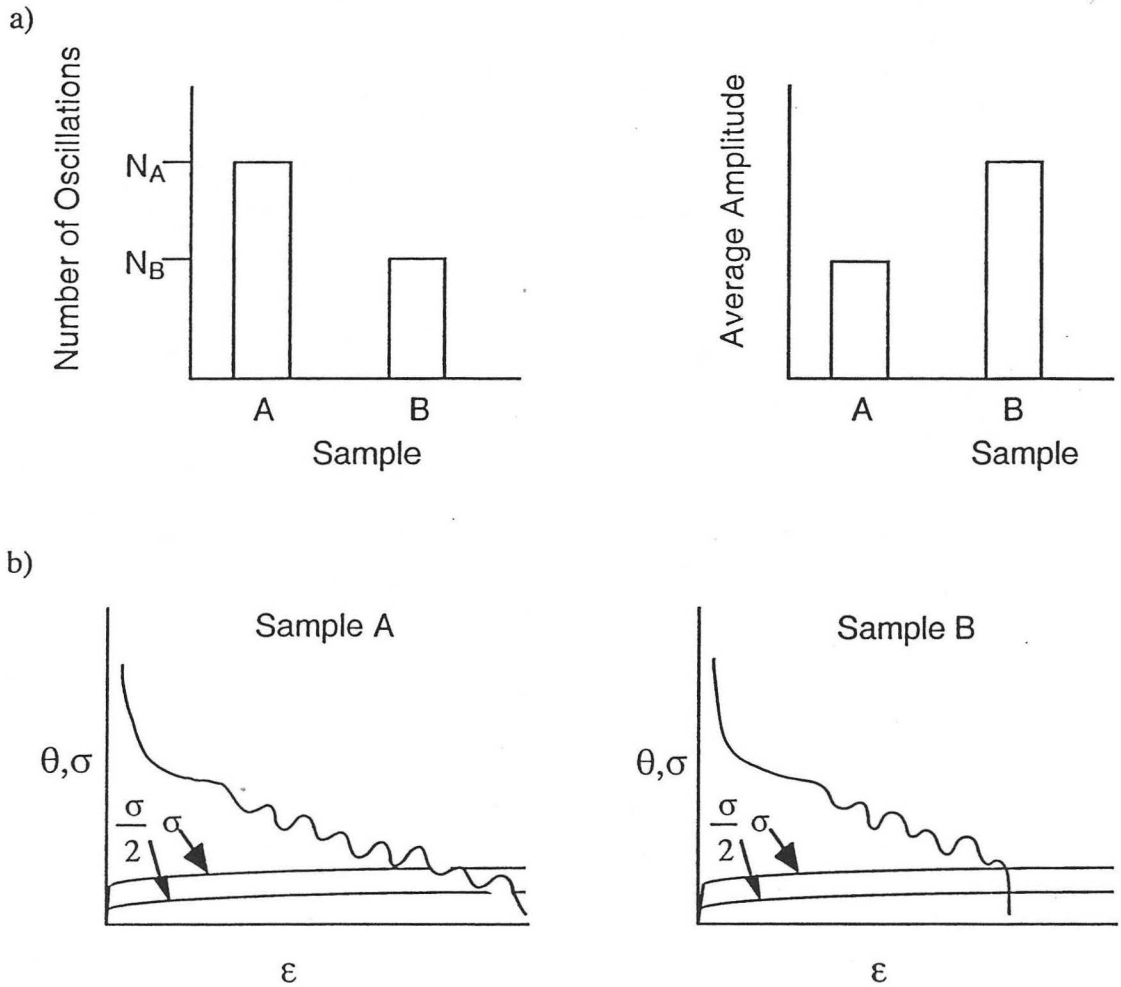

$$\varepsilon_{DL}^{A} > \varepsilon_{DL}^{B}$$
$$\varepsilon_{LF}^{A} > \varepsilon_{LF}^{B}$$

Figure 56: Schematic of how the number of oscillations, N, the average amplitude, A, the work hardening drop offs and the necking parameters behave for samples A and B. a) $N_A > N_B$; therefore, it would be expected that $A_A < A_B$, and b) their respective work hardening curves. Sample A has a more gradual drop off, and the necking parameters for A are greater as well.

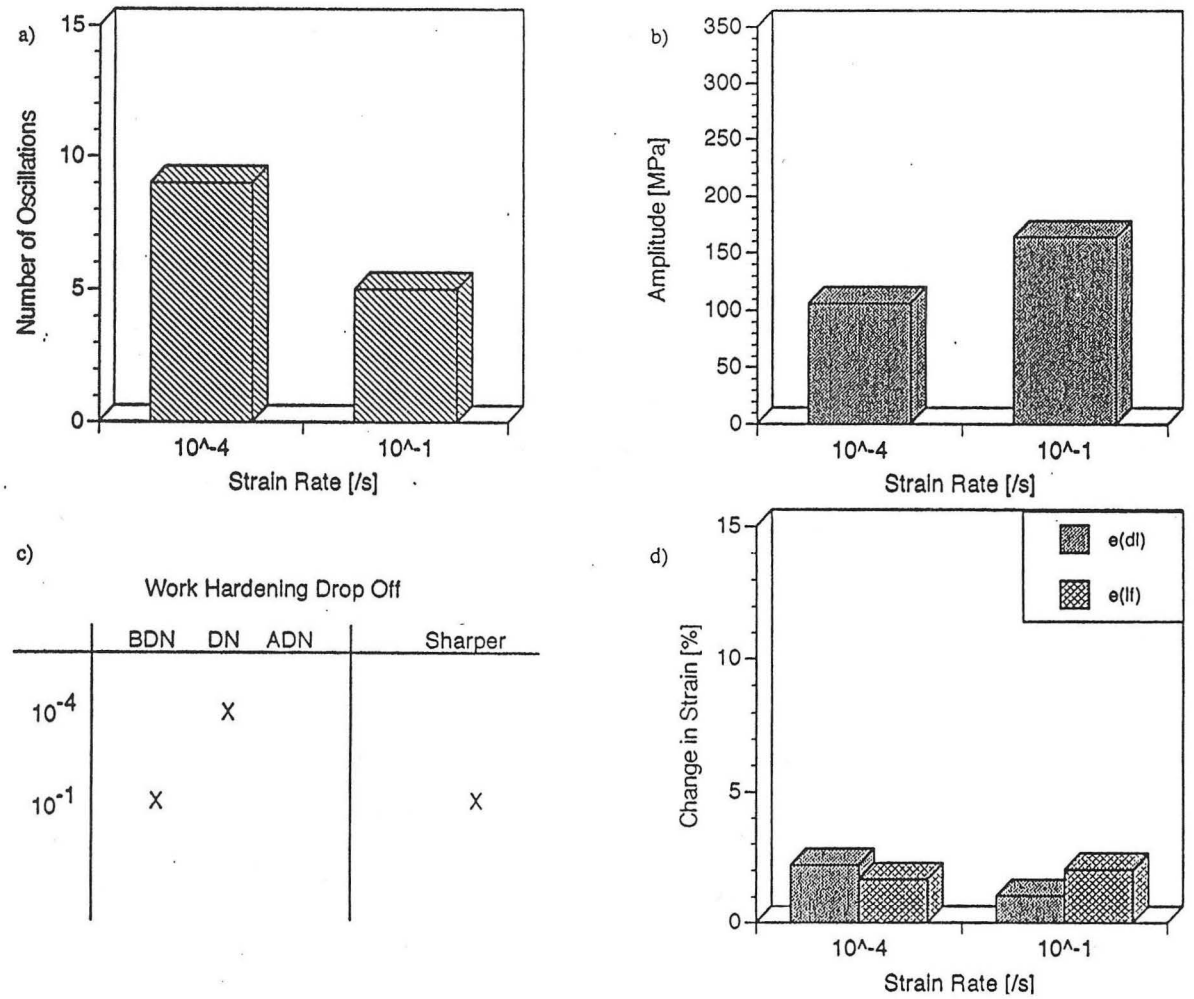

Figure 57: a) Number of oscillations, b) average amplitude, c) work hardening drop off characteristics and d) necking parameters for 6111-T4 longitudinal tested at 300K with an increase in strain rate from 10^{-4} /s to 10^{-1} /s.

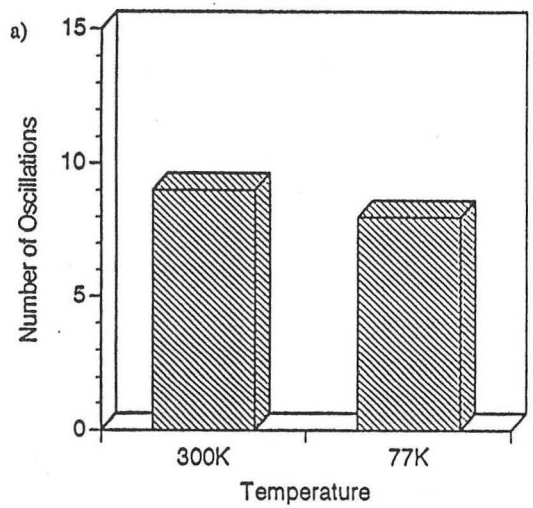

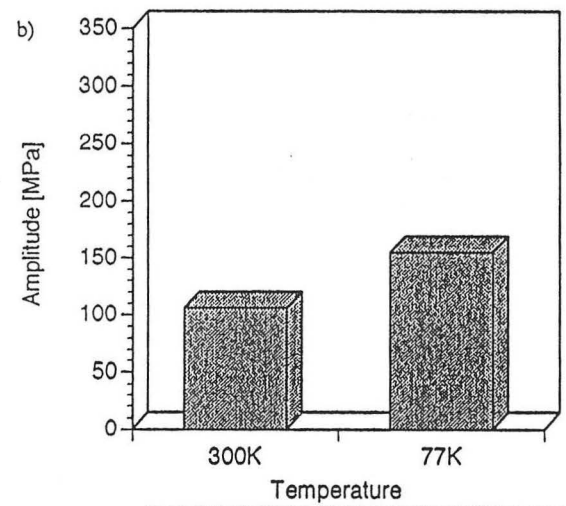

c)

Work Hardening Drop Off

	BDN	DN	ADN	Sharp
300K		X		X
77K	X			X

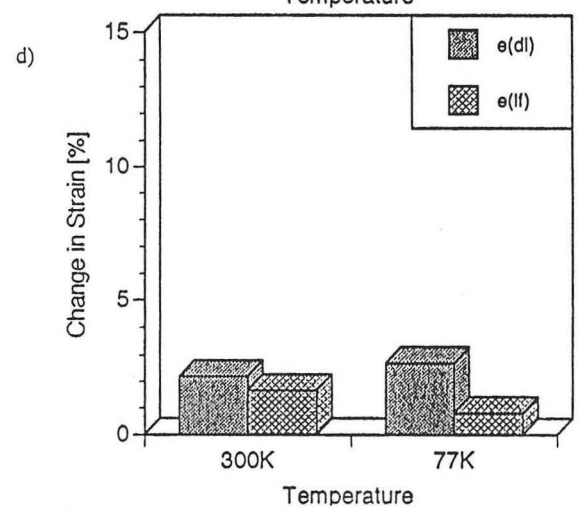

Figure 58: a) Number of oscillations, b) average amplitude, c) work hardening drop off characteristics and d) necking parameters for 6111-T4 longitudinal tested at 10^{-4} /s with a decrease in temperature from 300K to 77K.

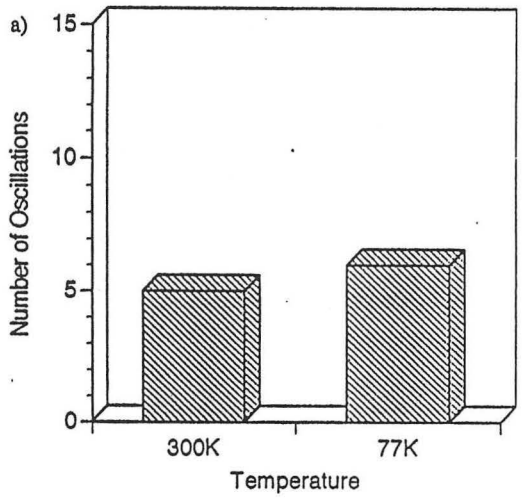

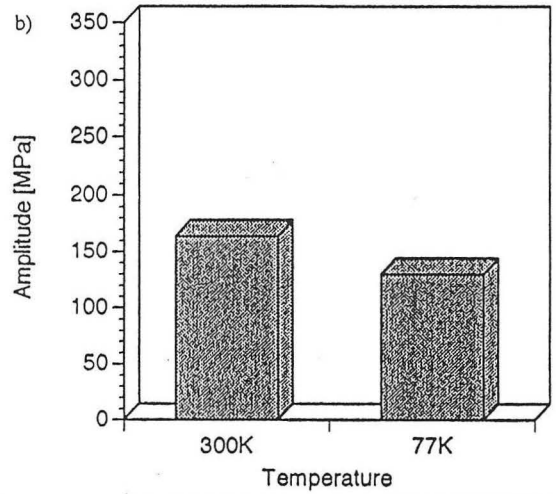

c)

Work Hardening Drop Off

	BDN	DN	ADN	Sharper
300K	X			X
77K		X		

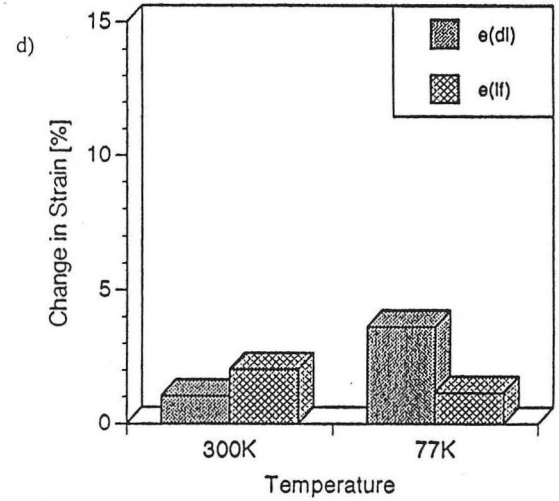

Figure 59: a) Number of oscillations, b) average amplitude, c) work hardening drop off characteristics and d) necking parameters for 6111-T4 longitudinal tested at 10^{-1} /s with a decrease in temperature from 300K to 77K.

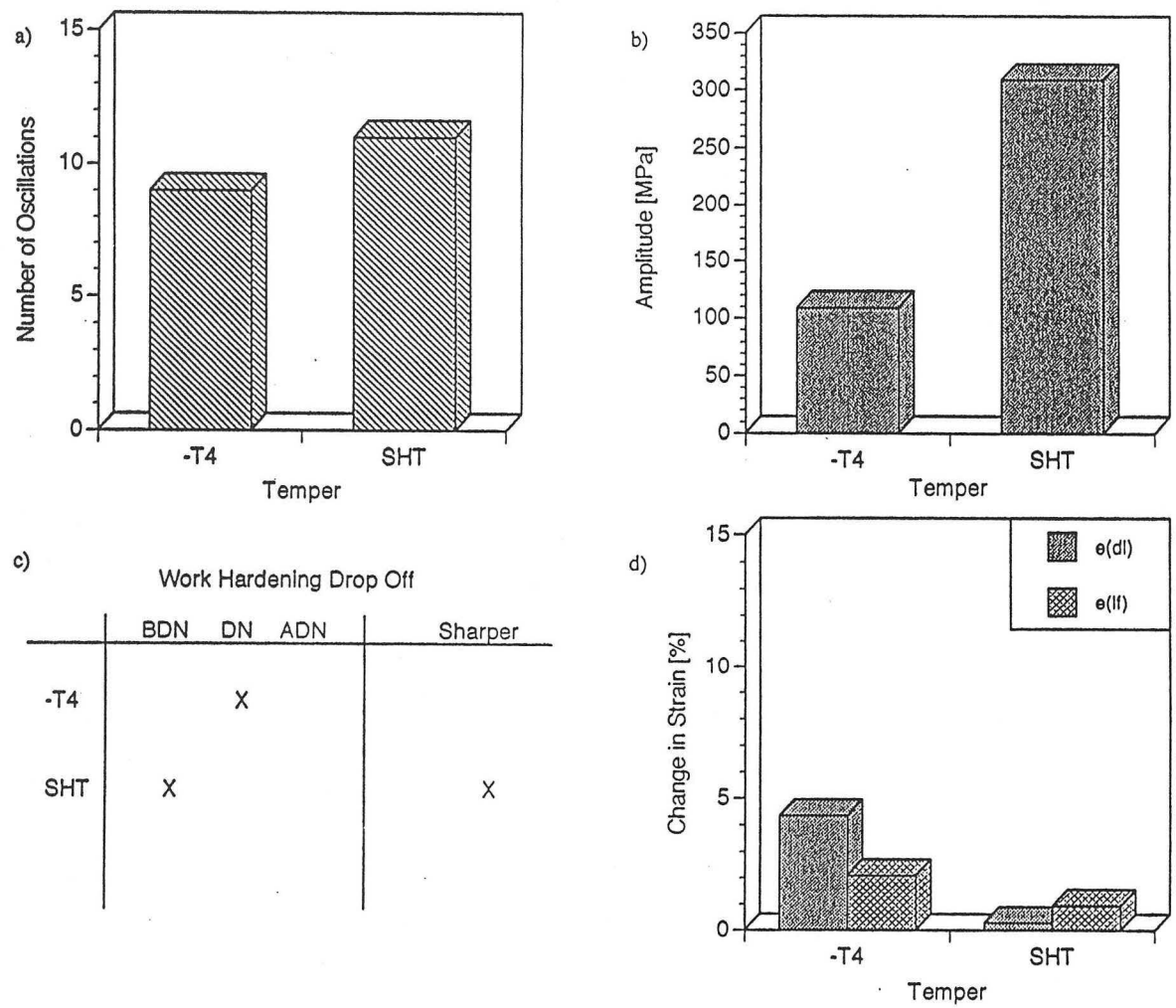

Figure 60: a) Number of oscillations, b) average amplitude, c) work hardening drop off characteristics and d) necking parameters for 6111 tested at 10^{-4} /s when the -T4 samples are solution heat treated (SHT).

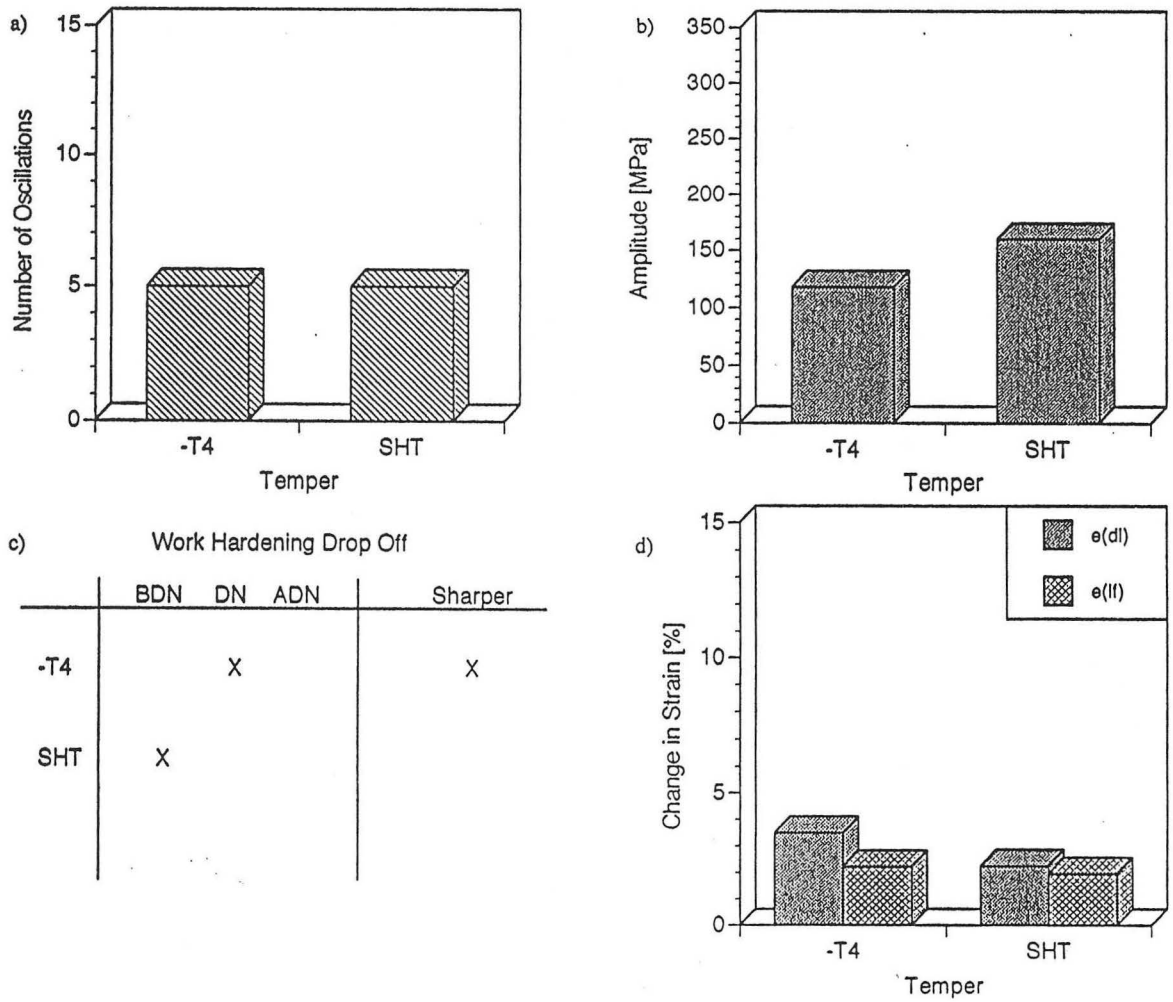

Figure 61: a) Number of oscillations, b) average amplitude, c) work hardening drop off characteristics and d) necking parameters for 6111 tested at 10^{-1} /s when the -T4 samples are solution heat treated (SHT).

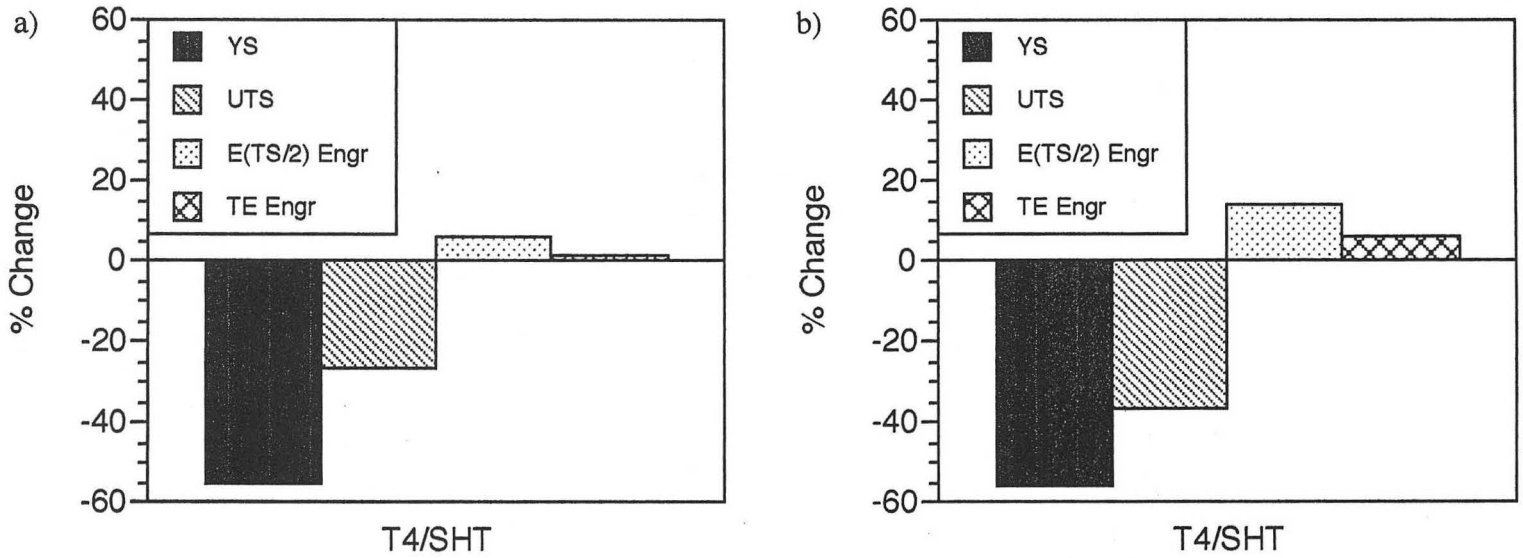

Figure 62: Percent change in mechanical properties for 6111 when the -T4 samples are solution heat treated (SHT) at 300K and a strain rate of a) 10^{-4} /s and b) 10^{-1} /s.

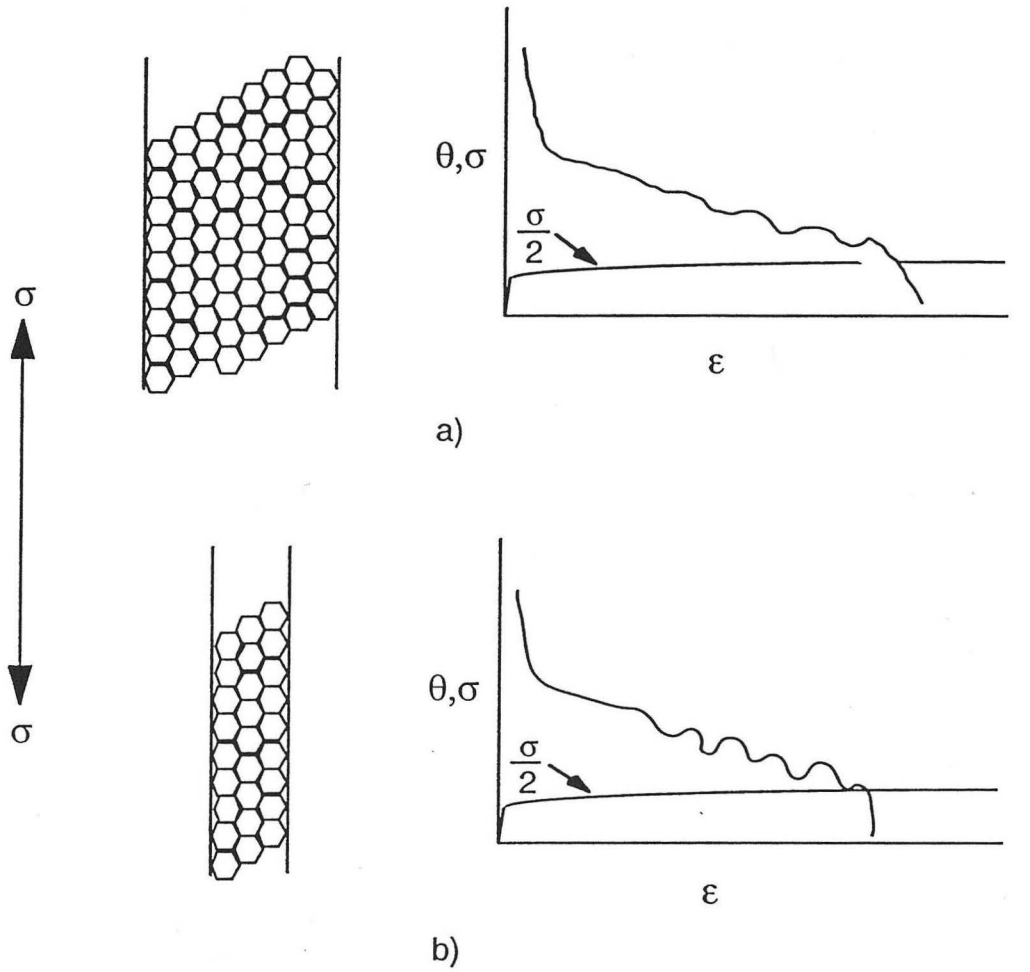

Figure 63: Schematic of how varying the gage width will affect the work hardening behavior. Clusters in a a) wide sample will account for a smaller volume fraction of the gage area while these clusters will constitute a larger volume fraction in the gage area of a narrow sample in b). The work hardening curve for the wide sample will have smaller amplitude oscillations than those for a narrow sample.

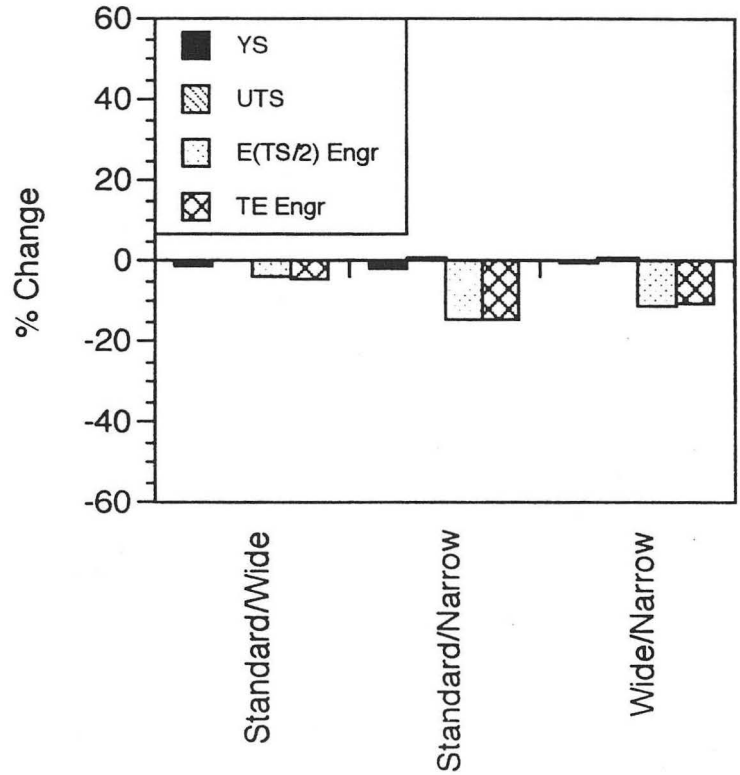

Figure 64: Percent change in mechanical properties for 6111-T4 longitudinal samples at 300K and 10^{-4} /s with a change in specimen geometry.

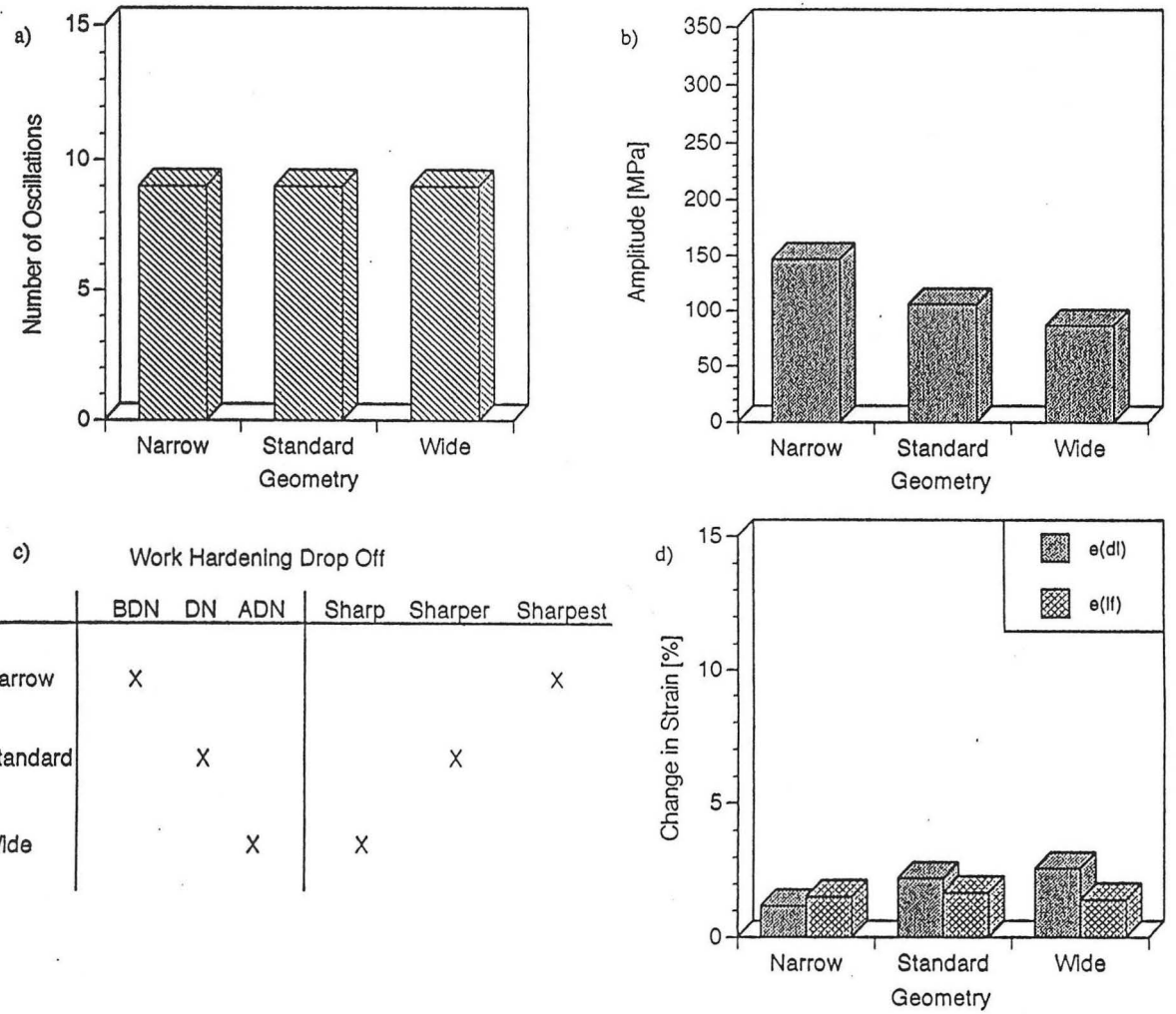

Figure 65: a) Number of oscillations, b) average amplitude, c) work hardening drop off characteristics and d) necking parameters for 6111-T4 tested at 10^{-4} /s and 300K when the gage width is changed.

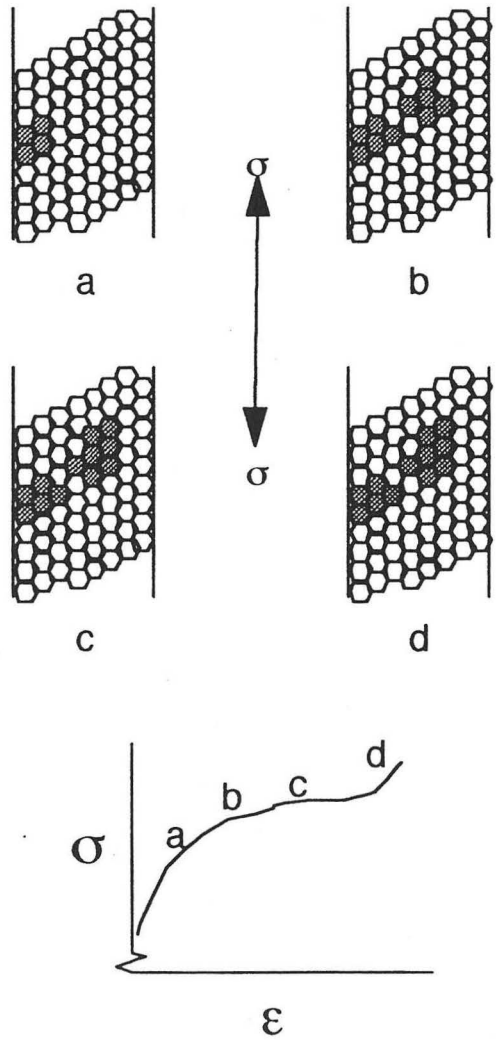

Figure 66: Hypothesized formation and propagation of deformation islands. a) Deformation will localize in a weak area of the sample; this softening is reflected as a decrease in the slope of the stress-strain curve. b) The island continues to propagate when the local stress can overcome obstacles in the neighboring grains; the slope in the stress-strain cuve continues to decrease. c) Island continues to propagate until it cannot overcome hard obstacles in its path; the slope in the stress-strain curve no longer decreases. d) The island hardens without increasing in size; the slope of the stress-strain curve is increasing. The cycle begins again when the island hardens to the point where it is more favorable to begin deformation in the next weakest area.

Ernest Orlando Lawrence Berkeley National Laboratory
One Cyclotron Road | Berkeley, California 94720

Prepared for the U.S. Department of Energy under Contract No. DE-AC03-76SF00098